ADVANCED TECHNOLOGIES FOR FABRICATION AND TESTING OF LARGE FLAT MIRRORS

by

Julius Eldon Yellowhair

A Dissertation Submitted to the Faculty of the

COLLEGE OF OPTICAL SCIENCES (GRADUATE)

In Partial Fulfillment of the Requirements
For the Degree of

DOCTOR OF PHILOSOPHY

In the Graduate College

THE UNIVERSITY OF ARIZONA

2007

UMI Number: 3257373

ProQuest Information and Learning Company
300 North Zeeb Road
P.O. Box 1346
Ann Arbor, MI 48106-1346

THE UNIVERISTY OF ARIZONA

GRADUATE COLLEGE

As members of the Dissertation Committee, we certify that we have read the dissertation prepared by Julius Yellowhair

entitled Advanced Technologies for Fabrication and Testing of Large Flat Mirrors

and recommend that it be accepted as fulfilling the dissertation requirement for the Degree of Doctor of Philosophy.

_____ Date: 04/18/07

James Burge, Faculty Advisor

_____ Date: 04/18/07

Jose Sasian, Member

_____ Date: 04/18/07

James Wyant, Member

_____ Date: _____

_____ Date: _____

Final approval and acceptance of this dissertation is contingent upon the candidate's submission of the final copies of the dissertation to the Graduate College.

I hereby certify that I have read this dissertation prepared under my direction and recommend that it be accepted as fulfilling the dissertation requirement.

_____ Date: 05/01/07

Dissertation Director: James Burge

STATEMENT BY AUTHOR

This dissertation has been submitted in partial fulfillment of requirements for an advanced degree at The University of Arizona and is deposited in the University Library to be made available to borrowers under the rules of the Library.

Brief quotations from this dissertation are allowable without special permission, provided that accurate acknowledgement of source is made. Requests for permission for extended quotation from or reproduction of this manuscript in whole or in part may be granted by the copyright holder.

SIGNED: Julius Eldon Yellowhair

ACKNOWLEDGEMENTS

This work was made possible by a tremendous team effort. I acknowledge these particular individuals – Mr. Norman Schenck who provided the daily extensive polishing runs, Dr. Jim Burge who provided the technical expertise and guidance, and Mr. Martin Valente who managed the entire project flawlessly and gave me the opportunity to get exposed to state of the art optical manufacturing. Others that have contributed tremendously, technically or otherwise, to this work are Robert Crawford, Thomas Peck, Dr. Jose Sasian, Dr. Brian Cuerden, Dr. Robert Stone, Dr. Chunyu Zhao, David Hill, Scott Benjamin, Marco Favela, Daniel Caywood, and numerous enthusiastic undergraduate and graduate students, in particular, Peng Su, Robert Sprowl, and Proteep Mallik. Without this team this dissertation would not have been possible.

I also thank my committee, Dr. Jim Burge (my advisor), Dr. Jim Wyant, and Dr. Jose Sasian, for providing guidance and feedback on my manuscript, and Dr. Matthew Novak and Mr. Dae Wook Kim (Dan) for painstakingly reviewing my manuscript and providing timely feedback. I thank my extremely talented and knowledgeable advisor, Dr. Burge, once more for bailing me out numerous times on challenging problems (personal, academic and technical).

Lastly I thank my wife, Valencia, who kept my life in balance for the past seven years, my mother, and the rest of the Yellowhair family for their tremendous love and support during my entire academic career. With their unbelievable support, failing was not an option. In particular, my mother (not a single day spent in school) is the driving force behind my success. Thank you, Mom!

DEDICATION

This dissertation is dedicated to my late father, Jimmie, and late brother, Nicholas. Your prayers are finally answered.

TABLE OF CONTENTS

TABLE OF CONTENTS – *Continued*

TABLE OF CONTENTS – *Continued*

TABLE OF CONTENTS – *Continued*

LIST OF FIGURES

LIST OF FIGURES – *CONTINUED*

LIST OF FIGURES – *CONTINUED*

LIST OF FIGURES – *CONTINUED*

LIST OF FIGURES – *CONTINUED*

LIST OF FIGURES – *CONTINUED*

LIST OF FIGURES – *CONTINUED*

LIST OF FIGURES – *CONTINUED*

LIST OF FIGURES – *CONTINUED*

LIST OF TABLES

LIST OF TABLES – *CONTINUED*

ABSTRACT

Classical fabrication methods alone do not enable manufacturing of large flat mirrors that are much larger than 1 meter. This dissertation presents the development of enabling technologies for manufacturing large high performance flat mirrors and lays the foundation for manufacturing very large flat mirrors. The enabling fabrication and testing methods were developed during the manufacture of a 1.6 meter flat. The key advantage over classical methods is that our method is scalable to larger flat mirrors up to 8 m in diameter.

Large tools were used during surface grinding and coarse polishing of the 1.6 m flat. During this stage, electronic levels provided efficient measurements on global surface changes in the mirror. The electronic levels measure surface inclination or slope very accurately. They measured slope changes across the mirror surface. From the slope information, we can obtain surface information. Over 2 m, the electronic levels can measure to 50 nm rms of low order aberrations that include power and astigmatism. The use of electronic levels for flatness measurements is analyzed in detail.

Surface figuring was performed with smaller tools (size ranging from 15 cm to 40 cm in diameter). A radial stroker was developed and used to drive the smaller tools; the radial stroker provided variable tool stroke and rotation (up to 8 revolutions per minute). Polishing software, initially developed for stressed laps, enabled computer controlled polishing and was used to generate simulated removal profiles by optimizing tool stroke

and dwell to reduce the high zones on the mirror surface. The resulting simulations from the polishing software were then applied to the real mirror. The scanning pentaprism and the 1 meter vibration insensitive Fizeau interferometer provided accurate and efficient surface testing to guide the remaining fabrication. The scanning pentaprism, another slope test, measured power to 9 nm rms over 2 meters. The Fizeau interferometer measured 1 meter subapertures and measured the 1.6 meter flat to 3 nm rms; the 1 meter reference flat was also calibrated to 3 nm rms. Both test systems are analyzed in detail. During surface figuring, the fabrication and testing were operated in a closed loop. The closed loop operation resulted in a rapid convergence of the mirror surface (11 nm rms power, and 6 nm rms surface irregularity). At present, the surface figure for the finished 1.6 m flat is state of the art for 2 meter class flat mirrors.

INTRODUCTION

There is a recent push for larger optical systems such as telescopes for space, thus there is increasing demand for large high performance flat mirrors (as references) to do component and/or full aperture system testing. Other uses of large flats include turning mirrors for ground based telescopes, which eliminate the need to point the telescope, and multipurpose shop use for component testing and periodic calibration of precision optical and mechanical metrology tools.

The need for large flats is evident, however, the manufacture of large flats (> 1 meter) is challenging for three reasons: 1) lack of techniques for precise and controllable polishing, 2) lack of accurate and efficient metrology, and 3) manufacturing takes a very long time to complete (months or even years).

Although technologies exist for manufacturing moderately sized flat mirrors (≤ 1 m), enabling technologies for making larger flat mirrors are limited or have not been developed. The cut-off is around 1 m diameter: flat mirrors that are 1 m or less in diameter can be manufactured efficiently and accurately; the cost of manufacturing, however, increases dramatically for flats larger than 1 m due to current inefficient fabrication and testing methods.

Flats require accurate surface testing. The requirement on surface power is on the same order of magnitude as surface irregularity. Conventional testing of flats requires comparison to another flat that is larger in size and has a much better surface quality.

However, large reference flats are almost non-existent, thus testing large flats in this manner is difficult. Due to fabrication and testing limitations, manufacturing large flat mirrors may take years, and thus, dramatically increasing cost.

This dissertation addresses the challenges listed above and describes the development and application of enabling technologies for fabricating and testing large high performance flat mirrors. Chapter one provides a background on flat mirror fabrication and conventional optical testing for large flats. The dissertation is then divided into two sections: Section one contains Chapters two through four and describes the development of accurate and efficient metrology used to guide the manufacture and qualify the final surface figure; Section two contains Chapter five and describes the development of precise and controllable polishing techniques that used small to moderate sized tools for figuring and polishing simulations for optimizing tool dwells and stroke enabling computer controlled polishing.

Some aspects of this dissertation have been published and presented. Other aspects still remain to be published in peer-reviewed journals.

My role on the manufacture of the 1.6 m flat was as the lead systems engineer. In addition to overseeing the testing and fabrication, I developed the electronic levels test, performed extensive analysis on the electronic levels and scanning pentaprism tests, which improved their accuracies, designed polishing runs using polishing simulation software and measured data, and, finally, integrating the metrology and fabrication into a closed loop manufacturing operation that eventually led to a rapid convergence of the 1.6 m flat surface errors. However, the work on this project was a lot more than one person

can handle. Below is a list of other people that directly contributed solutions to the many technical challenges that were present in this project:

Dr. Jim Burge – project scientist

Dr. Brian Cuerden (mechanical engineer extraordinaire) – mechanical modeling and detailed analysis

Dr. Robert Stone – mechanical modeling and analysis

Dr. Chunyu Zhao (technical go-to person) –software development for the Fizeau test and software support for the scanning pentaprism test

Mr. Norman Schenck – daily polishing runs and electronic levels measurements

Mr. Peng Su – maximum likelihood estimation software development for the reference and test surface determination in the Fizeau test and data analysis

Mr. Robert Sprowl – Fizeau system alignment and routine testing, and subaperture stitching and use of Park's method for test surface determination in the Fizeau test

Mr. Proteep Mallik – initial alignment and set-up of the scanning pentaprism test

Ms. Stacie Hvisc – software support on the scanning pentaprism test

The nice figures of mechanical hardware and structures were provided by Dr. Robert Stone, David Hill, Scott Benjamin, and Marco Favela. The finite element analysis results and models were provided by Dr. Robert Stone. The surface maps from the Fizeau test were provided by Peng Su and Robert Sprowl.

Below is a list of all the contributors by sub-projects.

1 meter vibration insensitive Fizeau interferometer development

Contributors:

Dr. Robert Stone (mechanical analysis)

David Hill (mechanical support)

Scott Benjamin (mechanical support)

Dr. Chunyu Zhao (software support)

Robert Sprowl – graduate (system alignment, testing, data analysis)

Peng Su – graduate (software support, data analysis)

Joshua Hudman – graduate (initial study)

Scanning pentaprism test development

Contributors:

Proteep Mallik – graduate (initial set-up, testing)

David Hill (mechanical support)

Scott Benjamin (mechanical support)

Daniel Caywood (mechanical support)

Grant Williams (software support)

Dr. Chunyu Zhao (software support)

Robert Sprowl – graduate (testing support)

Stacie Hvisc - graduate (software support

Stevie Smith – graduate (testing support)

Electronic levels test development

Contributors:

Norman Schenck (testing)

David Hill (mechanical support)

David Clark – undergraduate (software support)

Computer controlled polishing development

Contributors:

Norman Schenck (polishing support)

Robert Crawford (polishing guidance)

Thomas Peck (polishing guidance)

Scott Benjamin (mechanical support)

CHAPTER 1

INTRODUCTION TO LARGE FLAT MIRROR FABRICATION

1.1. Introduction

There is a recent push for larger optical systems such as telescopes for space [8-9]. That comes with an increasing demand for large high performance flat mirrors to do component and/or full aperture system testing. Large flat mirrors can also be used as turning mirrors for ground based telescopes, which eliminate the need to point the telescope. Furthermore, having a large (reference) flat mirror for multipurpose shop use is helpful for component testing and calibration of precision optical and mechanical metrology tools.

The need for large high performance flats is evident, however, manufacturing large flat mirrors that are much larger than 1 meter diameter is challenging [1-2]. For flat mirrors the tolerance on the radius of the surface is the same magnitude as the tolerance on surface irregularity; that is, power in the surface is considered an error that must be removed through careful polishing.

Current fabrication and testing technologies, although well established for moderately sized optics ($\leq$ 1 m), do not enable the manufacture of high performance flat mirrors much larger than 1 m. Large flat mirror fabrication poses significant challenges

in three areas: 1) techniques for precise and controllable polishing, 2) accurate and efficient metrology for surface testing, and 3) schedule and economic considerations.

The natural tendency of continuously rubbing two surfaces together (e.g. a polishing tool on glass) is for the two surfaces to shape themselves into spherical surfaces. This tendency makes spherical or near-spherical surfaces much easier to make. For flats, however, careful control of the polishing tool and parameters during polishing is required to make and keep the glass surface flat. We found during the manufacture of a 1.6 m flat that precise and controllable polishing is difficult using classical polishing methods alone. Furthermore, high precision flat surfaces require accurate metrology. Interferometeric testing of flat surfaces requires comparison to another flat surface that is larger in size and of significantly better surface quality. But large reference flats are virtually non-existent. Using liquids as reference flats have been proposed. The advantages of using liquid surfaces are they provide excellent reference surfaces [3-7] and large (> 1 m) liquid reference surfaces can be achieved. Large liquid surfaces are limited only by sag due to the radius of the earth. However, stability and contamination have been major issues, and the long settling times (hours) of liquid surfaces and test geometries make efficient testing impractical. Finally, large mirrors take a long time to make (years), and developing metrology for full surface testing can be cost prohibitive; thus, the manufacturing process may become very expensive (hundreds of thousands or even millions of dollars).

1.2. Current State of the Art for Flat Fabrication

The current state of the art for flat mirror fabrcation uses continuous polisher (CP) machines, which can produce flat surfaces that are 30 nm rms [10-14]. The CP uses a large annular lap that is at least three times the size of the part being polished and turns continuously. A top view diagram of a CP machine is shown in Figure 1.1. The parts to be polished are placed front surface down on the lap in holders that are fixed in place on the annulus and are driven so they turn in synchronous motion with the lap. Because the part is in synchronous motion with the lap, the part always remains in full contact with the lap, so the wear on the part will be uniform. The uniform contact and wear allows the surface to become flat rapidly. A conditioner that is as large as the radius of the lap helps keep the lap flat through the long polishing operation.

There are two advantages of using CP machines: 1) they can produce multiple flat mirrors simultaneously, making this type of a machine very cost-effective, and 2) they can polish smoothly out to the mirror edges because of the uniform contact between the mirror and the lap. The disadvantage, however, is that mirrors polished on a CP machine can be no larger than about a third of the diameter of the lap. CP machines with 4 m diameter laps are known to exist [13]. These particular CP machines can only accommodate up to 1.3 m flat mirrors. Any mirror bigger than 1.3 m has to be made with conventional methods.

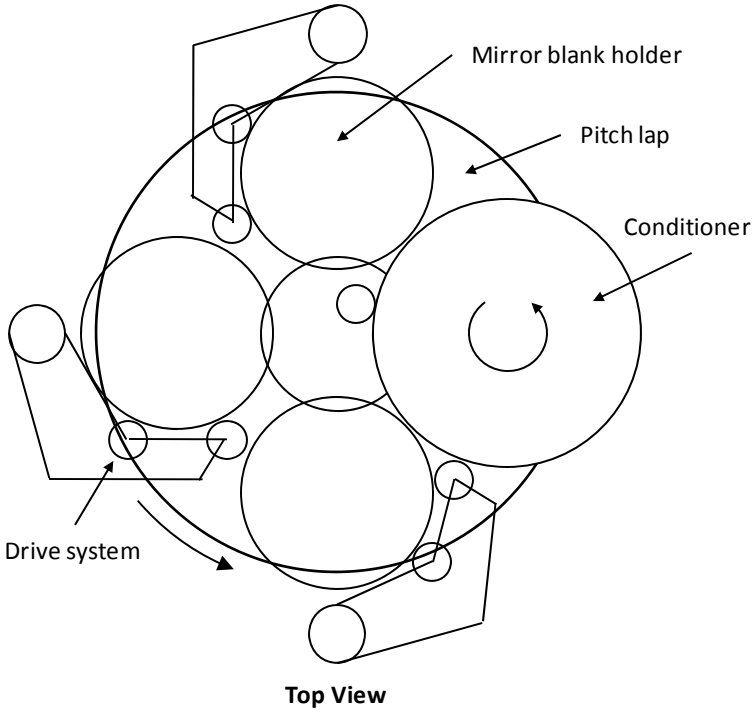

FIGURE 1.1. Top view diagram of the continuous polishing machine. The mirror parts continuously pass over the lap to get uniform wear on the surface.

1.3. Conventional Optical Testing of Large Flats

An interferometer is generally used to measure optical surface flatness. The type of interferometer depends on the size and shape of the surface being measured and the test geometry. In this section we describe three tests that are typically performed to measure flatness in large surfaces. The three tests have their advantages. But their disadvantages make them less accurate and efficient for testing large flats.

1.3.1. Fizeau interferometer

The simplest interferometer used to measure flat surfaces is the Fizeau interferometer [15-16]. The Fizeau interferometer uses a reference flat for comparison. Any surface

height differences is then attributed to the surface under test. Figure 1.2 shows a schematic of using a Fizeau interferometer to test a large flat. To make sure the reference and test surfaces are flat, a third flat surface is introduced to verify all surfaces are flat; this is the well known three flat absolute test [15].

Due to the limited aperture sizes of commercial Fizeau interferometers (10-15 cm), this test requires subaperture sampling and stitching to combine the subaperture measurements [17-20]. One major disadvantage of subaperture stitching is that the test accuracy and efficiency degrade as the test aperture becomes much smaller than the flat mirror under measurement.

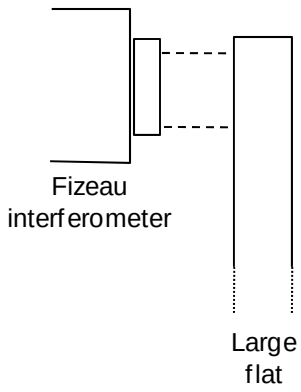

FIGURE 1.2. Schematic of an optical test using a Fizeau interferometer. Using a commercial Fizeau interferometer to test large flats requires many subaperture measurements and stitching to combine them.

1.3.2. Ritchey-Common test

The Ritchey-Common test places the flat mirror between the interferometer and a concave spherical mirror, as shown in Figure 1.3. With the Ritchey-Common test, full

surface testing of the large flat is possible. The test measures concavity (or convexity) accurately in the large flat mirror under test by measuring astigmatism in the surface [16, 21]. Surface irregularity, however, is more difficult to measure because the wavefront falls off with the cosine of the angle of incidence.

$$W = 4\delta\cos(\theta) \tag{1.1}$$

where δ is the surface error height. The beam is reflected off the flat surface twice so there is a factor of four in the measured wavefront. The difficulty comes from the angle, θ, changing across the flat surface. In addition, the sensitivity to surface irregularity decreases as the angle is increased.

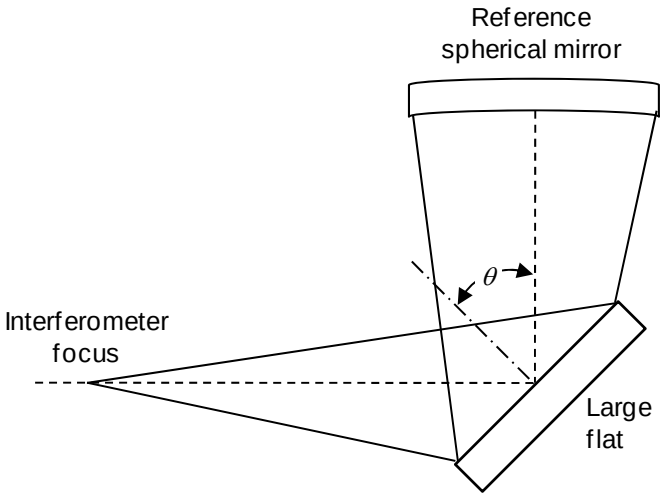

FIGURE 1.3. Schematic of a Ritchey-Common optical test. The Ritchey-Common test uses a large spherical reference surface and is typically performed on large flats.

The advantage of the Ritchey-Common test over the Fizeau test is that it does not require a reference flat surface for comparison. The disadvantage is, although easy to

make, the spherical mirror must be larger than the flat mirror under test. Moving large optics around the shop, mounting them, and aligning them are not easy tasks. Therefore, the Ritchey-Common test is difficult and time consuming for very large mirrors.

1.3.3. Skip flat test

A less documented and relatively unknown test of large flat mirrors is the skip flat test [22, 30]. This test uses an interferometer with a collimated output that is much smaller than the test surface. The collimated beam is reflected from the test surface at an oblique angle. The beam is returned with a flat mirror to provide a narrow profile of the mirror. A schematic of the test geometry is shown in Figure 1.4. There is an anamorphic magnification between the long and short axes of the beam footprint at the test surface. Multiple measurements taken in different directions can be performed to determine the figure of the test surface. The skip flat test is similar to the Ritchey-Common test; the measured wavefront is multiplied by a factor of four due to the double reflection and falls off as the cosine of the angle of incidence (Equation 1.1), where the cosine of the angle of incidence in the skip flat test is the ratio of the diameters of the return flat and the large test flat.

The skip flat test has been used where conventional surface testing was difficult to perform (e.g. a cryogenic test of large mirrors). Like other stitching tests, however, accuracy and efficiency suffer as the size of the measured subaperture decreases with respect to the size of the mirror under test [17, 20].

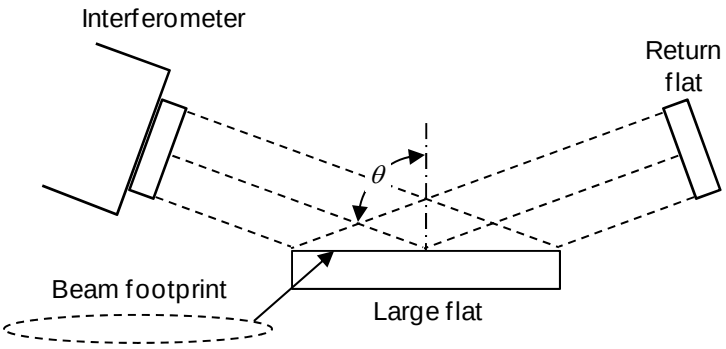

FIGURE 1.4. Schematic of a skip flat optical test. The skip flat test is performed on large flats.

SECTION I

ADVANCED TESTING TECHNOLOGIES

The first section presents testing technologies that were developed, analyzed, and implemented during the manufacture of a 1.6 meter flat mirror. We developed two slope tests, electronic levels and scanning pentaprism, and a 1 meter vibration insensitive interferometer based on the classical Fizeau interferometer. The electronic levels were used during the early stage of fabrication to measure global surface changes in the flat. The scanning pentaprism and the 1 m Fizeau interferometer are highly accurate tests that were used to guide the remaining fabrication and qualify the final surface figure of the 1.6 meter flat.

Two electronic levels, described in Chapter 2, provided an easy and efficient slope test to guide surface grinding and coarse polishing. An algorithm was developed to reduce the measured slope data and obtain surface maps represented by Zernike polynomials. With the electronic levels the surface of the 1.6 m mirror can be measured to 50 nm rms of low order aberrations.

The scanning pentaprism system, described in Chapter 3, has been used successfully to test paraboloidal mirrors at the University of Arizona. By replacing the beam projector and position detector with a high resolution electronic autocollimator and carefully aligning the two pentaprisms to the autocollimator, this test system can be used

to test large flat surfaces to 9 nm rms power by performing diagonal line scans. The test system has the option of measuring other low and mid order Zernike aberrations and only θ dependent aberrations, which are obtained by performing circumferential scans where both pentaprisms are fixed and the test mirror continuously rotates underneath.

The vibration insensitive Fizeau interferometer, described in Chapter 4, used 1 m subaperture sampling to measure surface irregularity. By using two different techniques (stitching and maximum likelihood estimation) the subaperture measurements were combined to produce a full synthetic surface map. This test relied on multiple overlapping subaperture measurements and measurement redundancy to isolate the errors in the reference flat and the test flat to 3 nm rms.

CHAPTER 2

OPTICAL FLATNESS MEASUREMENTS USING ELECTRONIC LEVELS

Conventional measurement methods for large flat mirrors are generally difficult and expensive. In most cases, comparison with a master or a reference flat similar in size is required. Using gravity, such as in modern pendulum-type electronic levels, takes advantage of a free reference to precisely measure inclination. We describe using two electronic levels to measure flatness of large flat mirrors. Using two levels differentially allows surface slope measurements of large flat mirrors by removing common tilt between the levels. One level is fixed, while the other level is moved across the mirror surface. We provide measurement results on a 1.6 meter flat mirror. Our method of measurement and data reduction resulted in measurement of surface accuracy to 50 nm rms.

2.1. Introduction

Traditionally, large flat mirror testing can be difficult and expensive. The Ritchey-Common test (described in Chapter 1), for example, requires a reference spherical mirror larger in size than the test surface. The test is straight forward on a smaller scale; however, aligning large optical components is a difficult and time consuming process.

The impact on schedule makes this test expensive for large optics. To overcome this problem, we introduce a simple and cost effective slope test that uses two high precision electronic levels.

Since the mid-1900's techniques have been developed to measure flatness of surfaces, namely industrial surface plates [23]. Methods to estimate the uncertainty in the measurements to calibrate the surface plates have also been developed [23-24]. The first measurement instruments included an analog autocollimator with a sliding mirror aligned to the autocollimator. The autocollimator measured angle deviations in the surface by sliding the mirror along measurement lines over the surface plate. Height profiles were obtained by integrating the measured angle deviations or slopes. In the 1990's high precision electronic levels were introduced and became commercially available. The measuring principle of electronic levels is based on a friction free pendulum suspended between two electrodes. A deflection to the pendulum changes capacitance between the electrodes, which is detected by a transducer and translated to an angle reading. Due to their ease of use and cost effectiveness the electronic levels replaced the autocollimator and mirror for measuring flatness of surfaces. One benefit of electronic levels is that their use does not require the skill needed to operate an autocollimator. Also, the angle readings can be recorded from a digital display or an acquisition system, which is a major advantage over the time consuming process of manual data recording.

At the University of Arizona Optical Engineering and Fabrication Facility (UA-OEFF), we extended the concept of measuring flatness of surface plates to optical surfaces. A significant advantage of using electronic levels for surface measurements of

large mirrors during fabrication is that the mirror can remain on the polishing supports. In contrast, other types of test systems may require moving the test mirror to a testing fixture. In addition to measurement efficiency, their ease of use and cost effectiveness make the electronic levels ideal for flatness measurements of large mirrors during manufacturing.

The concept of using uni-axis electronic levels for large flat mirror measurements is first introduced in Section 2.2. Section 2.3 provides the measurement sensitivities and the error analysis. Next, Section 2.4 provides results of flatness measurements on a 1.6 m flat mirror. In Section 2.5 a comparison of the electronic levels and the scanning pentaprism tests is performed and the results are provided. Section 2.6 describes a conceptual implementation of dual-axis electronic levels for flatness measurements on large flat mirrors. A Monte Carlos simulation of dual-axis electronic levels for surface measurements is also presented. Finally, the concluding remarks are provided in Section 2.7.

2.2. Test Concept

2.2.1. High precision electronic levels measurement system

A single high precision electronic level measures inclination of a surface, α, very accurately, as shown schematically in Figure 2.1. Two levels used differentially allows for surface slope measurements along the pointing direction where one level provides the reference measurement, B, and the other level provides measurement A. The differential measurement is the difference in the angular reading of the two instruments, $A - B$. The

reference level is normally fixed while level *A* is moved over the surface maintaining the common pointing of both levels. Typically, this mode of measurement is used to measure flatness of surface plates. In our case, we measure the flatness of large mirrors.

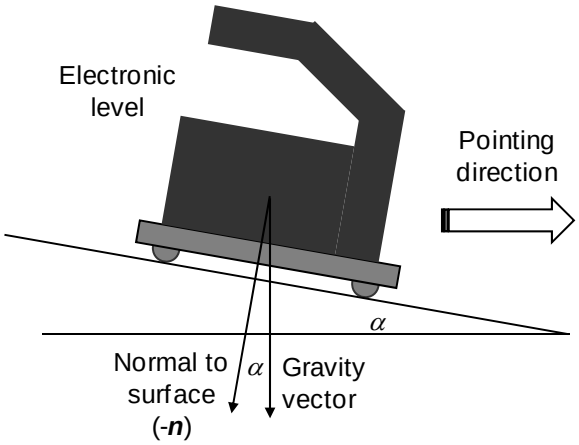

FIGURE 2.1. Schematic of the set up for measuring surface inclination with the electronic level.

Two high precision uni-axis electronic levels (Leveltronic NT made by Wyler AG [25]) were procured along with the necessary hardware and electronics. Uni-axis, as opposed to dual axis, levels can only measure inclination in the pointing direction. The standard steel base plates were replaced with custom aluminum plates and three tungsten carbide half-spheres for surface contact, as shown in Figure 2.2.

Maintaining the pointing of both levels is important when measuring flatness of large mirrors. To ensure single line scans, a fiberglass guide rail was fabricated to fit over the flat mirror as shown in Figure 2.3. The guide rail ensured consistent pointing of the levels, and also provided repeatable measurement locations.

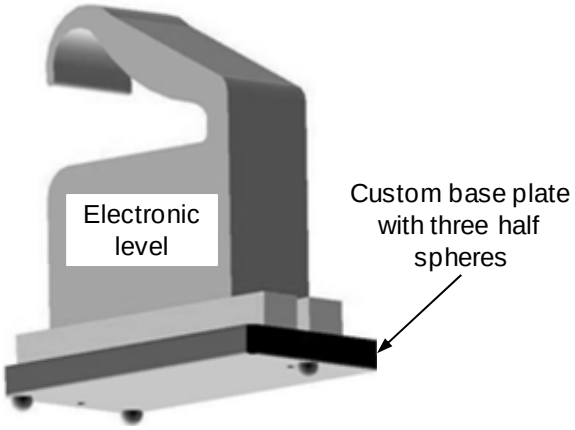

FIGURE 2.2. A Wyler Leveltronic NT electronic level with a custom aluminum three-point base plate for stable positioning.

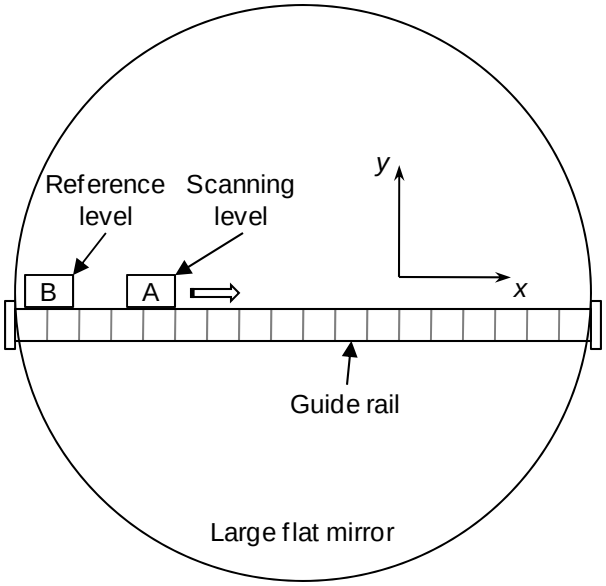

FIGURE 2.3. Top view of the electronic levels measurement set up for flatness measurements. A fiberglass guide rail secured to the mirror maintained the pointing of the electronic levels.

2.2.2. Principles of operation

To measure surface slopes the two levels were always used differentially. In this mode, the reference level remained fixed anywhere along the guide rail while the other level

was scanned along the guide rail across the diameter of the mirror. The scanning level was placed at several positions along the guide rail ensuring that the part was well sampled to avoid aliasing of the surface modes of interest.

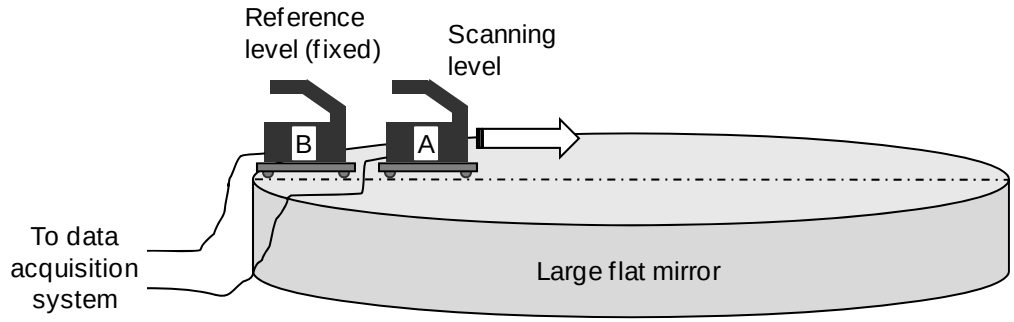

FIGURE 2.4. Schematic of differential slope measurement on an optical surface using two electronic levels.

A workstation running LabVIEW was used for data acquisition. For each measurement position 50 data points were acquired and averaged. The measurement positions on the mirror were recorded along with the slope reading for that position. The slope data, measurement positions, and other measurement parameters (e.g. mirror diameter, number of measurement points for each scan, number of scans, etc.) were saved into a text file. The text file was then imported into the analysis software, which reduced the slope data into low order Zernike aberrations through a least squares calculation. The outputs were the Zernike coefficients (in μm), a fitted two dimensional surface map, and statistics on the fitted surface map

.

2.2.3. Fit using Zernike polynomials

Since the electronic levels measured slope change, we performed the analysis using a basis set of slope functions derived from the Zernike polynomials. If the surface error is described by

$$S(x,y)=\sum a_i Z_i(x,y) \tag{2.1}$$

where Z_i are the Zernike polynomials in Cartesian coordinates and a_i are their coefficients, and measurements made in a direction is defined by

$$\hat{\mathrm{i}}\cos\theta+\hat{\mathrm{j}}\sin\theta, \tag{2.2}$$

then the slope data can be expressed as

$$\alpha(x,y,\theta)=\sum a_i \bar{\nabla} Z_i(x,y)\cdot\left(\hat{\mathrm{i}}\cos\theta+\hat{\mathrm{j}}\sin\theta\right), \tag{2.3}$$

where $\bar{\nabla} Z_i(x,y)$ is the gradient of the Zernike polynomials and forms a dot product with the measurement direction. The low order Zernike aberrations and their gradients are shown in Table 2.1.

The analysis software creates a matrix of low order slopes and a vector of measured surface slopes. Through a least squares calculation, the Zernike coefficients are determined by

$$[a]=[\alpha]\backslash[z'], \tag{2.4}$$

where $[z']$ is a matrix of gradients of the Zernike polynomials projected in the measurement direction

$[\alpha]$ is a vector of measured slope variations across the mirror surface.

The "\" operator is used in Matlab [26] for the least squares fit. After the coefficients are determined, the Zernike polynomials are used to generate a two dimensional surface topology of the flat mirror.

TABLE 2.1. List of the low order Zernike (UofA) polynomials and their gradients.

Aberration	Zernike	Gradient
Power	$Z4 = 2(x^2 + y^2) - 1$	$4x\hat{\mathbf{i}} + 4y\hat{\mathbf{j}}$
Astigmatism	$Z5 = (x^2 - y^2)$	$2x\hat{\mathbf{i}} - 2y\hat{\mathbf{j}}$
	$Z6 = 2xy$	$2y\hat{\mathbf{i}} + 2x\hat{\mathbf{j}}$
Coma	$Z7 = 3(x^3 + xy^2) - 2x$	$(9x^2 + 3y^2 - 2)\hat{\mathbf{i}} + 6xy\hat{\mathbf{j}}$
	$Z8 = 3(x^2y + y^3) - 2y$	$6xy\hat{\mathbf{i}} + (3x^2 + 9y^2 - 2)\,\hat{\mathbf{j}}$
Spherical	$Z9 = 6(x^4 + y^4) - 6(x^2 + y^2) + 1$	$12x(2x^2 - 1)\hat{\mathbf{i}} + 12y(2y^2 - 1)\hat{\mathbf{j}}$
Trefoil	$Z10 = x^3 - 3xy^2$	$3(x^2 + y^2)\hat{\mathbf{i}} - 6xy\hat{\mathbf{j}}$
	$Z11 = 3xy^2 - y^3$	$6xy\hat{\mathbf{i}} + 3(x^2 - y^2)\hat{\mathbf{j}}$

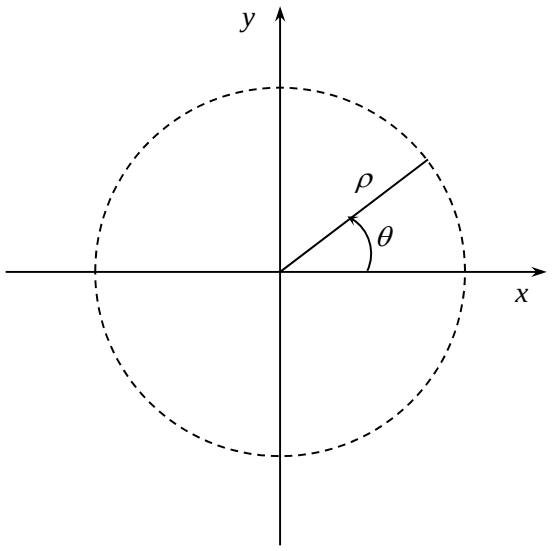

FIGURE 2.5. Coordinate system for defining the Zernike polynomials (ρ is the normalized radial coordinate and θ is the measurement direction).

2.3. Analysis

2.3.1. Sensitivity analysis: sampling for low order Zernike aberrations

A single line scan across the mirror does not sample all the low order Zernike aberrations shown in Table 2.1. The asymmetrical aberrations have orthogonal components, sine and cosine. Measuring for both components of astigmatism, for example, requires three line scans in different directions (e.g. three line scans separated by 120° as shown in Figure 2.6c). Three scans also allow averaging for power to reduce noise. Figure 2.6 shows other types of sampling arrangements that measure the low order aberrations.

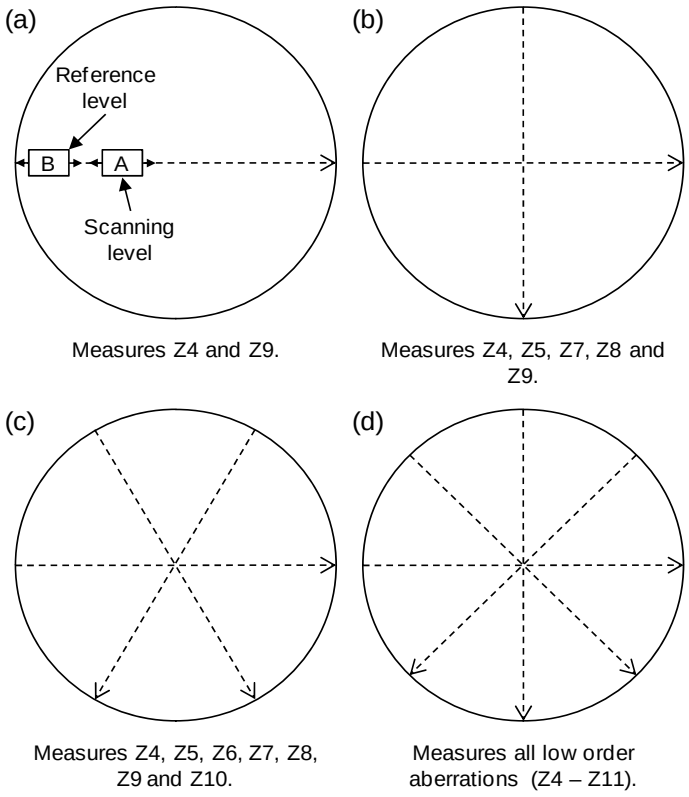

FIGURE 2.6. Sampling requirements for measuring low order Zernike aberrations. The dashed lines represent electronic level scan lines.

Scans through the center of the mirror are not a requirement. The scans can be offset from center; the aberrations measured still hold for the number of line scans made. The mirror surface should be well sampled along each scan line to avoid aliasing of the surface modes. For example, we periodically sampled for secondary spherical aberration. Sampling for secondary spherical requires a minimum of five measurement points across the diameter of the mirror, but this leaves a large measurement uncertainty for secondary spherical due to noise (discussed in more detail in Chapter two). More measurement points across the mirror will reduce the uncertainty.

Figures 2.7 and 2.8 show how the slope measurements would appear for the low order aberrations if the three line scans (at 0°, 120°, and 240°) shown in Figure 2.6c were performed. The plots are normalized by assuming the Zernike wavefront coefficients are 1 μm. The amount of each low order term is determined using the least squares fit to the measured slope data.

The three line scans have excellent sensitivities to the low order aberrations, except for Zernike 11 (sin trefoil). Trefoil is, thus, not adequately sampled with the three line scans. To fix this, four line scans shown in Figure 2.6d is required. To avoid aliasing, a minimum of three measurement points across the mirror diameter is required to measure all the low order aberrations (spherical aberration requires the most number of measurement points). But as pointed out previously, the measurement uncertainty due to noise will be high for a small number of measurement points.

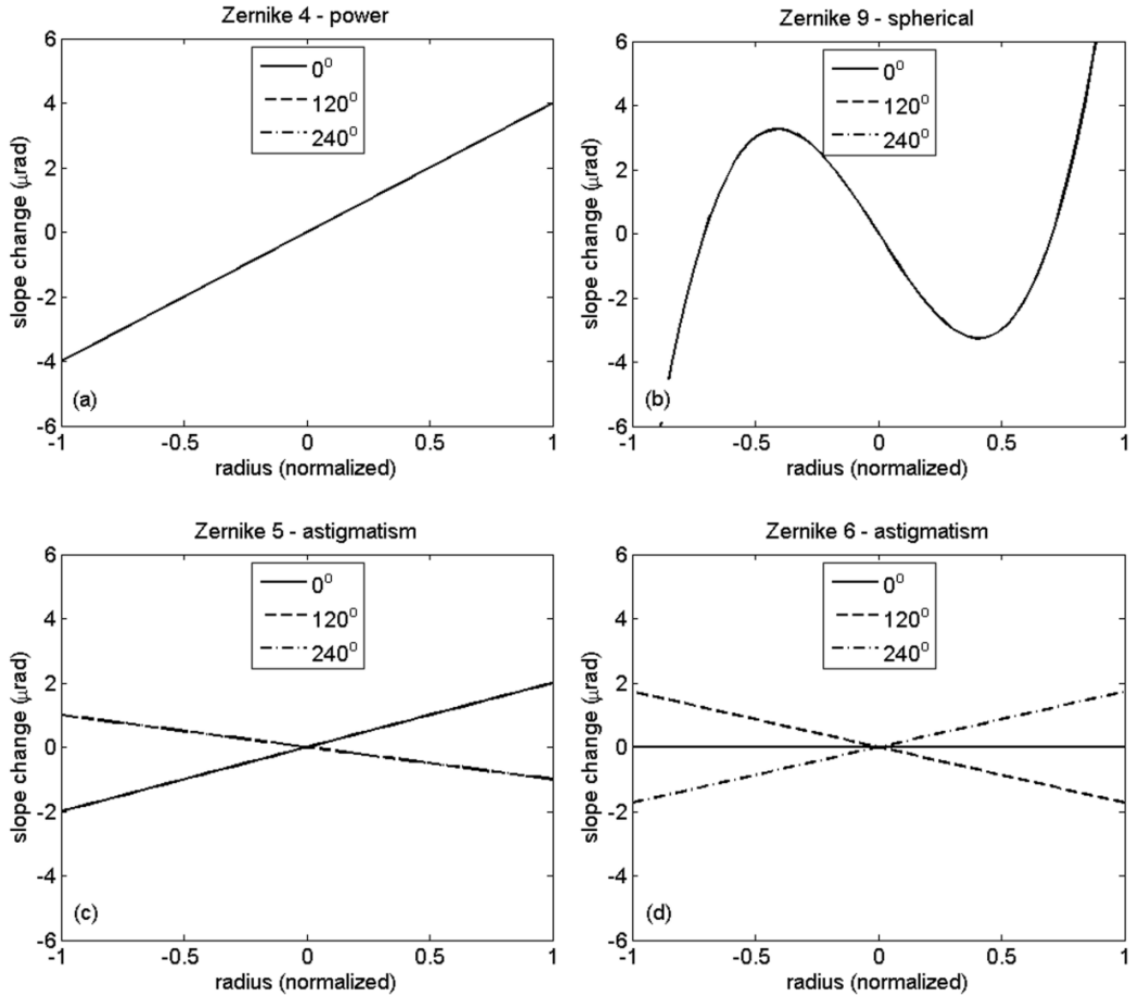

FIGURE 2.7. Simulated three line scans (separated by 120°) for low order surface errors described by single Zernike polynomial terms (power, astigmatism, and spherical aberrtaion).

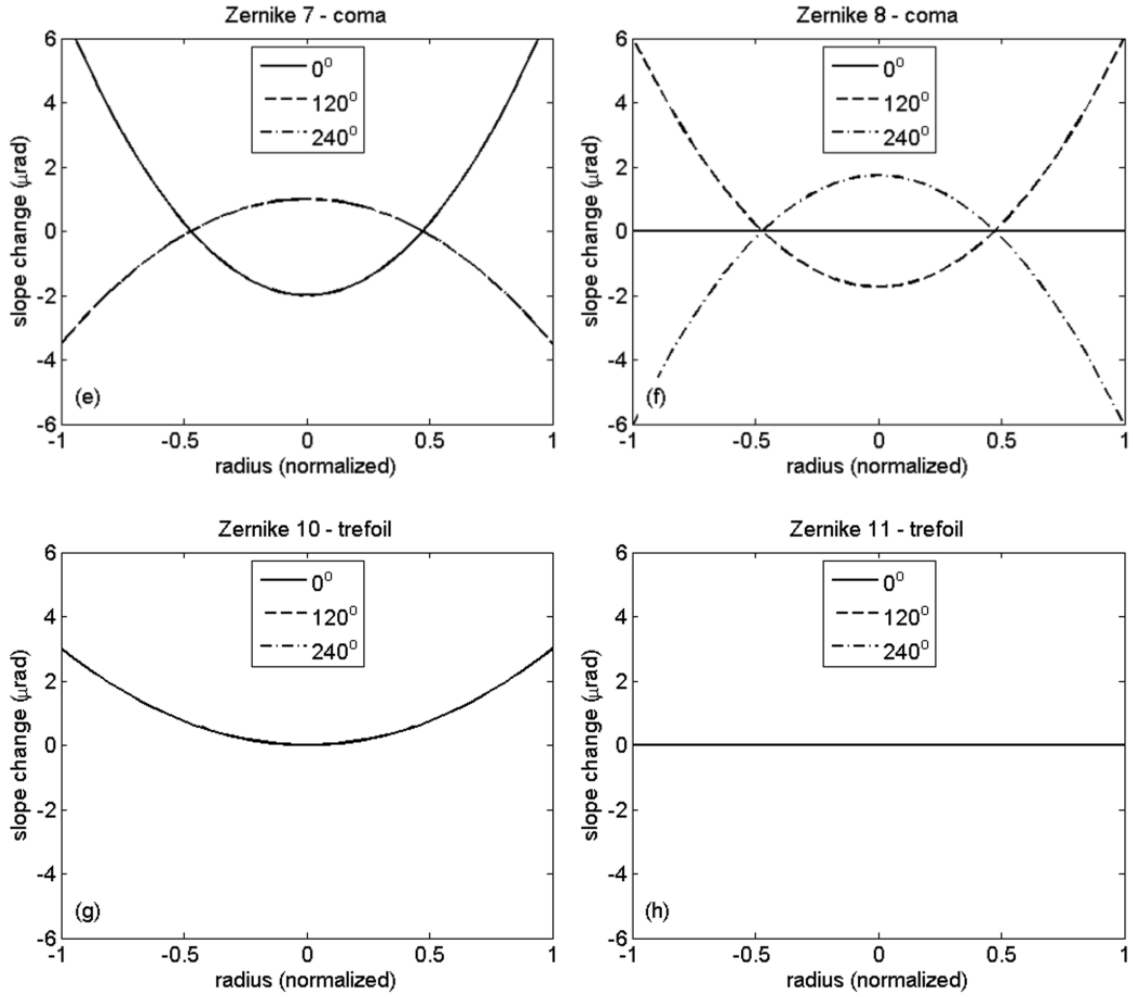

FIGURE 2.8. Simulated three line scans (separated by 120°) for low order surface errors described by single Zernike polynomial terms (coma and trefoil).

2.3.2. Error analysis

Drescher [20] reported on a method for estimating uncertainty in the surface slope measurements of industrial surface plates. We applied a similar analysis for measuring optical surfaces. The error sources can be separated into two categories: random and systematic errors. The random errors can be controlled through data averaging. The

systematic errors are fixed and cannot be eliminated, but they may be minimized after characterizing them.

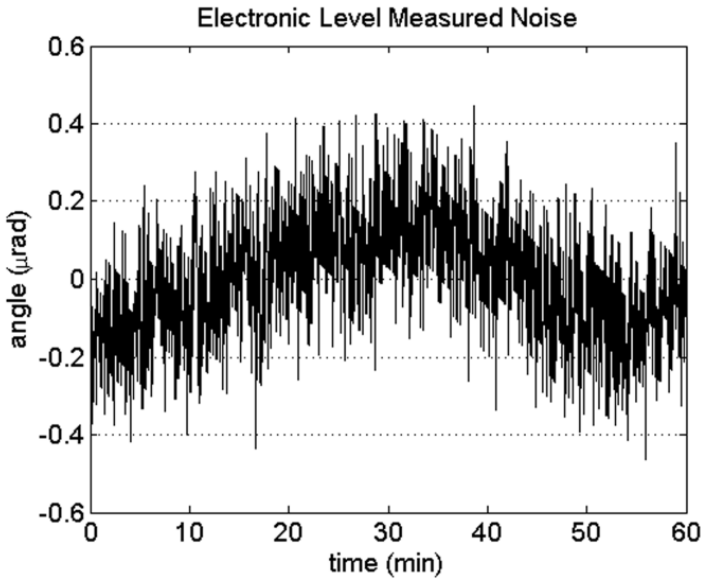

FIGURE 2.9. Measured noise in the electronic levels after removing linear drift (1σ = 0.15 μrad). Sample period = 3.3 Hz (full rate).

Random errors:

1. There is inherent noise associated with the electronic levels. We measured the noise floor of the levels to less than 0.2 μrad. The plot in Figure 2.9 shows a typical continuous measurement exhibiting noise after removing the drift effect. The continuous measurement was performed over one hour at the full sampling rate of the device (3.3 Hz) in the same environment in which the optical surface slope measurements were performed.

2. There was drift observed in the measurements due to environmental effects, notably thermal. The magnitude and direction of the drift seemed to be random in nature. The plot in Figure 2.10 represents a typical continuous measurement that shows drift and noise. The levels were placed on a flat rigid surface and allowed to settle and equilibrate for one hour. Measurements were then continuously taken over another hour at the full sampling rate of the device.

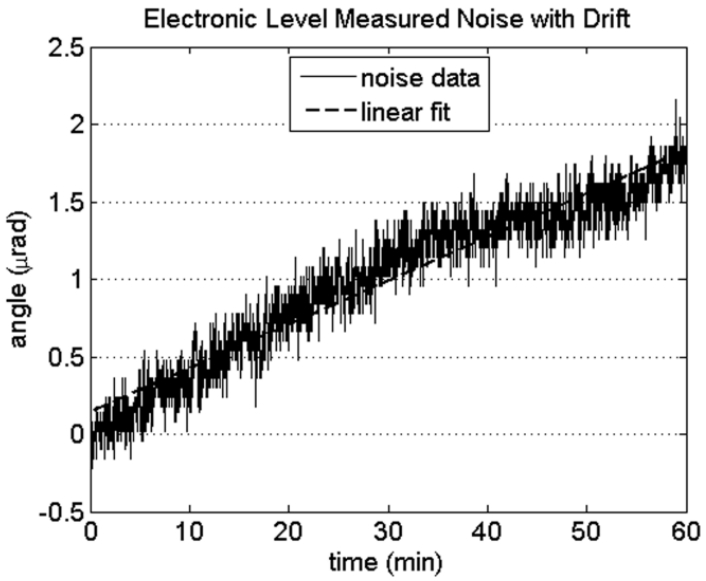

FIGURE 2.10. Measured drift and noise over 60 minutes. The amount of drift is about 1.75 μrad over 60 min (30 nrad/min).

The plot shows the level drifted about 1.75 μrad over 60 minutes or 30 nrad per minute. To minimize the drift effect, a reference measurement was always acquired that accompanied the data point. The reference measurement was then subtracted from the data. The two measurements were acquired in rapid succession that was much less than

the time constant of the drift. For example, a full measurement performed at one position on the mirror in three minutes introduced about 90 nrad of error.

3. The fiberglass guide rail used to maintain the pointing of the levels was not perfectly straight. The straightness was specified to less than 0.5 mm/m. This caused an error in pointing and coupling of the reading between the orthogonal axes, thus the slope error in the *x* direction became

$$\Delta\alpha_x = \alpha_y \times \Delta\theta\,, \tag{2.5}$$

where α_y is the slope in *y*

$\Delta\theta$ is the error in pointing (0.5 mrad).

For a ground mirror surface, the slopes can vary by no more than 4 nrad per mm. The contact point spacing of the electronic levels in the *y* direction was 64 mm, thus the slope in *y* vared by 256 nrad. The error in the slope reading in the *x* direction was then 0.13 μrad.

4. The slope error due to placement and setting of the levels is described by

$$\Delta\alpha = \left[\left(\frac{\mathrm{d}\alpha_x}{\mathrm{d}x}\mathrm{d}x\right)^2 + \left(\frac{\mathrm{d}\alpha_y}{\mathrm{d}y}\mathrm{d}y\right)^2\right]^{1/2}. \tag{2.6}$$

The fiberglass guide rail helped constrain the placement of the levels to 2 mm in the pointing direction *x* and to 0.5 mm in the *y* direction. If the surface slopes varied by 4 nrad/mm, then the placement error caused about 8 nrad in the measurement direction.

5. The residual error from the slope fit calculation consistently introduced an uncertainty of about 0.13 μrad. This error can be reduced by including more measurement points across the mirror.

Systematic errors:

There is only one systematic error to consider.

1. The gravity effects on the pendulum may introduce an additional angle deflection. The assumption was the level pendulum always pointed in the direction of gravity for reference. However, the force of attraction between the pendulum and a nearby large object can cause an additional deflection to the pendulum, thus changing the slope measurements.

The attracting force between two objects is defined by

$$F = G\frac{m_1 m_2}{r^2}, \tag{2.7}$$

where G is the gravitational constant

m_1 and m_2 are the masses of the two objects

r is the distance between the objects.

The force in Equation 2.7 on the pendulum can cause an additional deflection by amounts shown in the plot in Figure 2.11. The plot shows, however, that an object must be about 7,000 kg (8 tons) and 0.5 m away to have a noticeable effect on the slope measurements. The only large object in close proximity to the mirror was the polishing machine which weighs about 3 tons (2,722 kg). The force of attraction between the

polishing machine and the level pendulum would then cause an error of less than 0.1 μrad.

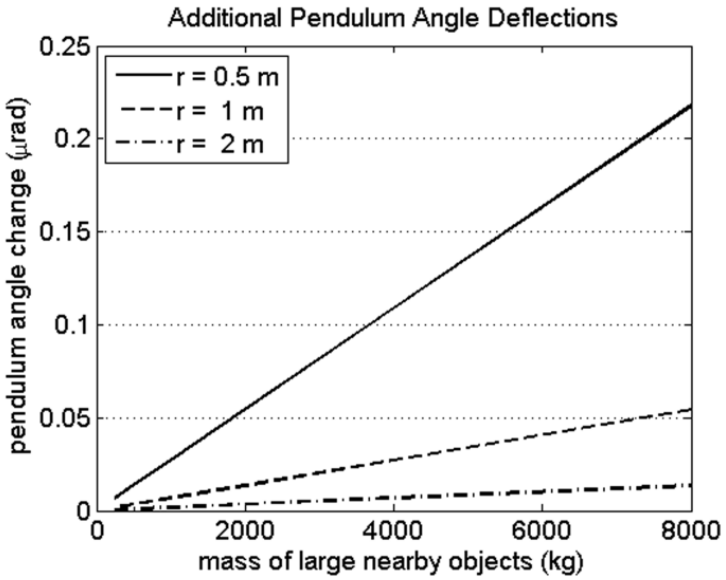

FIGURE 2.11. Simulated changes in pendulum angle due to force of attraction between the pendulum and nearby large objects.

TABLE 2.2. Sources of error for slope measurements that are assumed uncorrelated (for a single level).

Error source	Value (μrad)
Noise in the levels and calibration	0.25
Drift due to environment	0.10
Axes coupling (guide rail)	0.13
Levels placement and setting	0.01
Software residual fit error	0.13
Root sum square	0.33

Table 2.2 shows a summary of the error sources and their values. A root sum square (RSS) of all the error sources that are uncorrelated is about 0.33 μrad for a single level. The error from gravity effects then limits the accuracy of the level to about 0.4 μrad.

A Monte Carlo simulation of the three line scans (shown in Figure 2.6c) on a 2 m flat mirror was performed to determine the sensitivities of the low order Zernike aberrations using an uncertainty of 0.56 μrad for a single differential measurement. This analysis assumed 12 measurement points per scan. From the result of the simulation, the measurement uncertainty of each of the low order aberrations can be estimated. Table 2.3 shows that the expected accuracy for the measurement of a 2 m flat mirror is 50 nm rms of low order aberrations.

TABLE 2.3. Measurement uncertainty for the low order Zernike aberrations with the uni-axis levels.

Zernike aberration	Measurement uncertainty (nm rms)
Power	16
Cos Astigmatism	29
Sin Astigmatism	29
Cos Coma	11
Sin Coma	11
Spherical	8
Secondary Spherical	6
Root sum square	50

2.3.3. Other scanning arrangements for uni-axis electronic levels

There are other possible scanning arrangements for measuring surface slopes in large flat mirrors using uni-axis electronic levels. Figure 2.12 shows orthogonal scans with up-down (a) and left-right (b) pointing directions. The data analysis remains the same for these scanning arrangements. These types of scanning arrangements were not performed during this work.

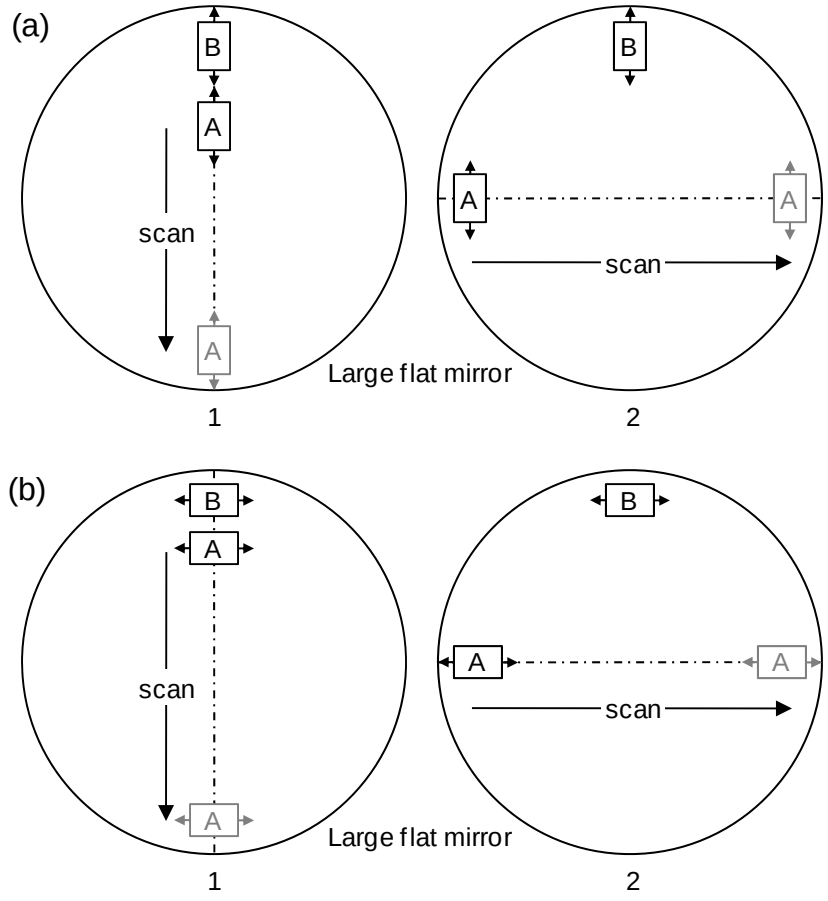

FIGURE 2.12. Orthogonal scans with up-down (a) and left-right (b) pointing directions using uni-axis electronic levels.

2.4. Measurement of a 1.6 Meter Flat Mirror

2.4.1. Single line scan

A single line scan, as shown in Figure 2.6a, provides information only on symmetrical aberrations (e.g. power). Figure 2.13 shows the result of a single line scan on the 1.6 m mirror while in was in production. The top left plot (2.13a) shows the measured surface slopes with 12 measurement points and a fit to them using slope functions for power and spherical. The bottom left plot (2.13b) shows the surface profile in microns after determining the Zernike coefficients. The right plot (2.13c) shows the two dimensional fitted surface map and the scan made on the mirror. All of the plots are normalized in radius.

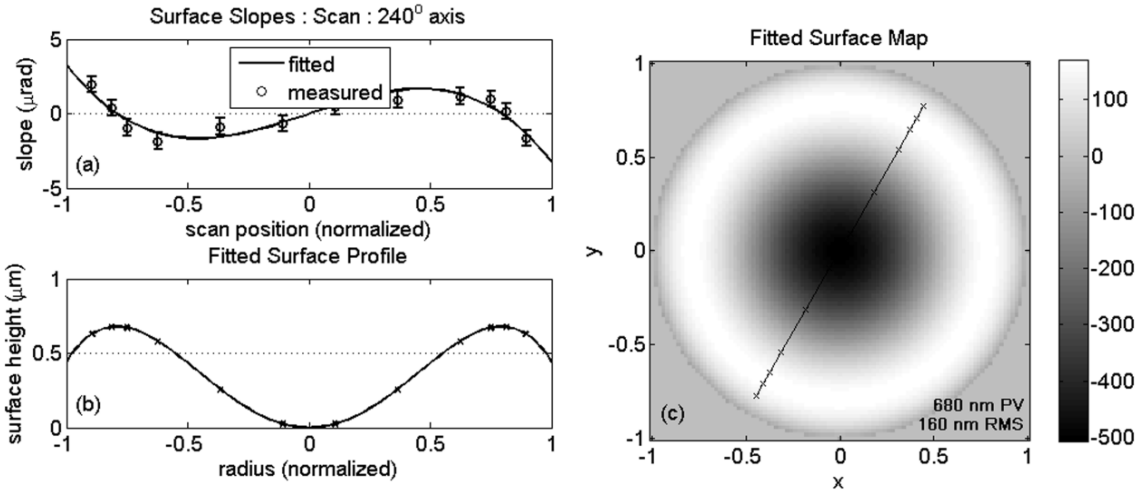

FIGURE 2.13. (a) Low order symmetrical Zernike aberrations fitted to measured slope data. (b) Surface profile of the fitted surface map. (c) The corresponding two dimensional fitted surface map with 680 nm PV and 160 nm rms.

The results shown in Figure 2.13 yielded an overall surface error of 160 nm rms: 127 nm rms was attributed to power and 128 nm rms to spherical.

2.4.2. Three Line Scans

The three line scans, as shown in Figure 2.6c, provide information on all the low order Zernike aberrations, except for trefoil. Figure 2.14a shows the result of the three line scans on the same 1.6 m flat mirror (at an earlier time in the fabrication process) and fits to them using slope functions of the low order Zernike polynomials. For this set of measurements we did not sample the center of the mirror.

Figure 2.14b shows the generated two-dimensional surface map and the line scans after the least squares calculation of the Zernike coefficients. The resulting surface map shown in Figure 2.14b yielded 295 nm rms of overall surface error. Table 2.4 shows a breakdown of error contributions from the low order aberrations.

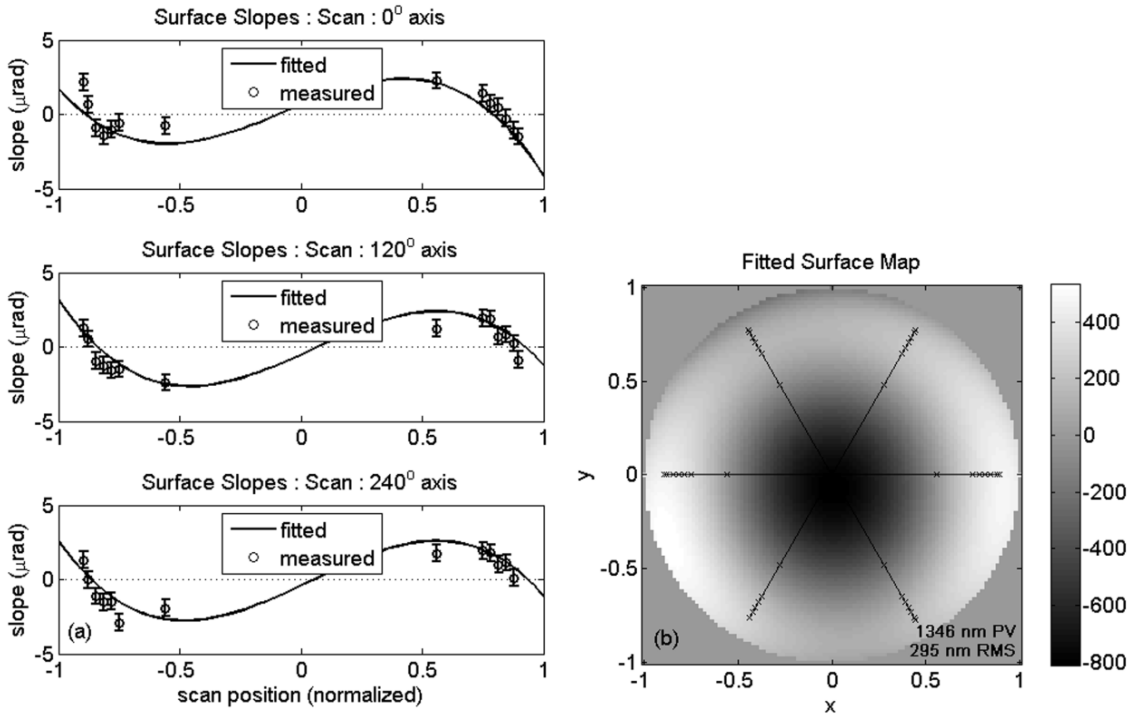

FIGURE 2.14. (a) Fit to measured surface slopes along three line separated by 120°. (b) The resulting surface map of the three line scan (295 nm rms).

TABLE 2.4. Values of the low order Zernike coefficients after fit to surface slopes.

Zernike Aberration	Value (nm rms)
Power	280
Cos Astigmatism	-97
Sin Astigmatism	33
Cos Coma	-65
Sin Coma	6
Spherical	-141

2.5. Comparison of the Electronic Levels and Scanning Pentaprism Tests

This section presents the results of the comparison of the electronic levels and the scanning pentaprism test. Both test systems measured surface slopes with the scanning pentaprism providing higher measurement accuracy. To validate the measurements with the electronic levels, the 1.6 m flat was measured with both test systems while the mirror was in early production. The same direction on the mirror was measured and 10 measurement points were acquired with both test systems. The sampling spacing between the two systems differed, however.

Figure 2.15 shows the results from the electronic levels test, and Figure 2.16 shows the results from the scanning pentaprism test. Table 2.5 shows (for comparison) the surface statistics from both tests after power and spherical aberration were fit to the slope data. Table 2.6 shows the difference in the data from both tests.

Results from the Electronic Levels Test

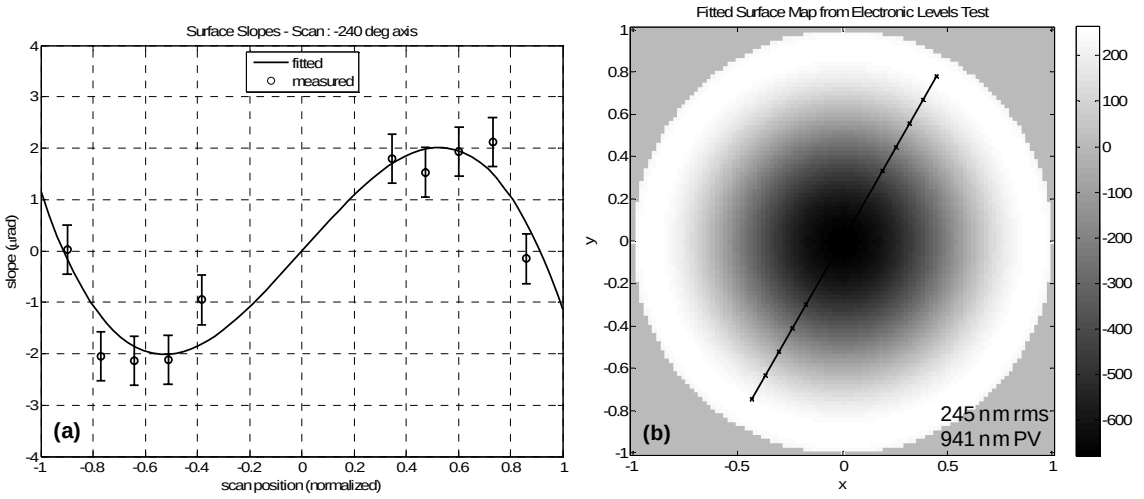

FIGURE 2.15. Measurements on the 1.6 m flat with electronic levels. (a) Slope measurements and fit to the slope data. (b) A fitted surface map after determining the Zernike coefficients through a least squares fit.

Results from the Scanning Pentaprism Test

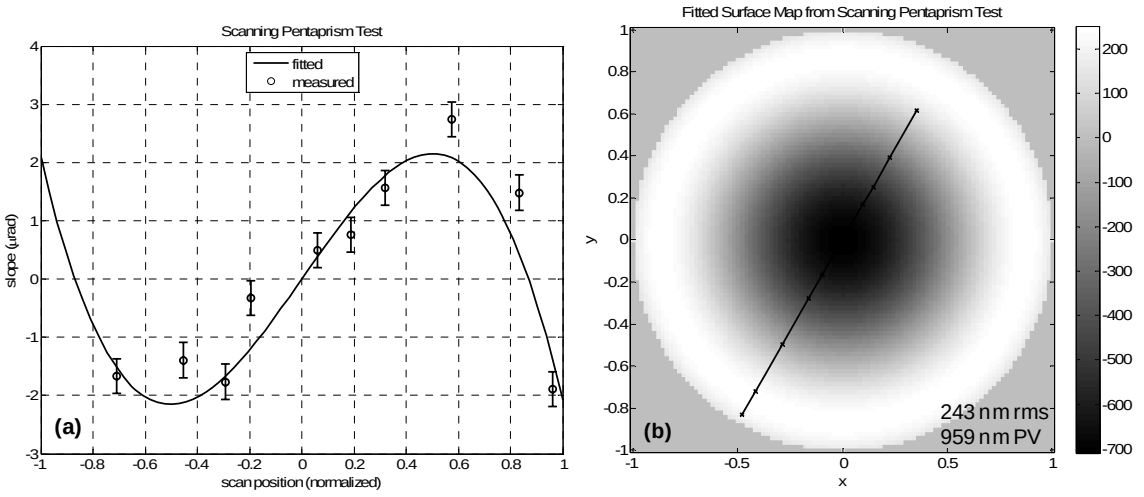

FIGURE 2.16. Measurements on the 1.6 m flat with the scanning pentaprism test. (a) Slope measurements and fit to the slope data. (b) A fitted surface map after determining the Zernike coefficients through a least squares fit.

TABLE 2.5. Zernike coefficients for power (Z4) and spherical aberration (Z9) after fits to the slope data.

	Electronic levels		Scanning pentaprism	
	rms (nm)	peak-valley (nm)	rms (nm)	peak-valley (nm)
Power	261	903	248	859
Spherical	-101	-339	-125	-420
Surface	245	941	243	959

TABLE 2.6. Difference in the Zernike coefficients for power (Z4) and spherical aberration (Z9), and the overall surface.

	Difference	
	rms (nm)	peak-valley (nm)
Power	13	44
Spherical	24	81
Surface	2	18

In addition to the different sampling spacing, the measurements between the electronic levels and the scanning pentaprism differed for two reasons:

1. The measurement accuracy of the electronic levels is 16 nm rms for power and 8 nm rms for spherical aberration (provided in Section 2.3.2). The measurement accuracy of the scanning pentaprism is 9 nm rms for power and 2 nm rms for spherical aberration (provided in Section 3.4.8).
2. The measurement sampling is about 40 mm for the scanning pentaprism (spot size on the test mirror), and about 140 mm for the electronic levels (contact points spacing).

This causes the same effect as averaging the surface slopes over the measurement sampling, but it is less of a problem for low order aberrations sampling.

The results of the comparison show that both test systems agree to within the measurement accuracy of the electronic levels, thus validating the electronic levels measurements.

2.6. Implementation with Dual Axis Electronic Levels

The scanning arrangements shown in Section 2.3.3 can be accomplished more efficiently with dual axis electronic levels as shown in Figure 2.17. Dual axis levels can measure two orthogonal axes simultaneously: the pointing direction and the direction orthogonal to it. Although we did not procure dual axis levels during the work reported here, they are available commercially. In this section, we analyze the performance of such levels through Monte Carlo simulations assuming the same type of measurement accuracies for both axes as for the uni-axis levels.

The data reduction remains the same for the dual axis levels. Slopes in orthogonal directions will be known for each measurement point; the common pointing of the levels must still be maintained. The errors contributing to uncertainty in the measurement can be treated in the same manner as for the uni-axis levels. With dual axis levels, measurements on a square grid can be made instead of scans through the center of the mirror to take advantage of the slope information in orthogonal axes (Figure 2.18).

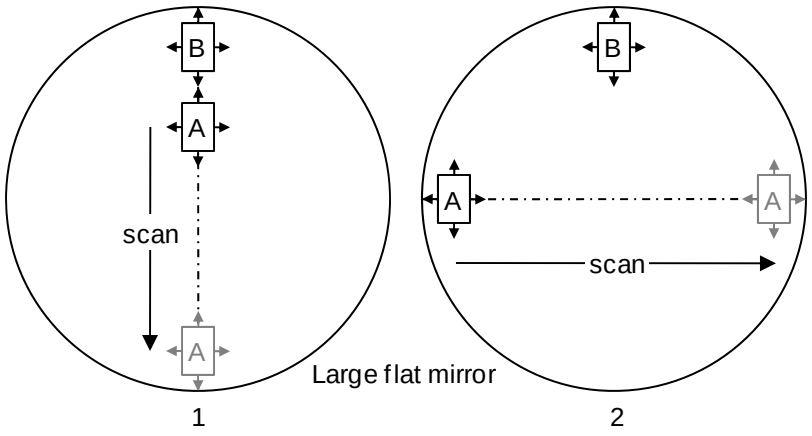

FIGURE 2.17. Schematic of performing simultaneous orthogonal measurements with dual axis levels. The advantage of dual axis levels over uni-axis levels is measurement efficiency.

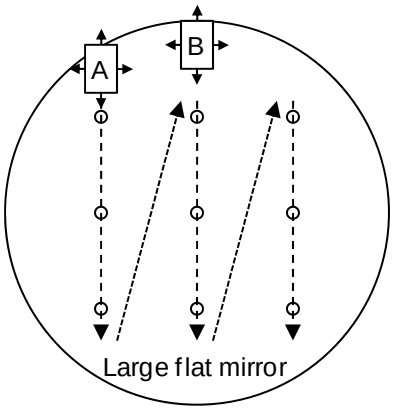

FIGURE 2.18. Potential sampling arrangement with the dual axis levels (nine measurement points on a square grid).

The sampling arrangement shown in Figure 2.18 can accomplished with three line scans with dual axis levels. Accomplishing the same scans with the uni-axis levels would require making six line scans, instead of three, demonstrating that dual axis levels can increase measurement efficiency.

Figure 2.19 shows the results of two measurement simulations with dual axis electronic levels. The sampling arrangements with dual axis levels shown in Figure 2.19 do not adequately sample astigmatism. To fix this, additional measurements on a rotated measurement grid is required.

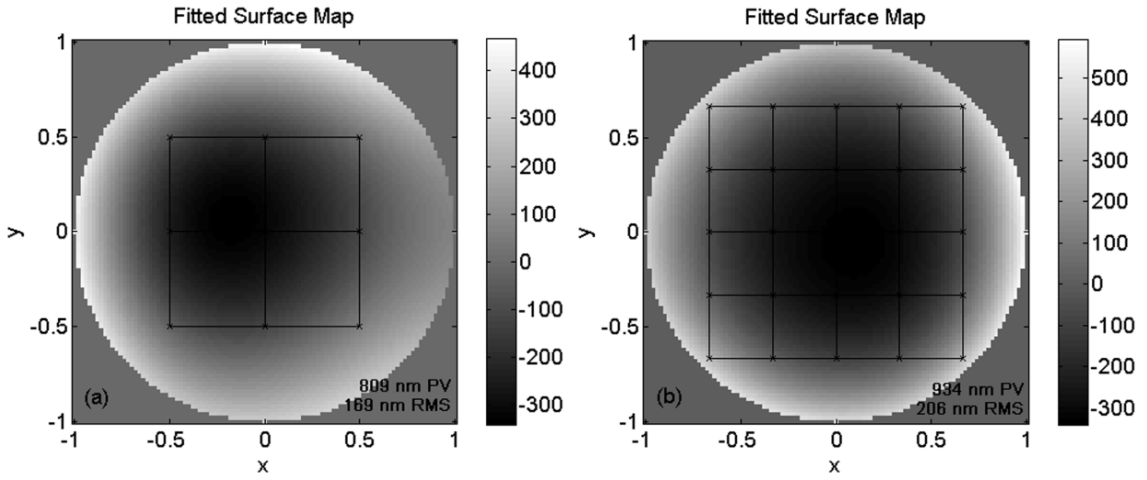

FIGURE 2.19. A simulation result of dual axis levels measurement on a 3 × 3 (a) and 5 × 5 (b) square grids assuming the same level of measurement uncertainty as for the uni-axis levels.

The advantage provided by dual axis electronic levels is efficiency, providing twice the information in a single measurement. Due to this fact, UA-OEFF is interested in obtaining dual axis electronic levels to do flatness measurements on large flat mirrors in the future.

2.7. Conclusion

The conventional measurement methods of large flat mirrors are often difficult and expensive. We provided an analysis of a high precision electronic level measurement

system that uses gravity as a reference and measures flatness in large flat mirrors with an option to measure other low order aberrations. The sources of error that limit the accuracy of the system were quantified; the errors are minimized through data averaging, using a guide rail, and making reference measurements. A Monte Carlo simulation of the system performance was performed based on the measurement uncertainty estimated from the error analysis. The simulation result showed the uncertainty in the measured low order Zernike aberrations and measurements to 50 nm rms of low order aberrations are achievable for 2 m class flat mirrors. The accuracy, efficiency, and low cost of the test system are ideal for testing of large flat mirrors. This test system can be used to guide polishing during the early stages of manufacture. In addition, the portability of the test system allows the test flat to be tested on the polishing table without moving the test flat to a testing fixture.

CHAPTER 3

ANALYSIS OF A SCANNING PENTAPRISM SYSTEM FOR MEASUREMENTS OF LARGE FLAT MIRRORS

We present an absolute test used to determine shape errors in large flat mirrors by measuring slope variations across the surface. The system uses two pentaprisms aligned to a high resolution electronic autocollimator. The pentaprisms deflect the collimated beam from the autocollimator nominally by 90° to the mirror surface, and the beam then returns on itself. The collimated beam is scanned across the flat mirror using motion of one of the pentaprisms on a linear stage. Any additional deflection in the return beam from the scanning prism provides a direct measurement of the shape error in the mirror surface. Misalignments and motions in the autocollimator and prisms that occur during scanning introduce second order error influences to the return beam. An active feedback system aids in maintaining the alignment of the prisms to minimize the error influences. Using this methodology, we measured 11 nm rms power in a 1.6 meter diameter flat mirror. The system can be used in a scanning or non-scanning mode, which measures only θ dependent aberrations.

3.1. Introduction

This chapter describes and analyzes a highly accurate optical slope test for very large flat mirrors. The test system consisted of a high resolution electronic autocollimator and two pentaprisms. A second electronic autocollimator was used as part of an active feedback control system to maintain the angular alignment of the scanning pentaprism during the scanning operation.

In optical surface metrology, systems with pentaprism(s) are used where conventional interferometric testing would otherwise be difficult or limited [27-28]. Two commonly used methods for testing flat mirrors interferometrically are the Fizeau test and the Ritchey-Common test. Both tests, described in Chapter 1, have limitations in terms of size for the Fizeau test and difficulty in performing the test on large mirrors for the Ritchey-Common test. We have developed a slope test system that overcomes these limitations.

The scanning pentaprism test system is highly accurate for measuring flatness in large flat mirrors. The system performance is limited in accuracy by second order error influences due to coupling of misalignments and motions in the autocollimator, pentaprisms, and test surface, and beam and prism errors coupling into lateral motion of the scanning pentaprism. The system discussed in this chapter built on a previous scanning system, which was designed to deflect the autocollimator beam upward to a flat mirror suspended above the test site and used off the shelf hardware [27-28]. In contrast, the new system deflected the collimated beam down to where the large test mirror rested on stable mechanical supports and used custom hardware. In addition to custom

hardware, alignment and data analysis techniques were modified in an effort to make the system more stable and accurate. The entire integrated test system, although heavy (~200 kg), is kinematic and can be transported by a hoist.

3.1.1. Systems with pentaprisms

Pentaprisms are used to deflect light beams at a constant angle (nominally by 90°) regardless of its orientation in the line of sight direction. Various optical test systems and devices involving pentaprisms make use of this unique property. Many systems involving pentaprisms have been developed to measure optical surface errors by measuring surface slopes [27-30]. Simply integrating the slope data gives surface height profiles. Through multiple measurements of the optical surface in different directions, a full synthetic surface map can be obtained. Other systems with pentaprisms are used to aid in optical alignments or in optical recording heads. Sensitive optical alignments and error corrections are made possible by the ability of the pentaprisms to project collimated and nominally parallel reference beams onto optical surfaces. Efforts have been made to understand the error influences in pentaprism systems [31-33]. Some systems have been refined to make them more accurate and less sensitive to alignment and motion errors [31-43].

The scanning pentaprism system design and development is presented in Section 3.2. This includes the system hardware, integration and alignment. The results and performance for 1.6 m flat mirror measurements are presented in Section 3.3. Finally, an analysis of error sources that limit the accuracy of the system and Monte Carlo analysis

of the sensitivities of the Zernike aberrations to noise are presented in Section 3.4. The concluding remarks are provided in Section 3.5.

3.2. System Design and Development

3.2.1. Test concept

In this section we discuss the design and test concept of the scanning pentaprism system. A schematic diagram of the test set up is shown in Figure 3.1. Two pentaprisms were co-aligned to a high resolution electronic autocollimator. Both prisms deflected the collimated beam from the autocollimator nominally by 90° to the mirror surface. The beams reflected off the test surface and returned to the autocollimator where small angle deviations revealed slope errors in the mirror surface.

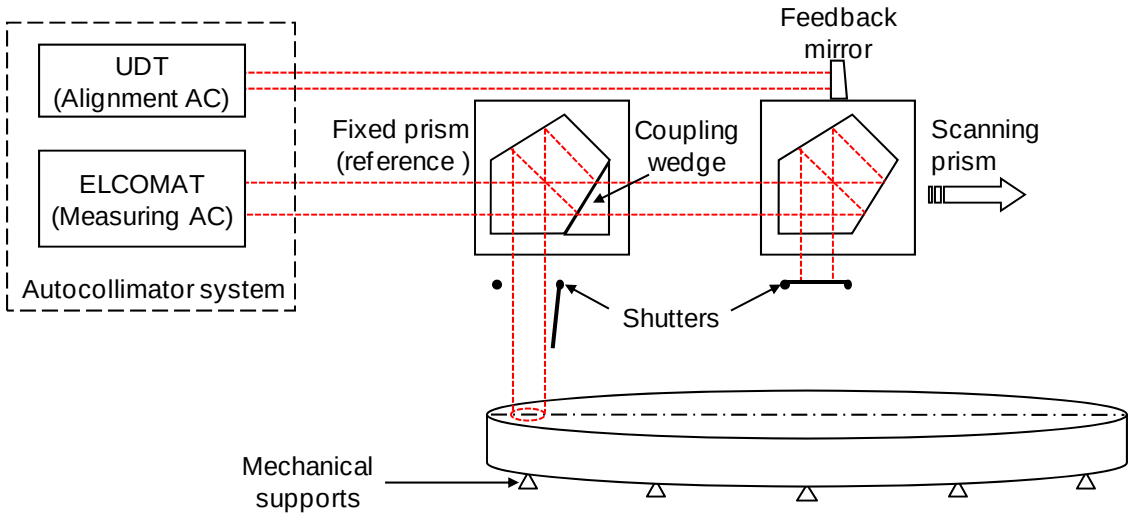

FIGURE 3.1. Schematic of the scanning pentaprism test system. The system used two electronic autocollimators (measurement and alignment) and two pentaprisms aligned to the measurement autocollimator.

The system can be used in a scanning or non-scanning mode. In the scanning mode, the reference prism remained fixed while the scanning prism was translated over the mirror surface. Since the autocollimator can only measure one return signal at a time, electronic shutters were used to alternately select the reference path and the scanning path. By taking a difference between the two prisms, the measurements became insensitive to the motion of the mirror or the autocollimator in the measurement direction or pitch (defined in Figure 3.2). An integration of the slope data provided surface height profiles along the scanning direction. The alternative method to integration is to fit low order slope functions derived from the Zernike polynomials to the slope data through a least squares calculation. The description of this method was given in Chapter two. Two dimensional surface topology maps were then generated from the Zernike polynomials after several scans at different orientations over the mirror.

In the non-scanning mode, both prisms remained fixed and the flat mirror under test was rotated while data was acquired continuously. Typically, the reference prism was positioned at one edge of the mirror, and the scanning prism was positioned at the center of the mirror. The non-scanning mode measured only θ dependent aberrations such as astigmatism (2θ) and trefoil (3θ).

The pentaprism system allowed slope determination only in the scan direction. We call this direction the line of sight pitch or in-scan direction. The prism degrees of freedom (pitch, yaw, and roll) are defined in Figure 3.2. Coupling between misalignments and motions of the prisms, autocollimator, and test surface in these degrees of freedom caused second order error influences to the beam line of sight.

Careful alignment of the scanning prism is required to minimize these errors. A second autocollimator (UDT shown in Figure 3.1), aligned to a small return mirror attached to the scanning pentaprism, was used to maintain the scanning pentaprism in angular alignment through an active feedback control. Sources of line of sight errors up to second order are listed in Table 3.1. The line of sight pitch varies linearly with the autocollimator and test surface pitch angles, and quadratically with other angular parameters. The first order effect of the autocollimator and test surface pitch motions were common to both the fixed and scanning prisms, so it was eliminated by performing differential measurements between the reference and scanning prisms.

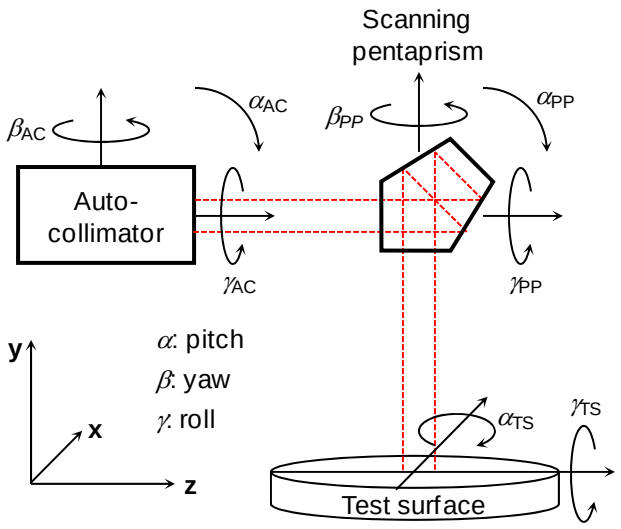

FIGURE 3.2. Coordinate system and definition of the degrees of freedom for the autocollimator, scanning pentaprism and the test surface.

TABLE. 3.1. Complete list of the line of sight alignment errors. Only the second order errors contribute to the in-scan slope error.

Contributions to line-of-sight pitch (in-scan direction)	Contributions to line-of-sight roll (cross-scan direction)
α_{AC}	β_{AC}
α_{TS}	β_{PP}
γ_{PP}^2	γ_{PP}
$\gamma_{AC} \times \gamma_{PP}$	γ_{TS}
$\gamma_{AC} \times \beta_{PP}$	$\alpha_{AC} \times \beta_{PP}$
$\gamma_{AC} \times \gamma_{TS}$	$\alpha_{AC} \times \beta_{TS}$
$\gamma_{TS} \times \gamma_{PP}$	$\alpha_{AC} \times \gamma_{AC}$
$\gamma_{TS} \times \beta_{PP}$	$\alpha_{AC} \times \gamma_{PP}$
α: pitch β: yaw γ: roll	AC: autocollimator PP: pentaprism TS: test surface

Pentaprism pitch motion sensitivity

Small pitch motion of the pentaprism was expected. This motion, however, had no effect on the beam deviation in the in-scan direction. This is the beauty of the pentaprism: the input beam is deviated at a constant (nominally) 90° angle, independent of small pitch errors. We take advantage of this property. As mentioned previously, this property makes the pentaprisms useful as reference beam projectors.

Pentaprism yaw and roll motion sensitivities

The in-scan (vertical) and cross-scan (horizontal) angles are coupled for yaw and roll motions of the pentaprism. The dependence is linear for yaw motion and quadratic for roll motion [31-33].

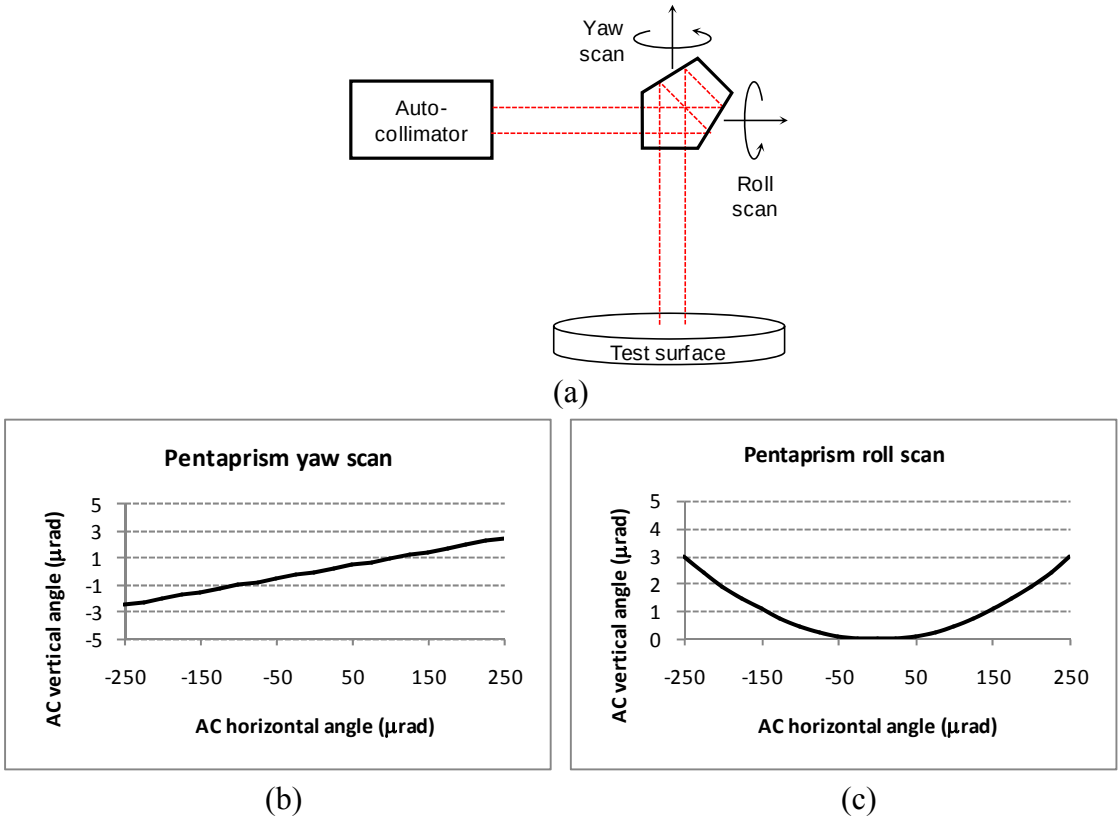

FIGURE 3.3. (a) Pentaprism yaw and roll scans. (b) Linear dependence of the angle measured with the autocollimator on the yaw angle of the prism. (c) Quadratic dependence of the angle measured with the autocollimator on the roll angle of the prism.

Any misalignments in yaw and roll couple with autocollimator, pentaprism, and test surface motions to cause second order errors. If the pentaprism is aligned, however, then the spot motion is the same for pentaprism roll and yaw motions. The in-scan

measurement is then perpendicular to the spot motion caused by motions in pentaprism roll and yaw. The noise over the amount of motions in roll and yaw gives the accuracy of the alignment. For example, if the yaw and roll alignments of the pentaprism are maintained to 50 μrad, the line of sight pitch will vary by less than 10 nrad (shown in Section 3.4.2).

Information from pentaprism yaw motion can be used to align both the autocollimator roll and the prism roll (Section 3.2.4). Geckeler [31-33] derives the slope of the autocollimator angle readings (vertical versus horizontal) from the yaw scan as

$$M_{\text{scan}}^{\text{yaw}} = \alpha_{\text{TS}} - \alpha_{\text{AC}}, \tag{3.1}$$

which reveals information on the difference of the roll angles of the autocollimator and the test surface. The autocollimator roll is aligned relative to the test surface when the slope, *M*, becomes zero. In addition, Geckeler [31-33] derives the minimum of the parabola from the pentaprism roll scan (vertical versus horizontal) as

$$H_{\text{scan}}^{\text{roll}} = \beta_{\text{PP}} - \beta_{\text{AC}} + 0.5 M_{\text{scan}}^{\text{yaw}}, \tag{3.2}$$

which depends on the pentaprism yaw, autocollimator yaw, and the result of the pentaprism yaw scan. Both Equations 3.1 and 3.2 have dependence on pentaprism yaw, thus prism yaw can be used to align autocollimator roll (from Equation 3.1) and prism roll (from Equation 3.2).

Beam collimation errors and alignment to the prism motion

The errors in the autocollimator collimated beam couple with lateral pentaprism motion to cause second order slope errors. We estimated that this effect caused 280 nrad slope

change per 1 mm of lateral prism motion. This linear motion was aligned to less than 0.5 mm along the beam, so the effect was limited to 140 nrad surface slope variation (discussed in Section 3.4.7).

3.2.2. System hardware

In this section, we describe the major components of the system. This includes the mechanical and optical hardware and measurement units.

Optical rails

A major improvement in stability over the previous system was in the mechanical stage used for the scanning operation. The current and new rail system consisted of two 2.5 m heavy duty steel rails spaced 20 cm apart and bridged by the pentaprism and autocollimator platforms, as shown in Figure 3.4. The straightness of the rail system was measured with a laser tracker to better than 0.05 mm/m, a significant improvement over the previous rail system. The advantage of the new rail system was that it limited the lateral and angular motion of the scanning pentaprism, resulting in less reliance on the active feedback control system. In addition, the new rail system was less susceptible to vibrations and warping, which were notable drawbacks of the previous system. The new rails and the feedback control system maintained the alignment of the pentaprisms to within 50 μrad in roll and yaw. The rail system rested on a three point kinematic base, which allowed the test system to be removed and stowed when not in use.

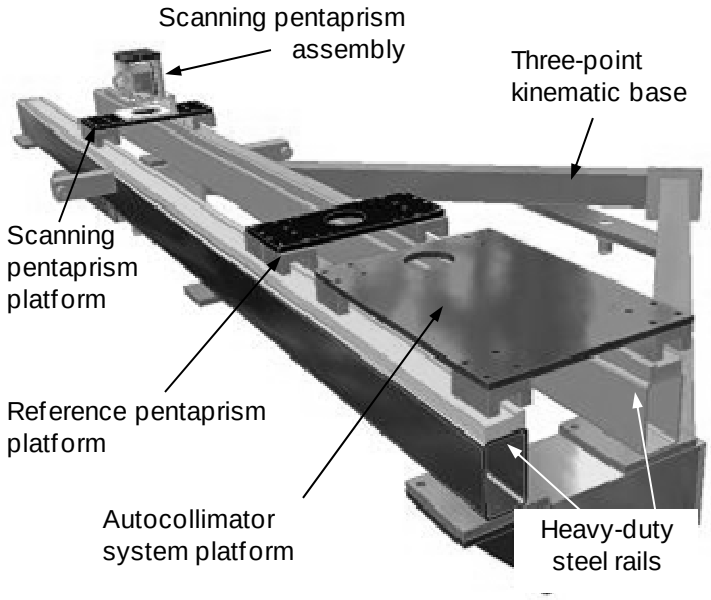

FIGURE 3.4. Solid model of the scanning pentaprism rail system showing the mounting platforms and the three point kinematic base.

Autocollimators

We used two electronic autocollimators. The first was a high resolution autocollimator (Elcomat 2000 made by Moller-Wedel [44]) used for the surface slope measurements. The Elcomat 2000 provided a 40 mm collimated beam, which was projected onto the mirror surface using the two pentaprisms (as described previously). The reflected beam was detected by the Elcomat and angle deviations caused by slope variations in the mirror surface were measured. The Elcomat also functioned as part of the active feedback control system that monitored cross-scan motion due to prism roll and yaw motions.

The second autocollimator had less angular resolution (model 3700 made by United Detector Technologies [45]). The UDT 3700 autocollimator was aligned to a return flat mirror that was attached to the scanning pentaprism assembly (see Figure 3.1

or 3.5). The UDT autocollimator was the main component of the active feedback control used to monitor the yaw motions of the scanning pentaprism. The UDT autocollimator was insensitive to roll motion of the pentaprism, but the Elcomat sensed the line of sight roll, which was caused by the combination of the prism roll and yaw motions. The prism roll was determined as the difference between the line of sight roll and the prism yaw. The UDT helped decouple the motions for the Elcomat. The feedback control then maintained both the roll and yaw alignment of the scanning pentaprism to better than 50 μrad (see Section 3.4.2).

Pentaprisms and pentaprism mounts

The first (reference) pentaprism had a coupling wedge that allowed about 50% transmission of the beam to the second (scanning) pentaprism, as shown schematically in Figure 3.1. We estimated measuring through the reference prism with the wedge caused about 50 nrad rms measurement error in the scanning mode (see Section 3.5.2).

The pentaprism holders provided secure mounts and remote adjustment of prism yaw and roll through Pico-motor™ linear actuators (see Figure 3.5). The Pico-motor™ actuators were controlled through the feedback control system; any misalignments of prisms were fixed with sending commands to the Pico-motors™ to drive the prisms back into alignment. The prism assemblies were mounted on rail cars, which moved on the two parallel steel rails.

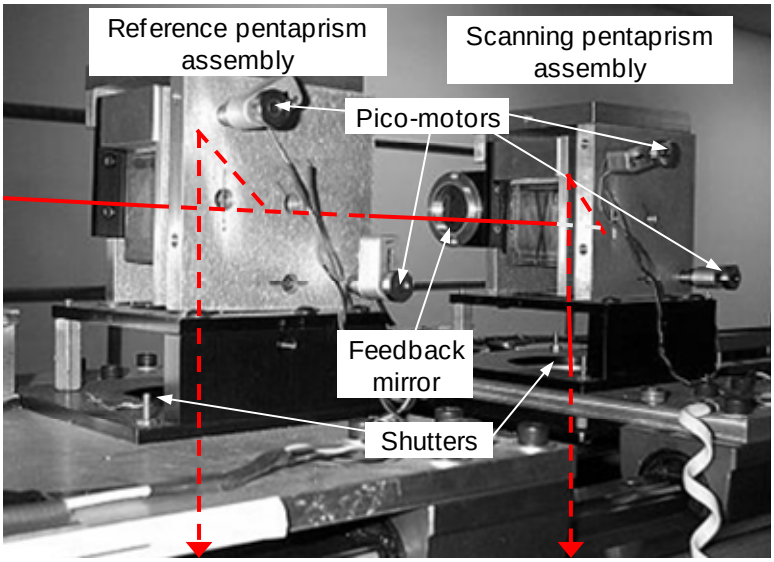

FIGURE 3.5. Pentaprism assemblies integrated into the system. Electronically controlled shutters are located at the exit face of each prism. The autocollimator system (not shown) is mounted to the left.

Shutters

We used two electronically controlled shutters. The shutters were mounted between the prisms and the test mirror, as shown in Figure 3.5. The shutters allowed alternating measurements between the prisms. Shutter *A* was open and shutter *B* was closed when measuring though the reference prism occurred. The shutter states were reversed when measuring through the scanning prism occurred. A delay of a few seconds between shutter operation and data acquisition allowed vibrations caused by the shutters to damp out.

Wedge plate for pentaprism apex angle error compensation

The reference pentaprism had a noticeable apex angle error. The beam deviation of this pentaprism was $90° + \varphi$, where φ is the additional beam deflection caused by the error in the prism apex angle. A wedge plate was inserted at the output of the reference prism to compensate for the additional beam deflection. We assumed the wedge plate introduced negligible errors to the measurement.

3.2.3. System integration

The system can be thought of as an assembly of subsystems. The subsystems included

1. Autocollimator system,
2. Reference pentaprism assembly,
3. Scanning pentaprism assembly, and
4. Electronics including the workstation and software for the active feedback control.

The rail system is the foundation upon which these subsystems were integrated (see Figure 3.5). Subsystems one through three were mounted on separate carriage platforms. The platforms can slide on the rail tracks. Subsystems one and two were locked into position at one end of the rails. The scanning pentaprism assembly, or subsystem three, was allowed to translate over the rails. The electronics and cabling for feedback control were housed in a breakout box and mounted underneath the autocollimator system platform (not visible in Figure 3.6).

The fully integrated system is shown in Figure 3.6. The entire system can be lifted with a hoist and positioned kinematically over the large mirror.

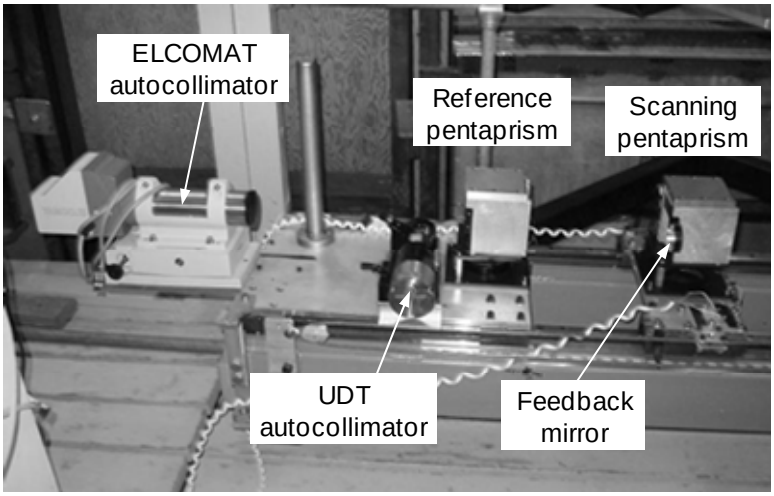

FIGURE 3.6. A fully integrated and operational scanning pentaprism test system. The vertical post next to the Elcomat was used to mount a He-Ne laser for the initial alignment of the system. Cabling attached to the pentaprism assemblies are used to control the Pico-motors™ through active feedback. The UDT beam is folded with a 50 mm mirror to the feedback mirror.

3.2.4. System alignment

The accurate alignment of the system, especially of the pentaprisms, is essential to slope measurement accuracy [27-40]. The system alignment was performed in several steps described below.

1) The large flat mirror rested on stable mechanical supports and a high performance rotary air bearing table, which was initially leveled to gravity. The pentaprism rails were also initially leveled to gravity, thus tilt between the test surface and the rails was minimized from the beginning.

2) A standard He-Ne laser was mounted in place of the measuring autocollimator. The laser was aligned to the rails by placing a crosshair target on the scanning pentaprism assembly, then pointing the laser at the crosshair while sliding the penataprism assembly

back and forth along the rails (shown schematically in Figure 3.7). After the laser was well aligned to the rails (less than 0.25 mm/m), the scanning pentaprism was parked at the furthest point on the rails opposite the reference pentaprism.

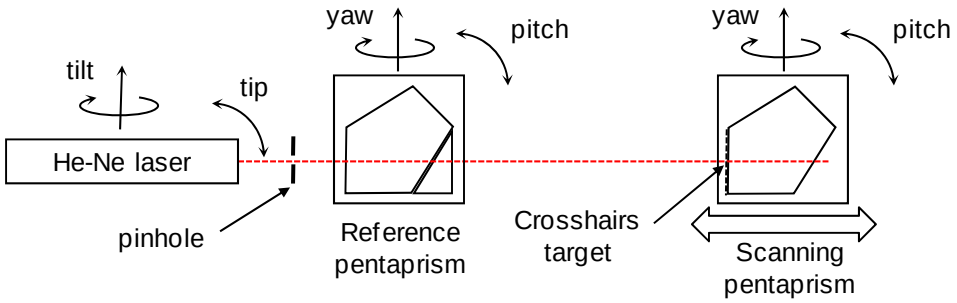

FIGURE 3.7. Schematic showing the initial alignment of the pentaprisms in yaw. The laser was reflected off the front faces of the prisms.

3) The crosshair target was removed, and both prisms were aligned in yaw by walking the laser return spots (from the prism faces) through a pinhole placed after the laser (see Figure 3.7). This procedure allowed the initial alignment of the scanning pentaprism in yaw to better than 120 μrad.

4) The roll motion of the reference pentaprism was aligned by opening one shutter, reflecting the laser beam off the test mirror, and adjusting the roll of the pentaprism until the reflected laser spot returned through the pinhole. The procedure was repeated for the scanning prism. At this point the initial alignment of the scanning prism roll was also better than 120 μrad.

5) Next, a return flat mirror (50 mm diameter) was placed in the path of the laser beam just before the scanning pentaprism. The return mirror was secured and adjusted until the

reflected laser beam returned through the pinhole. The laser and the pinhole were removed, and the measuring autocollimator was put in place. The autocollimator was aligned to the return mirror in both the horizontal and vertical axes. At this point the autocollimator was aligned to the rails and the pentaprisms to better than 120 μrad.

6) The fine alignment was performed iteratively using the read-out of the autocollimator. While the test surface remained fixed, adjustments were made to the autocollimator and the pentaprisms. Table 3.1 lists the angular motions that affected the beam line of sight pointing (pentaprism yaw and roll and autocollimator roll). These are the motions that required alignment. First, the reference pentaprism was scanned in yaw by approximately ±250 μrad, and the autocollimator horizontal and vertical angle readings were observed. The behavior of this motion is linear on the angle readings (vertical versus horizontal angle) [31-33]. A finite slope in the angle readings indicated a misalignment between the autocollimator and test surface in roll [33]. With the test surface fixed, adjustment was made to the autocollimator to minimize this misalignment. After adjusting the roll of the autocollimator, the prism was re-scanned in yaw. Roll of the autocollimator was aligned when the angle readings were no longer coupled for the prism yaw scan. The procedure was repeated for the scanning prism. The autocollimator roll was now aligned to better than 50 μrad.

7) Next, the reference prism was scanned in roll by approximately ±250 μrad, and the autocollimator horizontal and vertical angle readings were observed. The behavior of this motion is quadratic on the angle readings (vertical versus horizontal angle) [31-33]. Any coupled readings indicated a misalignment of the prism in yaw. Yaw of the prism

was adjusted, and the prism was then re-scanned in roll. The prism yaw was aligned when no noticeable coupling remained between the angle readings during the roll scans. At this point, the roll motion was constrained to the vicinity of the quadratic minimum [33]. This procedure was repeated for the scanning prism. Yaw and roll for both prisms were now aligned to better than 50 μrad. At this point, the system was aligned and ready to use.

3.3. System Performance

The scanning pentaprism system can be used in two modes: scanning and staring (non-scanning). Diagonal surface scans were performed in the scanning mode (see Figure 3.8). In the staring mode, circumferential scans were performed where both prisms remained fixed and the test flat rotated continuously while data was acquired (see Figure 3.12).

3.3.1. Diagonal line scans: scanning mode

In the scanning mode, the reference prism remained fixed and the scanning prism was scanned across the diameter of the mirror. A diagram of three scan paths is shown in Figure 3.8. This was achieved by rotating the test flat to two other positions after the first scan. Using these three scans measured most of the low order aberrations [46]. The results of three line scans are not presented here, but a similar measurement with electronic levels was given and analyzed in Chapter two.

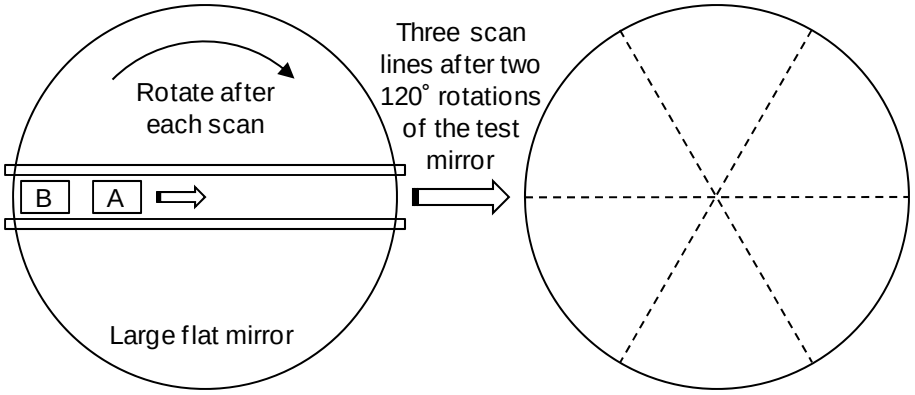

FIGURE 3.8. Schematic showing three line scans with the scanning pentaprism. This example shows the mirror being rotated in 120° steps for each scan.

A single diagonal scan measures only rotationally symmetric aberrations, as presented in Chapter two. Figure 3.9 shows the result of a single diagonal scan on the finished 1.6 m flat mirror. The results from the interferometer measurements showed that the surface contained mainly symmetric errors (see Figure 3.11). Power was the main surface error of interest, so only a single line scan was performed. Forward and backward scans were performed for the same diagonal line, and the data were averaged. Only the slope functions derived from the symmetric Zernike polynomials were fit to the slope data. The linear component of the polynomial fit to the slope data then revealed power in the flat mirror surface. This measurement yielded 11 nm rms in power.

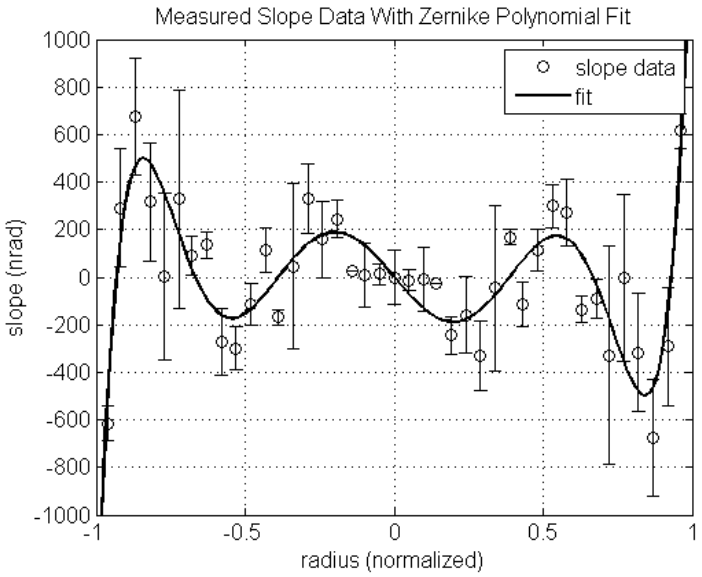

FIGURE 3.9. Surface slope measurements with the scanning pentaprism system and a low order polynomial fit. A linear component of the polynomial fit to the slope data gives information on power in the surface (11 nm rms).

Comparison to interferometric data

A radially normalized plot showing the scanning pentaprism slope data in comparison to the Fizeau interferometer data for the 1.6 m test flat is shown in Figure 3.10. The figure shows that the scanning pentaprism data and interferometer data, first differentiated to obtain the surface slope, have no significant differences, except at the very edge where high slopes were observed. The rms difference is about 160 nrad after removing the edge point, which is within the accuracy (given in Section 3.4) of the scanning pentaprism test in the scanning mode. The large Fizeau interferometer cannot measure power, so the interferometer data was adjusted for power before the comparison. The description of the large Fizeau interferometer is given in Chapter four.

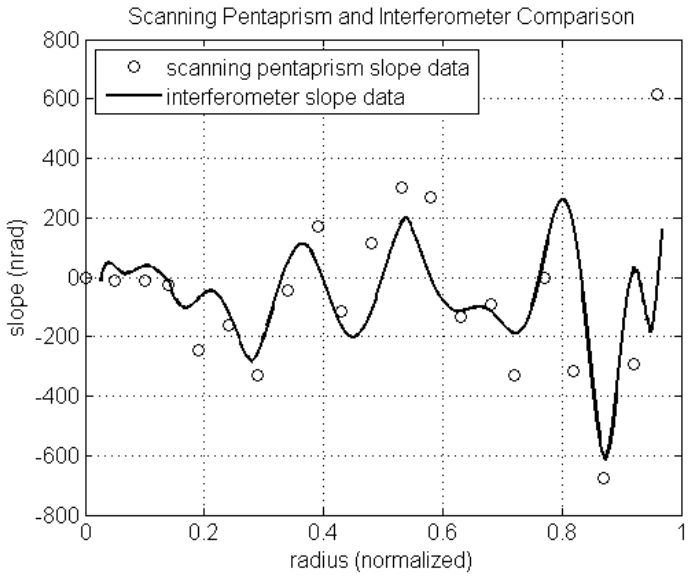

FIGURE 3.10. Comparison of the scanning pentaprism and the interferometer data. The interferometer data was first diffentiated to get surface slope.

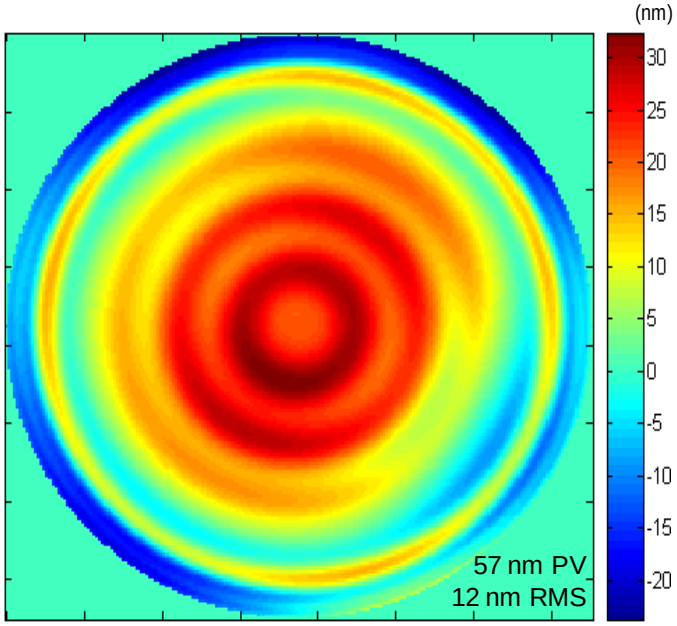

FIGURE 3.11. Fizeau interferometer measurement on the 1.6 m flat mirror.

The Fizeau interferometer used a 1 m custom reference flat and subaperture testing to measure the 1.6 m flat mirror [47]. The surface map, shown in Figure 3.11, is on the finished mirror after combining the subaperture measurements.

3.3.2. Circumferential scans: staring mode

The circumferential scans provided information on aberrations that have θ dependence such as astigmatism (2θ) and trefoil (3θ). Tilt between the autocollimator and the test surface has a 1θ dependence. The main aberration measured in this mode was astigmatism.

In the circumferential scans, both pentaprisms were fixed and the flat mirror was continuously rotated (see Figure 3.12). The slope data were continuously acquired for several full rotations of the flat mirror. The data were then averaged.

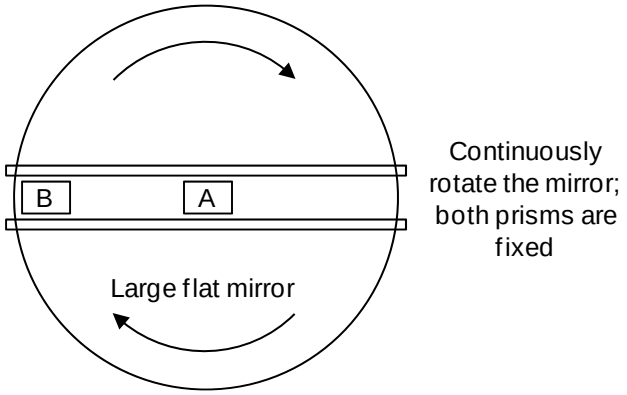

FIGURE 3.12. Circumferential scans, where both prisms were fixed and the mirror was continuously rotated, measured astigmatism and other θ dependent aberrations in the mirror surface.

For the scans shown in Figure 3.13a, the reference pentaprism (*B*) was parked near the edge of the large flat mirror, and the scanning pentaprism (*A*) was parked at the center of the mirror. These measurements were performed while the mirror was in production. The difference between the scans (Figure 3.13b) reveals the amount of contributions of low order aberrations with θ dependence (dominated by tilt).

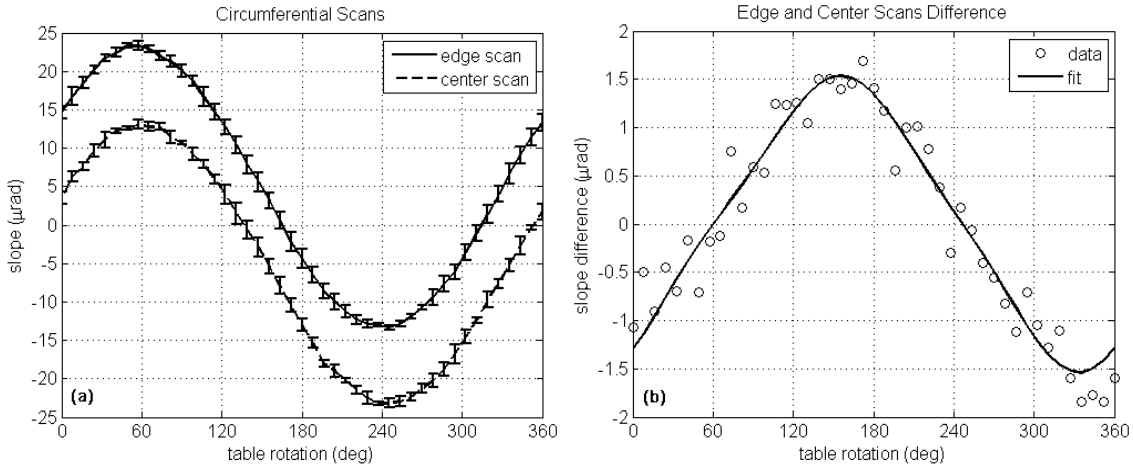

FIGURE 3.13. Circumferential scans at the center and edge of the large flat mirror (a), and difference in the scans and fit (b). The error bars in the scans indicate good stability of the rotary air bearing table.

A least squares fit of the difference data was performed using a fitting function of the form

$$f = a_0 + a_1 \sin(\theta) + b_1 \cos(\theta) + a_2 \sin(2\theta) + b_2 \cos(2\theta) + a_3 \sin(3\theta) + b_3 \cos(3\theta). \tag{3.3}$$

Table 3.2 lists the aberrations with θ dependence and their coefficient values after the fit. The last column shows the equivalent surface error for each θ dependent aberration.

TABLE 3.2. Aberrations with θ dependence measured with circumferential scans, fit coefficients and equivalent low order surface error.

Aberration term	Fit function term(s)	Fit coefficients (μrad)	Equivalent low order surface error
Piston	a_0	0.0294	---
Tilt	$a_1 \sin(\theta) + b_1 \cos(\theta)$	0.6328, -1.2888	359 nm rms
Astigmatism	$a_2 \sin(2\theta) + b_2 \cos(2\theta)$	0.0366, -0.0043	15 nm rms
Trefoil	$a_3 \sin(3\theta) + b_3 \cos(3\theta)$	0.0993, -0.0283	18 nm rms

3.4. Error Analysis

3.4.1. Errors to line of sight beam motion

There were several error sources that contributed to the line of sight beam pitch (or in-scan) motion. Below we describe the sources and quantify their effect on the beam line of sight.

3.4.2. Errors from angular motions of the pentaprisms, autocollimator and test surface

Taking the second order terms listed in Table 3.1, an expression for the change in the in-scan line of sight due to misalignments and angular motions of the pentaprism, autocollimator, and test surface can be derived as:

$$\Delta\alpha_{\mathrm{LOS}} = 2\gamma_{\mathrm{PP}}\cdot\Delta\gamma_{\mathrm{PP}} + \Delta\gamma_{\mathrm{AC}}\left(\gamma_{\mathrm{PP}} + \beta_{\mathrm{PP}} + \gamma_{\mathrm{TS}}\right) + \gamma_{\mathrm{AC}}\left(\Delta\gamma_{\mathrm{PP}} + \Delta\beta_{\mathrm{PP}} + \Delta\gamma_{\mathrm{TS}}\right) \qquad (3.4)$$
$$+ \Delta\gamma_{\mathrm{TS}}\left(\gamma_{\mathrm{PP}} + \beta_{\mathrm{PP}}\right) + \gamma_{\mathrm{TS}}\left(\Delta\gamma_{\mathrm{PP}} + \Delta\beta_{\mathrm{PP}}\right),$$

where each Δ term indicates the variation in prism, autocollimator, and test surface motion for that angle. Equation 3.4 shows motions of the three components coupling with misalignments to cause second order errors. Table 3.3 shows a summary of the error terms that coupled into the measurement in the in-scan direction, and Table 3.4 shows the amount of contribution from each error term in Equation 3.4.

TABLE 3.3. Budget for alignment errors for the scanning pentaprism system.

Parameter	Description	Tolerance
γ_{PP}	Initial misalignment of the prism roll	< 0.13 mrad
$\Delta\gamma_{\mathrm{PP}}$	Variation in prism roll	< 0.05 mrad rms
γ_{AC}	Misalignment of the autocollimator roll relative to direction of motion	< 0.10 mrad
$\Delta\gamma_{\mathrm{AC}}$	Variation in autocollimator roll	< 0.05 mrad rms
β_{PP}	Initial misalignment of the prism yaw	< 0.13 mrad
$\Delta\beta_{\mathrm{PP}}$	Variation in prism yaw	< 0.05 mrad rms
γ_{TS}	Misalignment of the test surface roll relative to the direction of motion	< 0.10 mrad
$\Delta\gamma_{\mathrm{TS}}$	Variation in test surface roll	< 0.01 mrad rms

TABLE 3.4. Misalignment and perturbation influences on the in-scan line of sight.

Contribution (terms from Eq. 3.4)	Amount of line of sight deviation (nrad rms)
$2\gamma_{PP} \times \Delta\gamma_{PP}$	13
$\Delta\gamma_{AC} \times \gamma_{PP}$	7
$\Delta\gamma_{AC} \times \beta_{PP}$	7
$\Delta\gamma_{AC} \times \gamma_{TS}$	5
$\gamma_{AC} \times \Delta\gamma_{PP}$	5
$\gamma_{AC} \times \Delta\beta_{PP}$	5
$\gamma_{AC} \times \Delta\gamma_{TS}$	1
$\Delta\gamma_{TS} \times \gamma_{PP}$	1
$\Delta\gamma_{TS} \times \beta_{PP}$	1
$\gamma_{TS} \times \Delta\gamma_{PP}$	5
$\gamma_{TS} \times \Delta\beta_{PP}$	5
Root sum square	**20**

3.4.3. Mapping error

The slope errors in the polished test surface were expected to be less than 2 nrad/mm rms. The position of the scanning prism (or the beam) on the test surface was known to better than 2 mm. The error due to the scanning prism position, thus, contributed about 4 nrad rms to the total error.

3.4.4. Thermal errors

The pentaprisms were made from BK7, which is fairly sensitive to temperature gradients (7.1×10^{-6}/°C). A linear temperature gradient in the prisms changes the index gradient and prism geometry. The thermal analysis showed that a temperature gradient of

0.01°C/meter in the pentaprisms would cause an additional beam deflection in the line of sight direction of 17 nrad [48]. The test system was used in scanning and staring modes (see Section 3.3). The time scale for the modes of operation was relatively short compared to the pentaprism's thermal time constant. In the scanning mode we estimated a single scan took one hour. For a full measurement, three scans were performed that required about three hours to complete. In the staring mode, a measurement typically took 10 to 15 minutes. Only the variation in temperature gradients during the 3 hour scan in scanning mode and 10 to 15 minute scan in staring mode contributed to the line of sight errors. The top level error budget allowed for change in the thermal gradient of ±0.04°C/meter for the scanning case and ±0.02°C/meter for the staring case. We then expected a line of sight error of up to 34 nrad rms and 17 nrad rms for scanning and staring cases, respectively.

3.4.5. Combined random errors

Table 3.5 shows the random errors for the pentaprism staring and scanning modes separately. There was an additional error in acquiring the measurements from the scanning pentaprism through the fixed pentaprism. This effect is included directly in Table 3.5.

TABLE 3.5. Pentaprism test system independent measurement errors assumed to be uncorrelated.

Error description	Staring mode (nrad rms)	Scanning mode (nrad rms)
Autocollimator measurement uncertainty (range dependent)[a]	140	160
Prism and beam angle variation	20	20
Mapping error	4	4
Thermal effects	17	34
Effect of reference prism error	25	50
Coupling of lateral motion	--	80
Root sum square	145	190

[a] manufacturer's specification.

3.4.6. Errors from coupling lateral motion of the pentaprisms

Phase or amplitude variations in the collimated beam did not affect the system performance to first order, because these effects were common to both pentaprisms. These variations, however, were coupled with lateral motion of the scanning prism relative to the collimated beam. Similarly, beam errors coupled with lateral motion of the scanning prism to cause second order errors. Coupling of phase errors, diffraction effects, beam non-uniformity, and prism errors with lateral motion of the pentaprisms for the scanning system was analyzed by Mallik et al [27-28]. This analysis for our system is not repeated here; our system had better control of the lateral motion of the pentaprisms. The lateral motion of the scanning prism in our system was aligned and maintained to 0.5 mm. The combined effect of these errors was then estimated to be 80 nrad rms.

3.4.7. Analysis of errors due to beam divergence

There was an additional error to consider that coupled into lateral motion of the pentaprism. For typical uses of electronic autocollimators, a collimated output beam is assumed. If the beam is slightly diverging, however, the angle readings are shifted by some amount proportional to the divergence angle. In the scanning pentaprism system, the effect of the beam divergence can couple into lateral motion of the pentaprism causing a second order error. To quantify this effect, a simple test was devised. A 13 mm circular aperture was placed at the output port of the measuring autocollimator. The aperture was shifted up and down (in the line of sight direction) by about 18 mm from the top edge of the beam to the bottom edge as shown in Figure 3.14, and the change in the vertical (*y*-axis) angle reading was recorded for the two aperture positions.

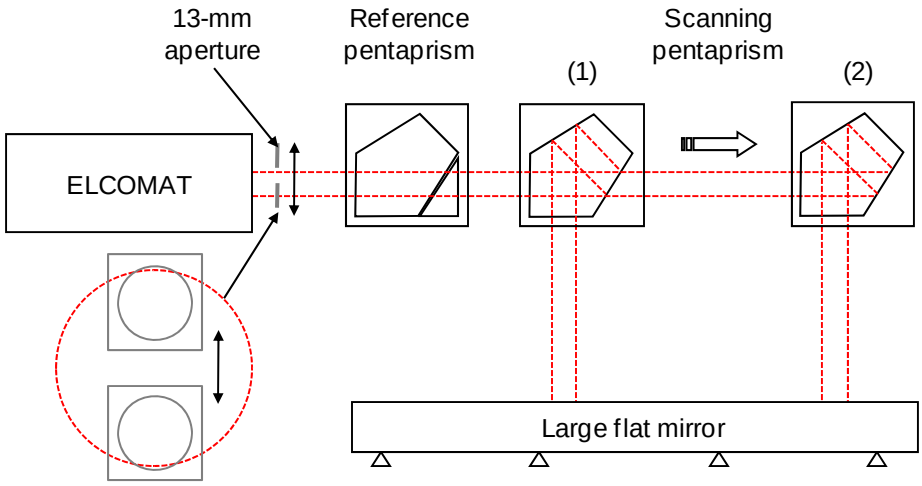

FIGURE 3.14. Schematic showing the test set up to measure the effect of beam divergence on lateral prism motion.

For the case when the scanning pentaprism was close to the reference prism (1), the change in the autocollimator *y*-axis angle reading was about 10 μrad. The scanning prism was then moved to the far edge of the flat mirror (2), and performed the aperture shifts. For this case, the change in the *y*-axis angle reading was about 15 μrad. From these measurements we can estimate that this effect caused 280 nrad slope change per 1 mm of lateral motion. The pentaprism linear motion was aligned to less than 0.5 mm along the beam, so the effect is limited to 140 nrad surface slope variation. This systematic slope variation of ±70 nrad corresponds to surface power of less than 8 nm rms.

3.4.8. Monte Carlo analysis of system performance

A Monte Carlo simulation on the three diagonal surface scans separated by 120° was performed to determine the uncertainty distributions of the low order Zernike aberrations using a noise of 0.3 μrad rms for a single differential measurement. This analysis assumed 42 measurement points per scan. From the simulation the measurement uncertainty of each of the low order aberrations can be estimated as shown in Table 3.6. The simulation result in Table 3.6 shows that a 2 m flat mirror can be measured to 14 nm rms of low order aberrations with the scanning pentaprism system after careful system alignment. The measurement of power has 8 nm rms due to the systematic effect listed above, limiting the surface power measurement to 9 nm rms.

TABLE 3.6. Scanning pentaprism measurement uncertainty for the low order Zernike aberrations assuming 0.3 μrad rms noise for a single differential measurement, three line scans, and 42 measurement points per scan.

Zernike aberration	Measurement accuracy (nm rms)
Power	9
Cos Astigmatism	8
Sin Astigmatism	8
Cos Coma	4
Sin Coma	4
Spherical	2
Secondary Spherical	2
Root sum square	16

3.4.9. Monte Carlo analysis of sensitivity to noise and number of measurement points per scan

Figures 3.15 through 3.17 show additional results of Monte Carlo simulations of the sensitivities of the low order Zernike aberrations to noise and the number of measurements points per scan. The analysis assumes three diagonal line scans (separated by 120°) across a 2 m flat mirror and measurement noise normalized to 1 μrad rms. The measurement spacing was varied for each number of measurement points to get a distribution of the measurement uncertainty.

The sensitivities should get better as $\frac{1}{\sqrt{N}}$, where N is the number of measurement points per scan. An equation of the form

$$\varepsilon = AN^{-1/2} \tag{3.5}$$

was, therefore, fitted to the data points, where ε is the measurement uncertainty and A is the sensitivity to noise. The coefficient A was determined that allowed that best fit through the data points. In addition to verifying the $\frac{1}{\sqrt{N}}$ effect on the measurement uncertainty, the analysis also shows that the sensitivities of the aberrations depend on the how the measurement points are distributed across the mirror diameter. For example, varying the sample spacing of the five measurement point across the mirror gives a distribution of the uncertainty values, as seen in the proceeding plots.

TABLE 3.7. Summary of the values of the sensitivity to noise for the proceeding plots (Figures 15 through 17).

	Power (Z4)	Cos Astigmatism (Z5)	Sin Astigmatism (Z6)	Cos Coma (Z7)	Sin Coma (Z8)	Spherical (Z9)
A	110	185	180	84	84	56

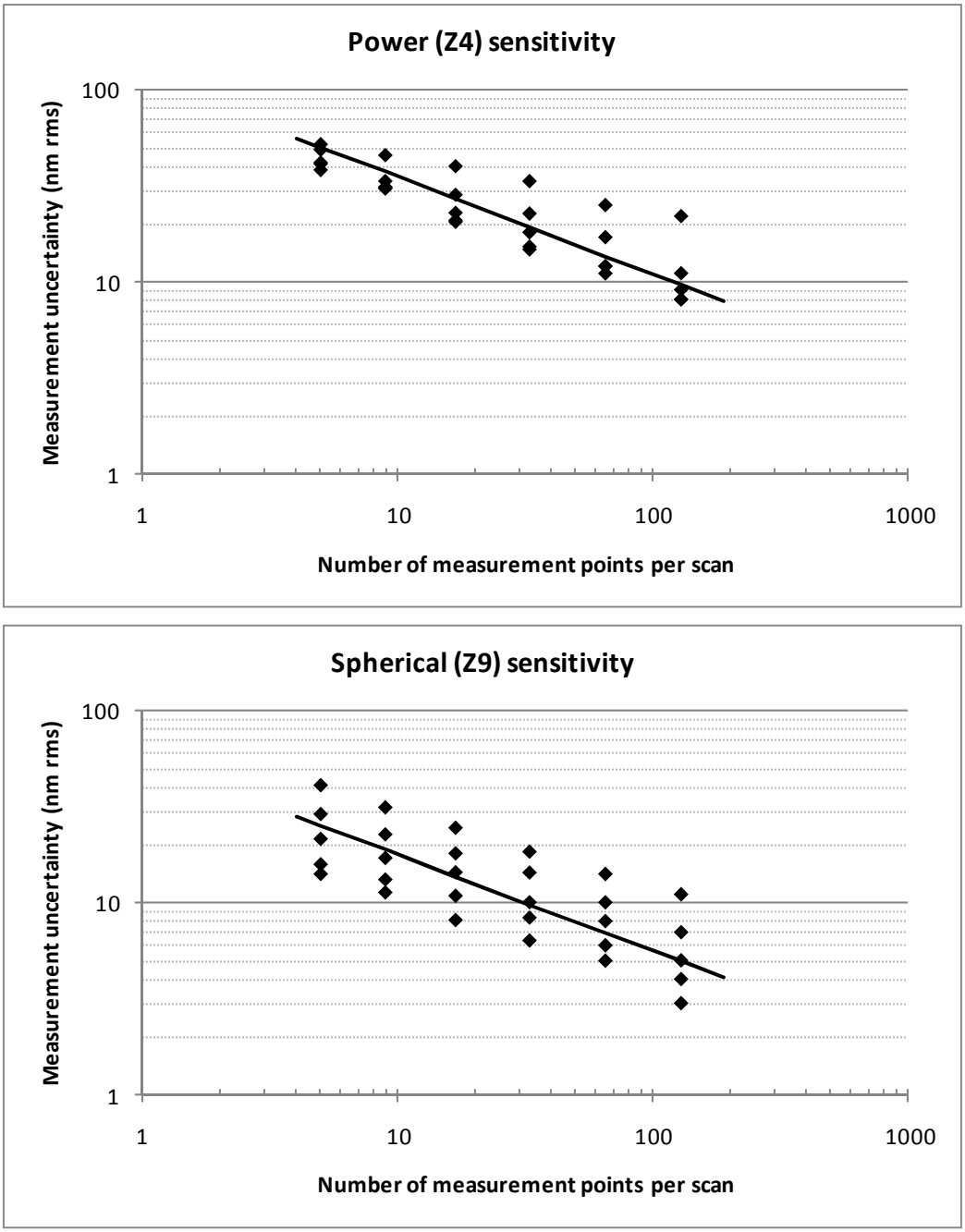

FIGURE 3.15. Power (Z4) and spherical aberration (Z9) sensitivity to noise and number of measurement points per scan. Three line scans (separated by 120˚) on a 2 m flat mirror and 1 μrad rms noise were assumed. A = 110 for power and A = 56 for spherical aberration.

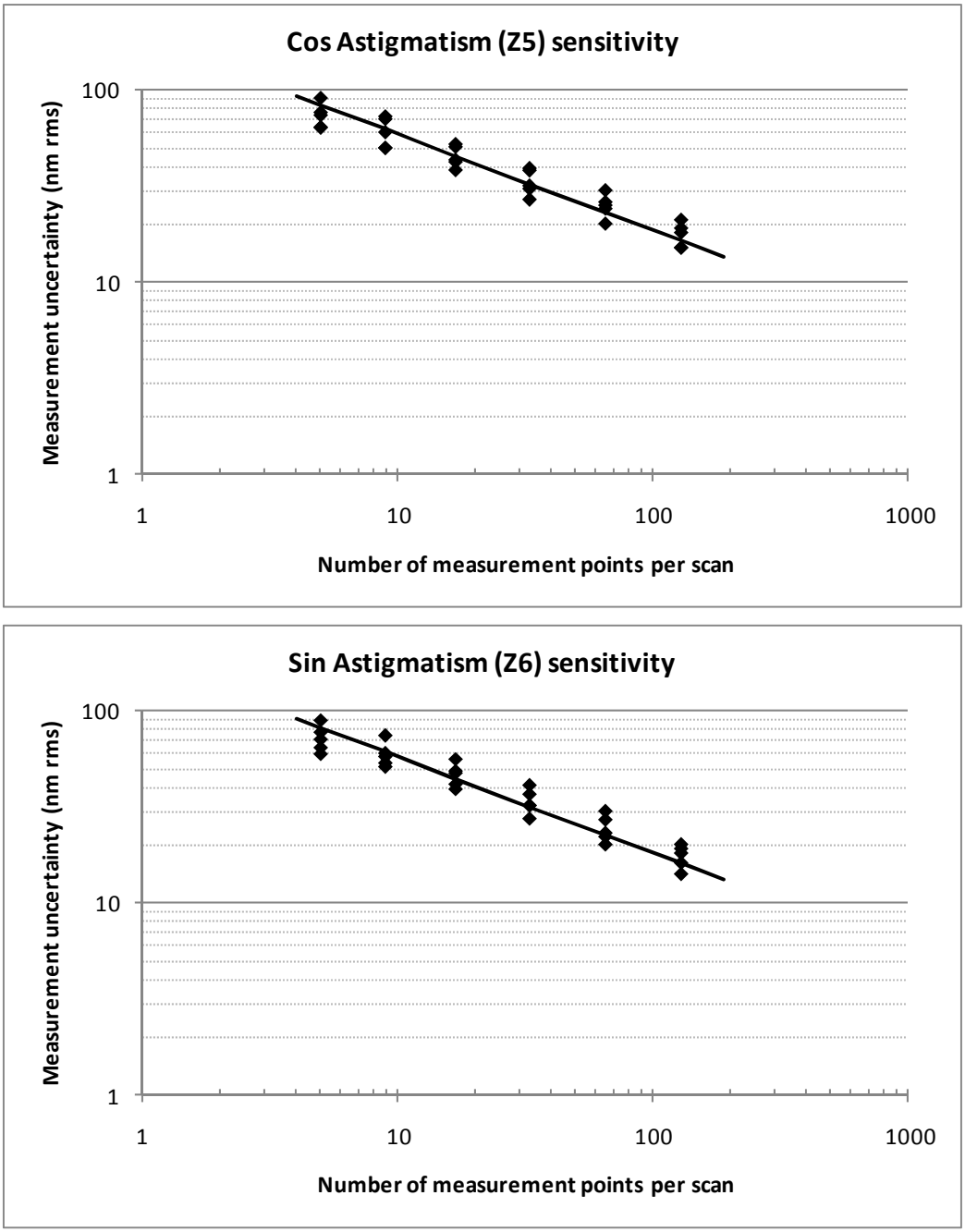

FIGURE 3.16. Astigmatism (Z5, Z6) sensitivity to noise and number of measurement points per scan. Three line scans (separated by 120˚) on a 2 m flat mirror and 1 μrad rms noise were assumed. A = 185 for cos astigmatism and A = 180 for sin astigmatism.

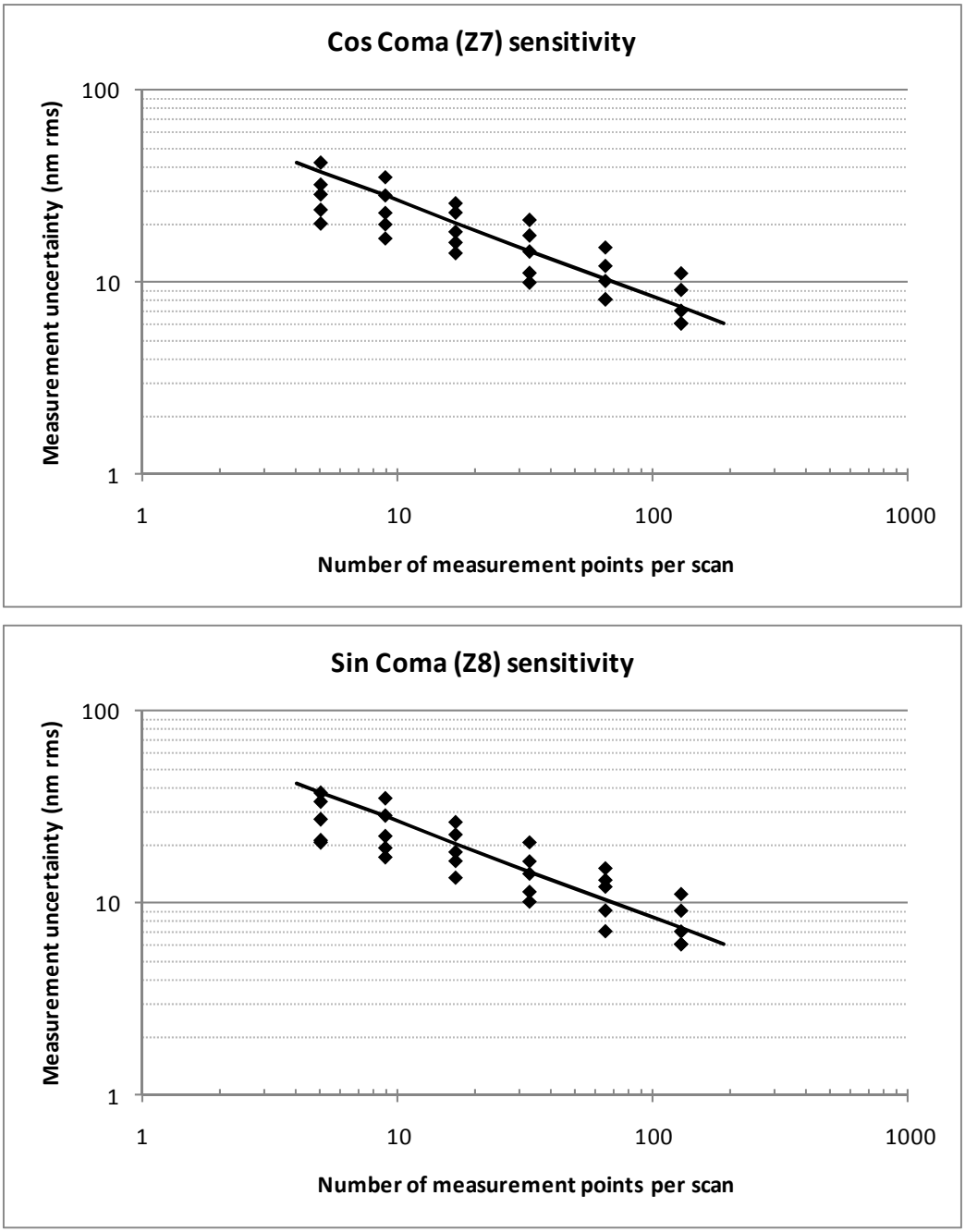

FIGURE 3.17. Coma (Z7, Z8) sensitivity to noise and number of measurement points per scan. Three line scans (separated by 120˚) on a 2 m flat mirror and 1 μrad rms noise were assumed. $A = 84$ for both components of coma.

TABLE 3.8. Definition of mid order Zernike (UofA) polynomials. The angle, θ, is measured counter clockwise from the *x*-axis, and the radial coordinate is the normalized dimensionless parameter, ρ.

Zernike term	Polynomial, $Z(\rho,\theta)$ rms
Z10 – cos trefoil	$\sqrt{8}\,\rho^3 \cos 3\theta$
Z11 – sin trefoil	$\sqrt{8}\,\rho^3 \sin 3\theta$
Z12 – cos secondary astigmatism	$\sqrt{10}\,(4\rho^2 - 3)\rho^2 \cos 2\theta$
Z13 – sin secondary astigmatism	$\sqrt{10}\,(4\rho^2 - 3)\rho^2 \sin 2\theta$
Z14 – cos secondary coma	$\sqrt{12}\,(10\rho^4 - 12\rho^2 + 3)\rho \cos\theta$
Z15 – sin secondary coma	$\sqrt{12}\,(10\rho^4 - 12\rho^2 + 3)\rho \sin\theta$
Z16 – secondary spherical	$\sqrt{7}\,(20\rho^6 - 30\rho^4 + 12\rho^2 - 1)$
Z17 – cos pentafoil	$\sqrt{10}\,\rho^4 \cos 4\theta$
Z18 – sin pentafoil	$\sqrt{10}\,\rho^4 \sin 4\theta$
Z25 – tertiary spherical	$\sqrt{9}\,70\rho^8 - 140\rho^6 + 90\rho^4 - 20\rho^2 + 1$

3.4.10. Monte Carlo analysis of noise coupling into mid order Zernike aberrations for number of line scans and number of measurement points per scan

The analysis in this section looks at measurement noise normalized to 1 μrad rms coupling into mid order Zernike aberrations (defined in Table 3.8) for the number of line scans and number of measurement points per scan on a 2 m diameter flat mirror. The line scans are equally spaced in angle (as shown in Figure 2.6) and the measurement points per scan are equally spaced across the diameter of the mirror. The proceeding plots shown are for the case of three line scans separated by 120° going through the center of the mirror. More plots are available in the appendix for line scans that are offset from the center of the mirror.

Summary of the proceeding plots (Figures 18 through 20):

1. The analysis assumes measurement noise normalized to 1 μrad rms coupling into mid order Zernike aberrations for a 2 m flat.
2. The sensitivity to trefoil requires four line scans, and the sensitivity to pentafoil (4θ) requires five line scans. The proceeding plots are for the case of three line scans only, so trefoil and pentafoil are omitted. The results for more lines scans are provided in the appendix.
3. The effect of increasing the number of measurement points generally reduces the measurement coupling into mid order Zernike aberrations by AN^{-m}, where A would be the sensitivity to noise and a constant, N is the number of measurement points, and m is the power with an ideal value of 0.5.
4. The plots were fitted with the function $AN^{-0.5}$. The coefficient A was chosen that allowed a best fit to the distribution of data points. The distribution of the data for each number of measurement points comes from varying the sampling spacing. For small N, the plots deviated from the fitting function due to under sampling of the aberration. The points where the deviations occur are labeled $N_{\min}$, a transition point for under sampling to full sampling.

TABLE 3.9. Table of the values of the sensitivity to noise, *A*, and number of minimum measurement points required for full sampling of mid order Zernike aberrations.

	Mid order Zernike aberrations							
	Z12	Z13	Z14	Z15	Z16	Z17	Z18	Z25
$N_{\min}$	< 5	< 5	11	11	8	--	--	8
A	115	115	40	40	35	--	--	25

Scaling law example

The values of the coefficient *A* shown in Table 3.9 are for a 2 m flat with noise normalized to 1 μrad rms. The values can be scaled to any size mirror assuming the measurement noise is known by the following scaling law:

$$\varepsilon = \tfrac{1}{2} D(\mathrm{m}) \times \Delta\theta(\mu\mathrm{rad}) \times A N^{-1/2} \tag{3.6}$$

For example, the sensitivities of the mid order Zernike aberrations can be scaled for the 1.6 m flat with 0.3 μrad rms. Using the scaling law, we can estimate the values of the *A* coefficient as shown in Table 3.10.

TABLE 3.10. Values of the sensitivity to noise coefficient using the scaling law. The new values are for the 1.6 m flat with 0.3 μrad rms measurement noise.

	Mid order Zernike aberrations							
	Z12	Z13	Z14	Z15	Z16	Z17	Z18	Z25
A	17.3	17.3	6	6	5.3	--	--	3.8

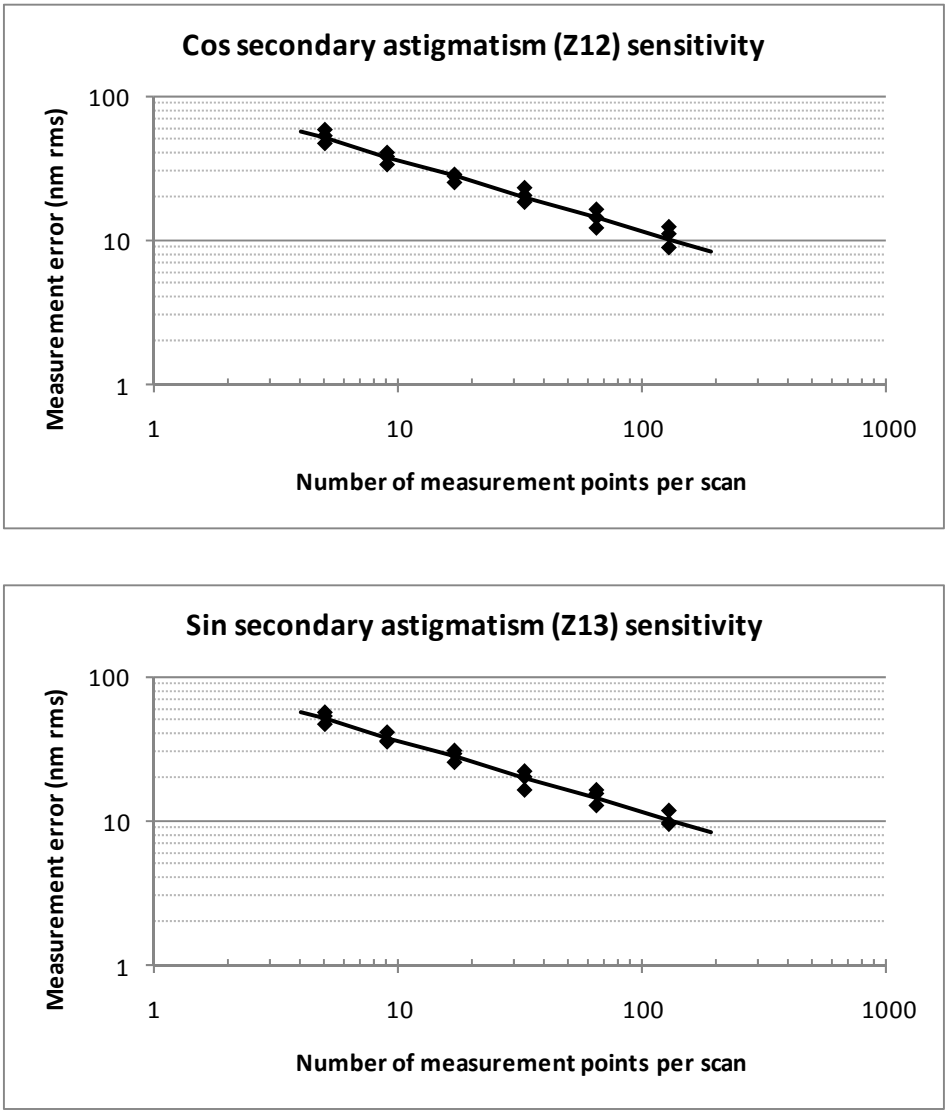

FIGURE 3.18. Measurement noise normalized to 1 μrad rms coupling into secondary astigmatism (Z12, Z13) for number of line scans and number of measurement points over a 2 m flat. A = 115 for both components of astigmatism.

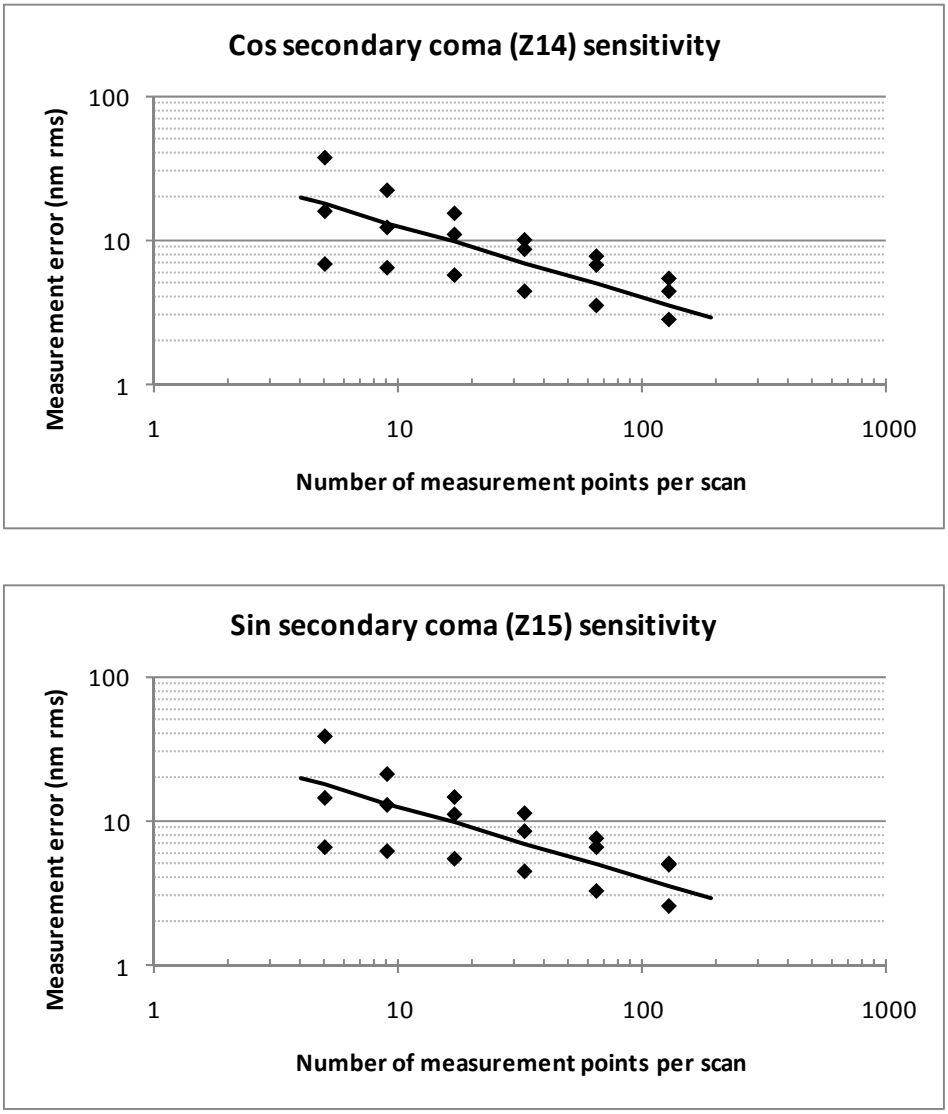

FIGURE 3.19. Measurement noise normalized to 1 μrad rms coupling into secondary coma (Z14, Z15) for number of line scans and number of measurement points over a 2 m flat. $A = 40$ for both components of coma.

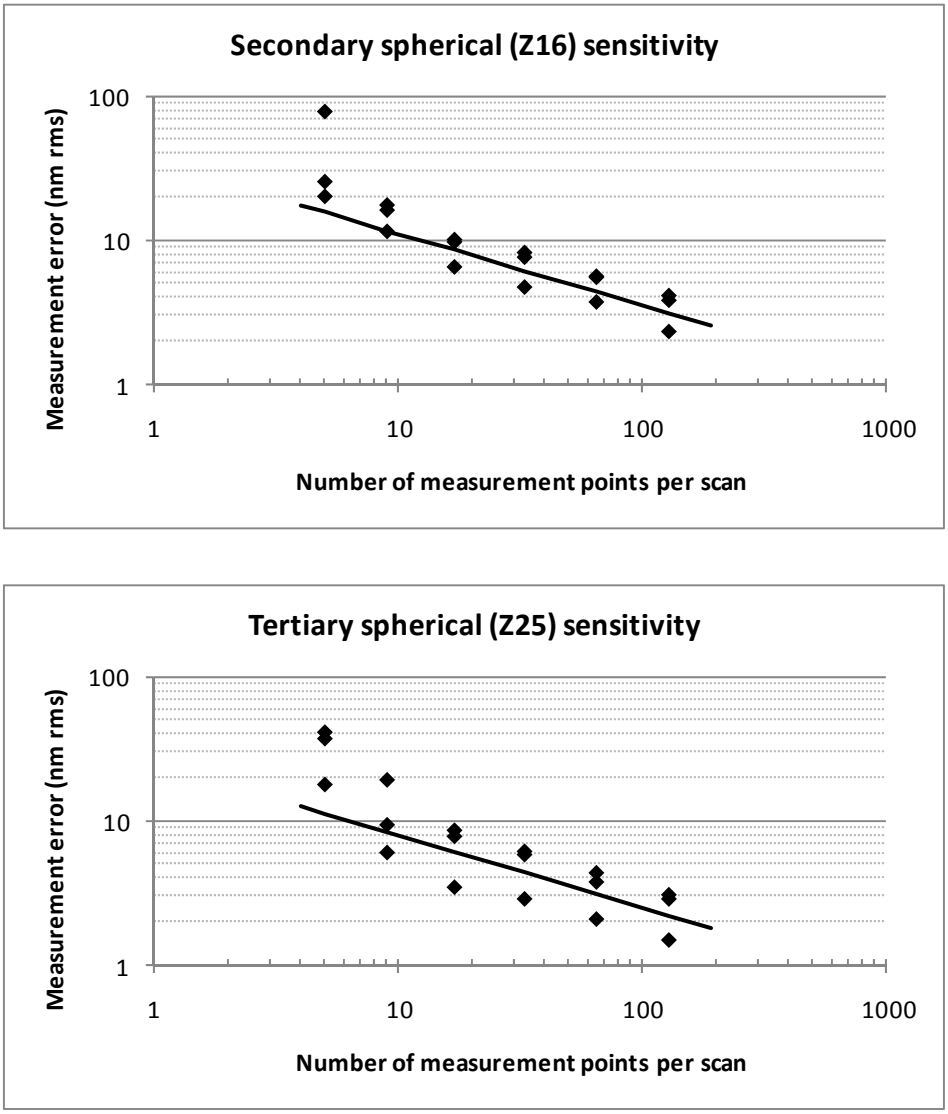

FIGURE 3.20. Measurement noise normalized to 1 μrad rms coupling into secondary and tertiary spherical (Z16, Z25) for number of line scans and number of measurement points over a 2 m flat. A = 35 and 25 for secondary and tertiary spherical, respectively.

3.4.11. Effect of sampling spacing and noise on measurement error

The measurement sampling arrangement and noise affects the measurement uncertainty, especially for higher order Zernike aberrations. The previous set of plots showed a distribution of data points for each number of measurement points per scan. This can be explained by varying the sampling spacing. In Figure 3.21 we show two different sampling arrangements for five measurement points across the mirror and a fit to the point using the slope function for secondary spherical. The five measurement points, showing some noise variation, in both cases are distributed evenly across the mirror (the plot is normalized in radius). In one case (square markers) the edges of the mirror are sampled. In the other case (triangle markers) the edges are not sampled, but the sample spacing is smaller.

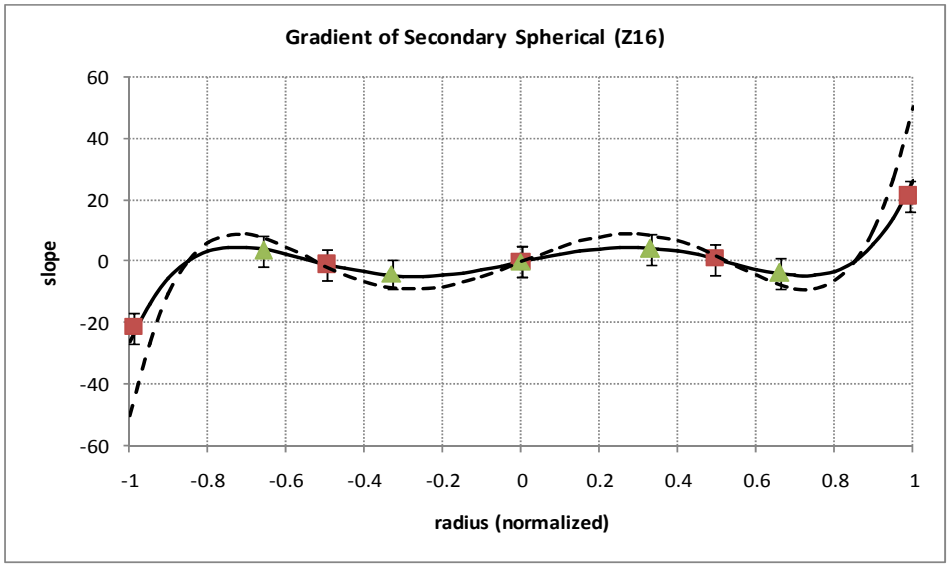

FIGURE 3.21. Sampling for secondary spherical aberration (Z16) with two different five equally spaced sample points (sample points are showing noise variation).

In the case of sampling at the edges the measurement error is better controlled, because the edge points alone limit the amount of variation in the fit. For the other case there is no constraint at the edges, so the measurement error is not well controlled and has more variation. The latter case then is not a recommended sampling arrangement due to larger measurement error, especially for higher order Zernike aberrations.

3.4.12. Limitation of the Zernike basis set

The fits to the slope data were performed using a Zernike basis. The results of the Monte Carlo analysis and the example given in Section 3.4.11 showed the polynomials with this basis seemed to become unbalanced in slope space, because in slope space the gradients of the Zernike polynomials were used for the least squares fitting. More weight is given to the higher polynomial orders; therefore, behavior at the edges varies more rapidly than around the center of the mirror. Perhaps it would be better to develop and use another orthogonal basis set of polynomials that is more balanced in slope space to perform the least squares fitting. After the surface has been reconstructed with the new orthogonal polynomials, the surface can then be related back to Zernike polynomials.

3.5. Conclusion and Future Work

We provided an analysis of the scanning pentaprism system that measured flatness in large flat mirrors with an option to measure other low to mid order aberrations and only θ dependent aberrations. The system alignment was discussed in detail. The measurement accuracy was limited by second order influences from misalignments and autocollimator, pentaprism, and test surface motions, which were minimized through careful system

alignment and active pentaprism motion control. A Monte Carlo simulation of the system performance was performed based on the measurement uncertainty estimated from the error analysis. The simulation result showed the uncertainty in the measured low order Zernike aberrations and measurements to about 15 nm rms of low-order aberrations are achievable for 2 m class flat mirrors. Additional Monte Carlo analysis was performed that studied the effect of measurement noise coupling into mid order Zernike aberrations for the number of line scans and number of measurement points per scan over a 2 m flat mirror.

The high accuracy of the test system makes it ideal for absolute testing of arbitrarily large flat mirrors. This test can be used as a final test on the surface figure or to guide polishing during fabrication. The kinematic base allows the test system to be moved to the polishing table without moving the test flat to a testing fixture and stowed when not in use or during polishing.

The results were obtained using the Zernike basis for polynomials. These polynomials seemed to become unbalanced in slope space. A different orthogonal basis set of polynomials might work better for the least squares fitting in slope space. This investigation is left open for future work.

Absolute calibration of the system was not performed. This can be accomplished using liquid reference surfaces over very long test paths (~4 m), where the liquid surfaces are only limited by the curvature of the earth (sag/power = 0.31 μm peak to valley over 4 m). The result will be excellent characterization of the system performance. This task was left open for future work.

CHAPTER 4

DEVELOPMENT OF A 1 METER VIBRATION INSENSITIVE FIZEAU INTERFEROMETER

We developed a 1 meter aperture vibration insensitive Fizeau interferometer to test 2 m and larger flat mirrors through subaperture sampling. The subaperture measurements can then be combined by stitching to obtain a full surface map. The 1 m interferometer was constructed using a 10 cm aperture commercial instantaneous Fizeau interferometer combined with custom 1 m reference and collimating optics. Multiple surface measurements made by rotating the reference flat and a 1.6 m test flat and post processing of the subaperture measurements allowed for absolute characterization of the two surfaces to 3 nm rms in surface irregularity. In this chapter, we describe the system design, calibration of the reference flat, and data analysis including the correction for field errors and mapping distortion.

4.1. Introduction

At the University of Arizona Optical Engineering and Fabrication Facility (UA-OEFF), we have implemented precise and controllable polishing techniques for manufacturing large flat mirrors (> 1 m) [49]. However, metrology has been a major obstacle for testing large mirrors accurately and efficiently. The two main problems are: 1) limited aperture

sizes of commercial interferometers, and 2) stitching is required but limits the measurement accuracy and efficiency.

To enable surface testing of 2 m class and larger flat mirrors, we scaled up a 10 cm aperture instantaneous Fizeau interferometer to 1 m and performed subaperture testing. We accomplished this by expanding the 10 cm beam to 1 m and inserting a 1 m custom reference flat. The collimating optics were arranged such that the test was performed vertically. The reference flat was held in a kinematic mount. The mount has a three point base for mechanical stability and placement repeatability, and allowed six equally spaced rotations of the reference flat. After multiple measurements and measurement redundancy through rotations of the reference and the test flats, the nonsymmetrical surface errors in the reference flat can be isolated from the test surface. Power in the reference flat was calibrated using an auxiliary test system that measured surface slopes very accurately [50]. The reference flat surface errors were then stored in a reference data file, which was used to correct each of the subaperture measurements before combining them.

4.1.1. Testing large flat mirrors

The most efficient and accurate method of measuring flat surfaces uses a Fizeau interferometer with a flat reference surface. Most commercially available interferometers are limited to 10 to 15 cm apertures, although 30 cm [51-52] and 60 cm [53] aperture interferometers have been demonstrated. Large flat surfaces can be measured with small aperture interferometers, but stitching subaperture data is required [17-20]. As the

subaperture becomes smaller compared to the size of the test mirror, the accuracy and efficiency of the measurement diminishes.

Due to size limitations of commercial interferometers for direct measurements, large flat mirrors are normally tested in a Ritchey-Common configuration [16, 21]. The Ritchey-Common test, however, is limited in other areas as discussed in Chapter one.

In order to guide our polishing of high quality flat mirrors, the surface measurements must be efficient to perform and provide accuracy of a few nanometers. It is optimal to measure flat mirrors *in situ* as they rest on our 4 m polishing table, which allows rapid turnaround between testing and polishing. It is impractical to isolate the system from vibrations, but the test hardware must function in the shop environment, which had considerable vibration and air currents.

The vibration insensitive Fizeau interferometer meets all of our requirements. The 1 m reference surface can be held to a few centimeters above the mirror under test as it rests on the polishing machine. The short air gap and the use of polarization for instantaneous phase shifting give high accuracy in the presence of vibration and thermal effects.

4.1.2. Instantaneous interferometry

Vibration is a major problem in optical testing. Industrial environments, such as optical fabrication and testing facilities, are prone to vibrations and air motions. Vibrations are especially problematic in large scale optical testing where the large optics and the supporting mechanical structures are not easily isolated. In addition, air motions over long test path lengths contribute to the overall fringe motion. In the presence of

vibrations, the standard phase shifting interferometry through temporal phase stepping is inadequate for accurate optical testing. The time scale for mechanical vibrations is shorter than the time between exposures. Thus, vibrations limit the ability to collect accurate data. To overcome these problems, simultaneous acquisition of the phase shifted frames is needed.

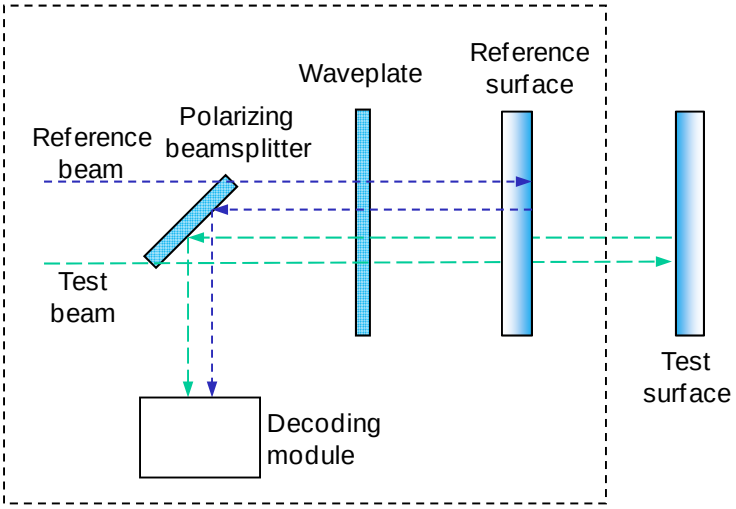

FIGURE 4.1. Schematic showing a Fizeau interferometer simultaneous phase shifting concept using polarizing element and orthogonal polarizations.

We use the Intellium H1000 (made by Engineering Synthesis Design, Inc. [54]) instantaneous Fizeau interferometer. This interferometer uses polarizing elements to produce three simultaneous phase shifted signals for interference. In this method, two orthogonal polarizations, *A* and *B*, are emitted by the interferometer, as shown in Figure 4.1. The polarizations can either be linear or circular. One polarization, *B* for example, is reflected off the reference surface, and the other polarization, *A*, is reflected off the test surface. The return signals are combined to produce a set of interference fringes

simultaneously, which are then recorded by a decoding module. The interference fringes are then combined to generate a phase map of the test surface.

4.2. Design and Analysis of the 1 Meter Fizeau Interferometer

A schematic of the 1 m Fizeau test system is shown in Figure 4.2. The inset photos are the actual components of the ones shown schematically. The Intellium H1000 interferometer used a 30 mW laser diode at 657 nm as a source. The source emitted two circularly polarized beams, as opposed to linearly polarized, to minimize birefringence though the 1 m reference flat [55]. A standard reference diverger and the off axis parabola (OAP) formed the beam expansion and collimation. The 1 m reference flat was suspended over the large test surface (described in section 4.3.1).

4.2.1. Test concept

Fizeau interferometers require a collimated beam and a flat reference surface to test other flat surfaces [15-16]. The Intellium H1000 emitted a 10 cm collimated beam. The reference diverger and the OAP expanded the beam to 1 m. A 15 cm fold flat kept the H1000 horizontally mounted and allowed the test to be done vertically.

In this arrangement of the interferometer, the probe beam was external to the Intellium H1000 interferometer, hence the external reference surface. Interference occurred between the reference flat bottom surface and test flat top surface. A small wedge in the reference flat isolated the reflection off the top surface of the reference flat from the measurements. The air gap between the reference and test surfaces was kept to a few centimeters to minimize the errors from illumination. The 1 m beam then

subsampled the larger flat mirror under test. Rotating the large flat mirror underneath the reference flat allowed for complete coverage of the flat mirror. The subaperture measurements were corrected for errors. The corrected subaperture measurements were then stitched together to obtain a full surface map.

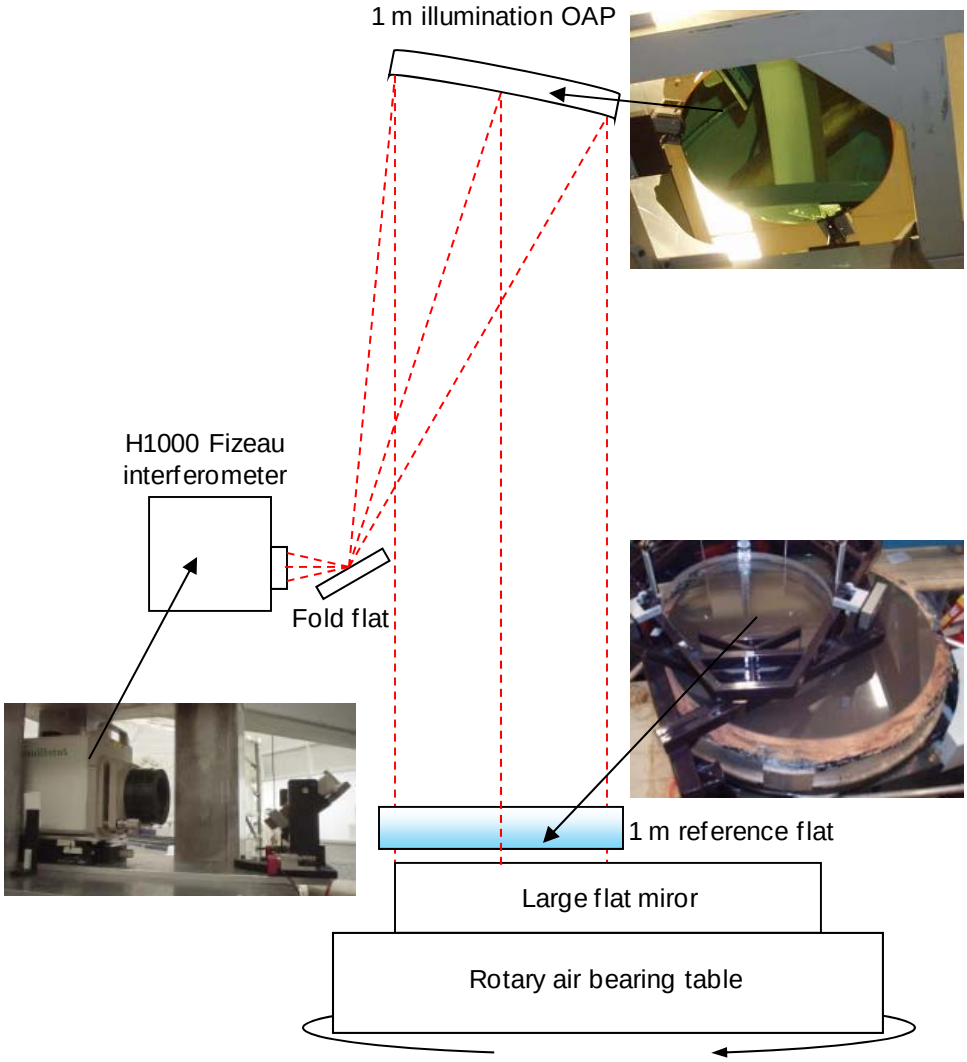

FIGURE 4.2. Schematic of the 1 m Fizeau interferometer with an OAP for beam collimation and an external 1 m reference.

4.2.2. Test tower design

The test components shown in Figure 4.2 were integrated into a large test tower with base dimensions 7.2 m × 3.3 m and height 4.2 m. The test tower was a four column weldment with diagonally braced framework as shown in Figure 4.3. The columns were made out of 12 mm thick 20 cm square metal tubes. The Intellium H1000 interferometer and the fold flat were mounted on a platform. The platform was then suspended from the horizontal cross member in the test tower. The test tower was braced at the top with two additional brace beams, which held the OAP in place. The fully integrated structure is shown in Figure 4.9. The entire structure was then moved over the polishing table. The advantage of doing this was to allow the test flat to remain on the polishing table and perform testing *in situ*. An additional horizontal cross member (not shown in the solid model in Figure 4.3) was used as a place to stow the kinematic reference flat during polishing. The tower was designed to vibrate below 15 Hz to ensure system stability. Table 4.1 shows the three lowest vibration modes of the tower from the finite element analysis (FEA) model.

TABLE 4.1. Fizeau test tower lowest frequency modes.

	Frequency (Hz)	
Mode	**Pinned ends**	**Fixed ends**
1	8.69	10.75
2	12.71	12.87
3	13.00	13.14

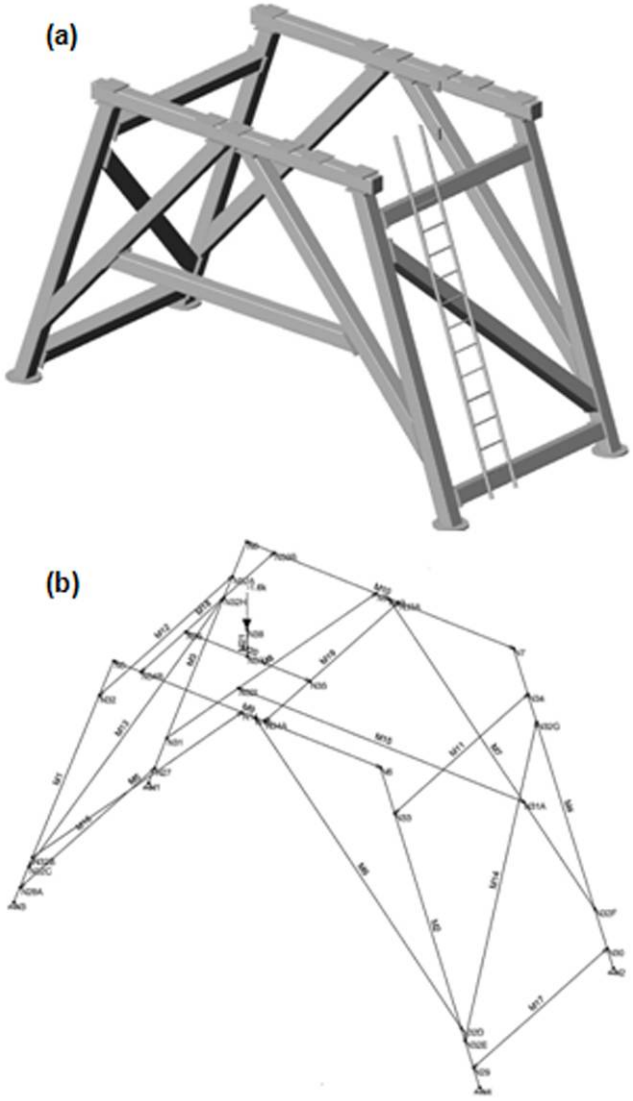

FIGURE 4.3. Solid (a) and FEA dynamic (b) models of the Fizeau test tower.

4.2.3. Collimation OAP design

The OAP was used as the beam collimator. The OAP was mounted in a whiffletree type back support with tangential side supports as shown in Figure 4.4. The OAP was placed in a downward looking orientation, tilted at 5.7° from vertical. The support allowed tip and tilt adjustments for initial alignment and locking of the OAP.

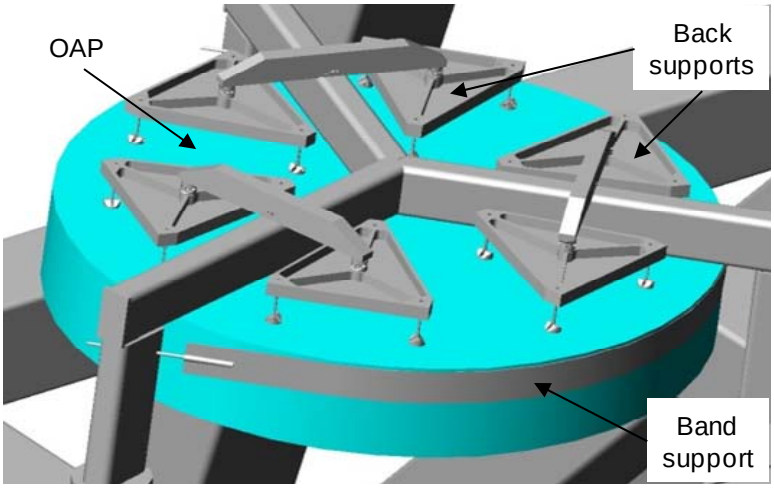

FIGURE 4.4. OAP mounted in an 18 point whiffletree and band support. The mount provided tip and tilt adjustments.

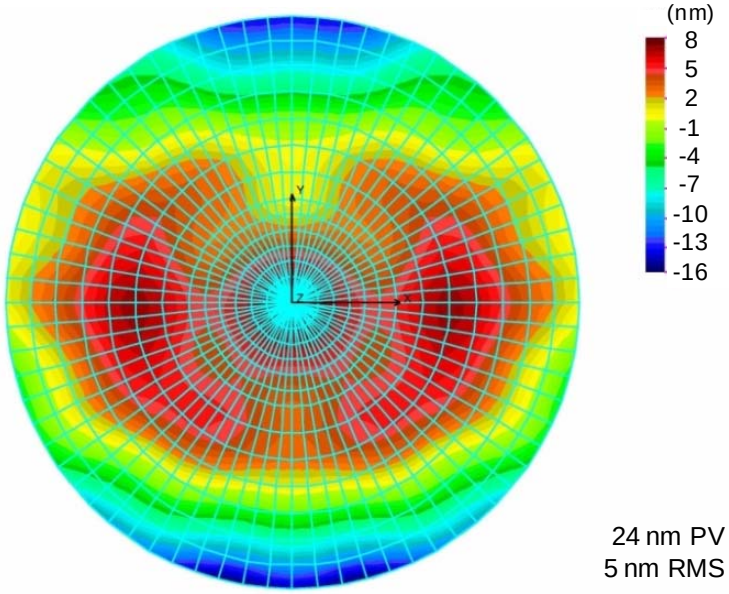

FIGURE 4.5. FEA model of the mounted collimating OAP optical performance (5 nm rms).

Figure 4.5 shows the optical performance of the mounted OAP from the finite element model. A maximum slope error of 0.1 μm/mm due to gravity and mount induced surface deformation was derived from the system error budget. With this requirement, the analysis predicted surface errors of 5 nm rms from gravity and the mount.

4.2.4. Field effect errors

The Intellium H1000 interferometer used two beams with orthogonal polarizations that had a slight shear between them. If polarization *A* was used as the reference beam, then polarization *B* must be the test beam for interference and phase shifting to occur. The slight shear between the beams and using the OAP for beam collimation caused the beams to traverse slightly different paths through the system. This effect of traversing different path lengths caused field, or retrace, errors in the measurements [55]. To fix this problem, measurements were taken with both polarizations as the reference beam and the results were averaged to obtain a phase map that was free of field errors. Using polarization *B* as a reference beam, however, resulted in inverted surface maps. This inversion was verified with a simple but unambiguous test of introducing small tilts in known directions and acquiring the surface data. The surface maps were re-inverted before combining them with the measurements taken with polarization *A* as the reference beam.

Figure 4.6 shows using both polarizations as reference beams to take surface measurements and the average of the two measurements to eliminate the field errors. This fix must be applied to each subaperture measurement before further data processing.

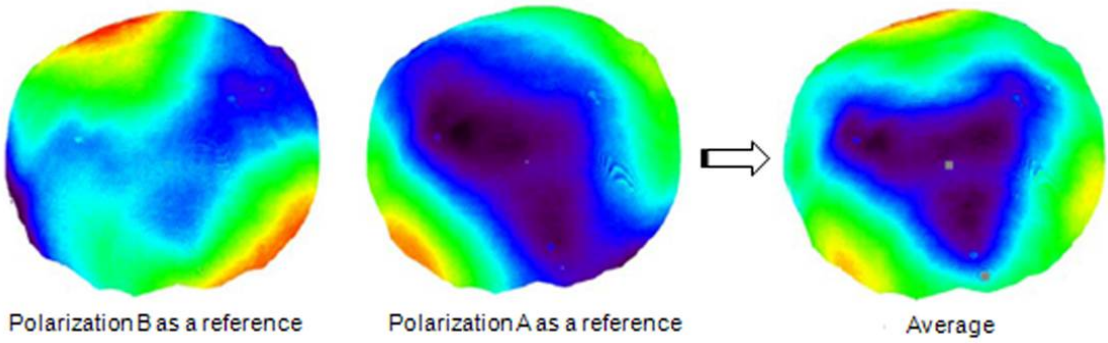

FIGURE 4.6. The 1 m Fizeau interferometer with polarization *B* as the reference beam (left), polarization *A* as the reference beam (center), and the average of the two measurements (right) to eliminate field errors.

The average surface map in Figure 4.6 exhibits trefoil, which is a result of the three cable suspension of the reference flat (see Figure 4.7).

4.2.5. Wedge in test plate

There was a small wedge in the reference flat. The wedge allowed the reflection from the back (top) surface of the reference flat to be isolated from the measurements. The wedge, however, caused the beam spots from the *A* and *B* polarizations to be rotated and translated at the image plane when the reference flat was rotated. Because of this, the spots were tracked carefully to prevent errors in the measurements.

4.2.6. Distortion correction

Using the OAP to collimate the beam caused slight mapping errors. Mapping errors, also known as distortion, occur when points on an object do not maintain their relative spacing in the image plane. Distortion in each of the subaperture measurements must be

fixed before combining them to generate a full surface map. We developed a four-step process to correct for distortion in each of the subaperture measurements.

1. First, we defined and fabricated a Mylar based film fiducial mask. A fiducial mask contains a regular pattern of small circular apertures or fiducials. The mask is usually placed at the test surface and that typically cover 5 to 10 pixels for easy locating in the image plane. The physical spacing of the small apertures must be known. Our mask contained 12 mm circular apertures spaced 10 cm apart.
2. Next, we imaged the fiducial mask through the system. This was accomplished by placing the mask at the pupil, or the reference surface, and performing the normal data acquisition.
3. Then, we defined fitting polynomials and determined their coefficients. This was accomplished by relating the undistorted points in object space to the distorted digitized points in image space through polynomials of degree *n*.
4. Finally, we filtered the distorted image through the fitting functions to generate an image that was corrected for distortion.

The fitting polynomials were defined as

$$\begin{aligned} x &= \sum u_{ij} X^i Y^j \\ y &= \sum v_{ij} X^i Y^j \end{aligned} \tag{4.1}$$

where x and y are the original image coordinates

X and Y are similar object coordinates

u_{ij} and v_{ij} are coefficients to be determined through least squares fitting.

The degree of the polynomials, $n = (i + j)$, determines the minimum number of fiducial points required by the following formula,

$$N \geq \frac{n(n+3)}{2} + 1. \tag{4.2}$$

For example, a fitting polynomial of degree three requires a minimum of 10 fiducial points for correct determination of the coefficients

During testing we controlled the mapping to 2 mm, which coupled in as surface error of about 1 nm rms.

4.3. System Integration

4.3.1. Reference flat and its mounting support

The reference flat was a 1 m transmissive fused silica polished to 100 nm peak to valley. It was 11 cm thick and weighed about 195 kg. A mechanically stable kinematic mount was designed to hold the reference flat, as shown in Figure 4.7. Three counter balanced cables were attached to pucks carefully bonded to the top surface of the reference flat. In addition, six tangential edge supports were added. The cables and the edge supports offloaded about 60% of the reference flat weight (117 kg). As stated earlier, the three cable suspension caused trefoil in the reference flat surface.

The kinematic base rested on three stable points. The three points were equally spaced which allowed for three equally spaced rotations. Separately, a smaller top support structure also rested on three points, which were offset by 60° from the base points and allowed for three additional equally spaced rotations. Combined, the entire

support structure provided six equally spaced rotations and good position repeatability of the reference flat.

The control of the gap between the reference and the test surfaces is important. As the gap increases the accuracy of the test system degrades. For example, the test flat may be assessed to an accuracy of 20 nm peak to valley. The illumination error was expected to be less than 0.5 mrad. For this case, the gap between the reference and test surfaces must be maintained to

$$t \le \frac{\lambda}{100}\frac{1}{\theta^2} \approx 8 \text{ cm}. \tag{4.3}$$

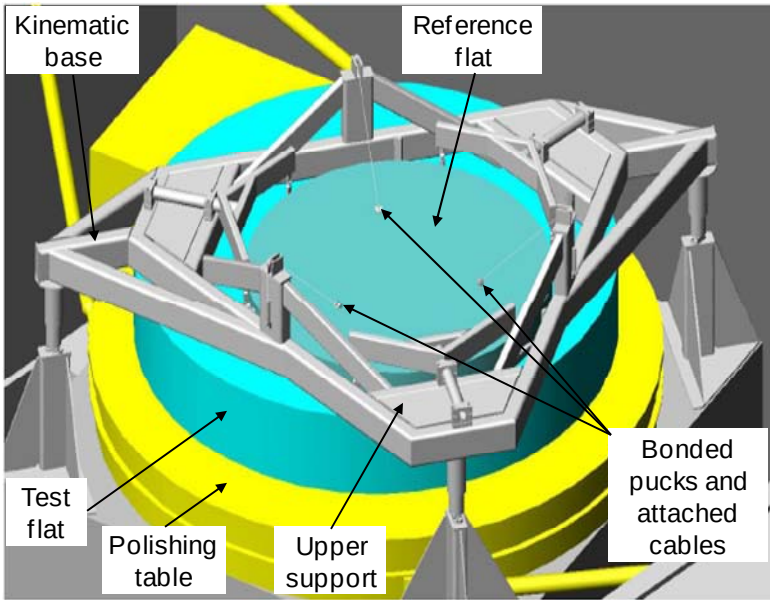

FIGURE 4.7. Oblique top view of the kinematic support mount for the Fizeau reference flat. Cables, attached to the pucks, and a six point edge supports held the reference flat.

4.3.2. System alignment

To enable system alignment, each of the components in the test system required multiple degrees of freedom with coarse and fine adjustments. The OAP mount provided adjustments in tip and tilt. The reference flat mount provided coarse and fine adjustments in tip and tilt. The fine adjustment was accomplished through three voltage driven piezo transducer (PZT) stacks. The Intellium H1000 interferometer with the diverger and fold flat was mounted on a stage with five degrees of freedom combining coarse and fine adjustments. The system was first aligned as an autocollimation of the OAP with the reference flat as the return flat. In this configuration, the diverger surface was the reference surface and OAP surface was the test surface. During initial alignment, a pan of oil was used as the return reference surface due to its natural alignment to gravity.

In the autocollimation test configuration, the OAP position was no longer in the common path of the reference and the test beams, thus the OAP required adjustments to get a minimum wavefront slope in the interference pattern. Most of the alignment error introduced astigmatism. A combination of the OAP, H1000 interferometer and fold flat iterative adjustments minimized the wavefront slope. The alignment of these components was not critical, because all the surfaces before the reference surface are common path in the Fizeau test. However, careful alignment was still performed to minimize any high order effects. After the system alignment, we required the reference flat to be stable to 3 nm rms during testing.

To better understand the effects of OAP motion on the system alignment, the test system was modeled as an autocollimation test using optical design software.

Perturbations in *x* and *y* tilts and clocking about *z* were applied to the OAP in the model. Figure 4.8 shows the effects of the perturbations on alignment of the system. The simulation was used to aid in fine tuning the alignment of the system.

The model showed OAP tilt about the *y*-axis and clocking about the *z*-axis gave the same alignment errors, but the wavefront error was more sensitive to tilt about the *y*-axis.

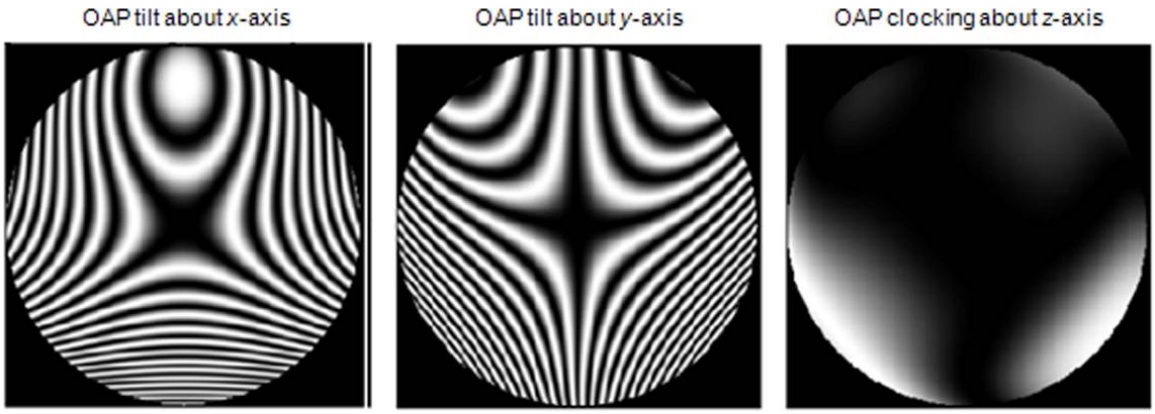

FIGURE 4.8. Sensitivity to the OAP motion - after addition of 0.5 mrad of tilt about *x* (left) and *y* (center), and clocking about the *z*-axis (right) to the OAP in an autocollimation test configuration.

4.4. System Calibration

The conventional method of absolute calibration of flat surfaces involves comparison between three flat surfaces, commonly known as the three flat test [15, 56]. In our case, this approach is not possible because we had only one 1 m flat. In this section we present an alternative approach to reference flat calibration.

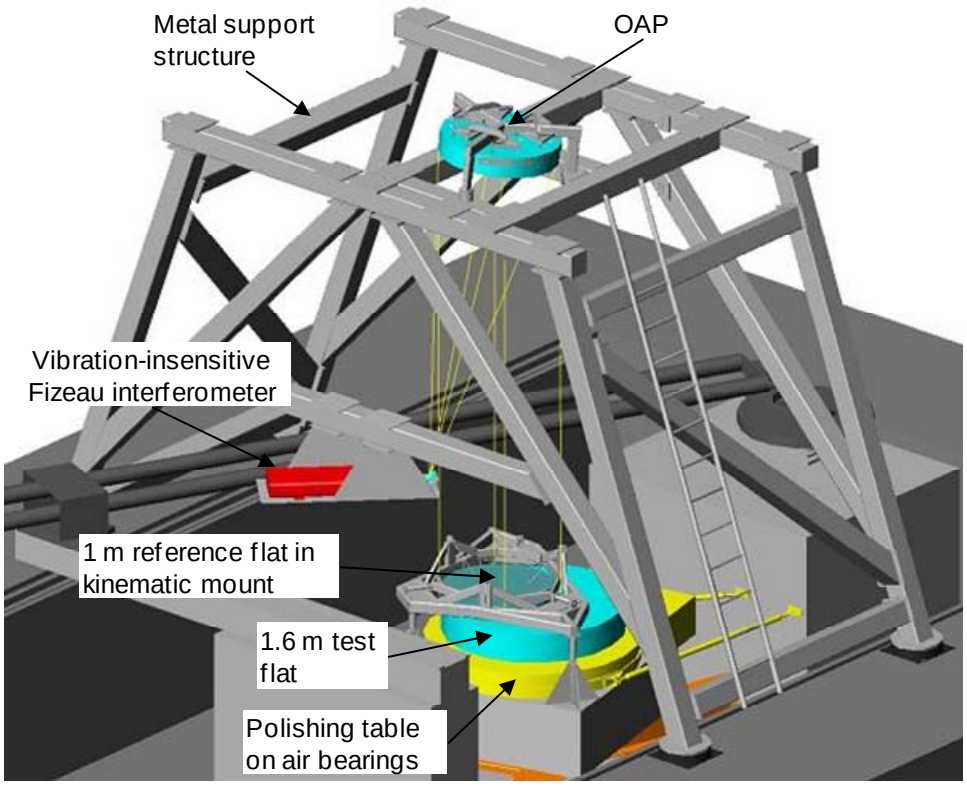

FIGURE 4.9. Solid model of the 1 m vibration insensitive Fizeau test system fully integrated and aligned.

4.4.1. Calibration of reference surface irregularity

By using overlapping subapertures along with multiple rotations of the reference and test flats, we can obtain unbiased estimates of both the reference and the test surfaces [57-58]. The measurement algorithm that was used to obtain 24 subaperture measurements is provided in Table 4.2. This procedure, shown schematically in Figure 4.10, helped in separating the errors in the reference and test surfaces. Surface errors that moved with the reference flat belonged to the reference flat; the remaining errors were associated with the test flat. This method of rotating surfaces with no translations, however, was immune

to symmetrical errors in the reference flat, thus power in the surface measurements were be ambiguous. We addressed this problem by using an auxiliary test system that measured power and other low order aberrations in the test surface (discussed in section 4.5.3).

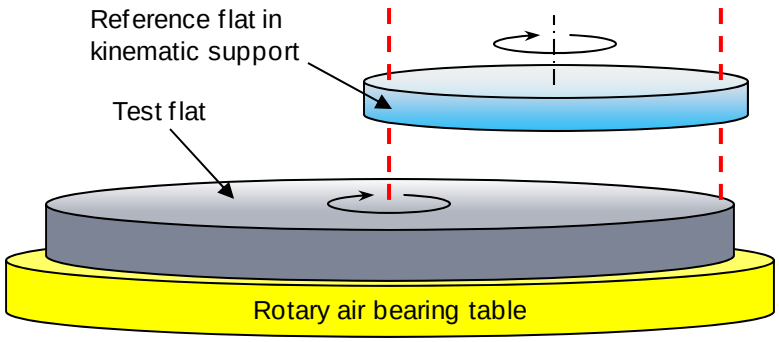

FIGURE 4.10. Schematic for method of estimating the reference flat by rotating the reference and test flats.

TABLE 4.2. Measurement algorithm for obtaining the unbiased estimates of the reference and test surfaces.

Reference flat angle position (deg)	Test flat angle position (deg)				Number of measurements
0	0	90	180	270	4
60	15	105	195	285	4
120	30	120	210	300	4
180	45	135	225	315	4
240	60	150	240	330	4
300	75	165	255	345	4
			Total number of measurements		24

An algorithm was developed that combined all the measurement data and separated the surface errors in the reference and test surfaces using maximum likelihood estimation [57-58]. Figure 4.11 shows the reference surface estimated after acquiring 24 subaperture measurements using the algorithm given in Table 4.2 and applying the maximum likelihood estimation to separate the errors in the reference flat from the errors in the test flat.

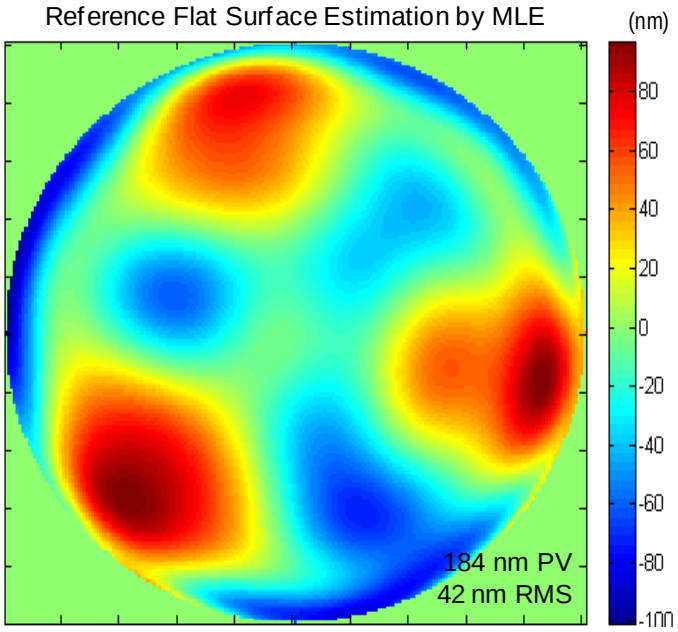

FIGURE 4.11. The 1 m reference surface estimated by modulation of the reference and test surfaces and performing maximum likelihood estimation. Multiple Zernikes terms were used to generate the surface (42 nm rms). The surface map shows the effect of the three point cable suspension.

The surface map shows 42 nm rms after removing ambiguous rotationally symmetric errors. The surface map reveals the effect of the cable suspension as trefoil. The positions of the three pucks bonded to the top surface are indicated by the three high

spots on the surface map. This surface map was saved as a reference data file. The file was then be subtracted from each of the subaperture measurements before they are combined. The error in the surface irregularity calibration was estimated to be 1 nm rms [58].

4.4.2. Comparison to finite element analysis model

A simulation of optical performance was also performed on the finite element model of the suspended reference flat. The simulation used the following parameters listed in Table 4.3 for the mount shown in Figure 4.7.

TABLE. 4.3. The reference flat support parameters for the FEA model and simulation.

Six point edge whiffletree support	Top surface cable support
• 60° puck spacing • Pucks positioned at center of gravity plane of the reference flat	• Three pucks bonded to the top surface positioned at 28 cm from center (56% ϕ) • 120° puck spacing • 45° load wire angle

The result of the simulation is shown in Figure 4.12. The simulation output gave 29 nm rms, which is conservative compared to the result from the previous method described above. The result from the simulation did not include errors such as interferometer noise and illumination and alignment errors. Also the systematic errors were not measured, and therefore were not included in the simulation. They were, however, automatically included in the measured data, thus giving a higher rms surface error for the reference flat shown in Figure 4.11.

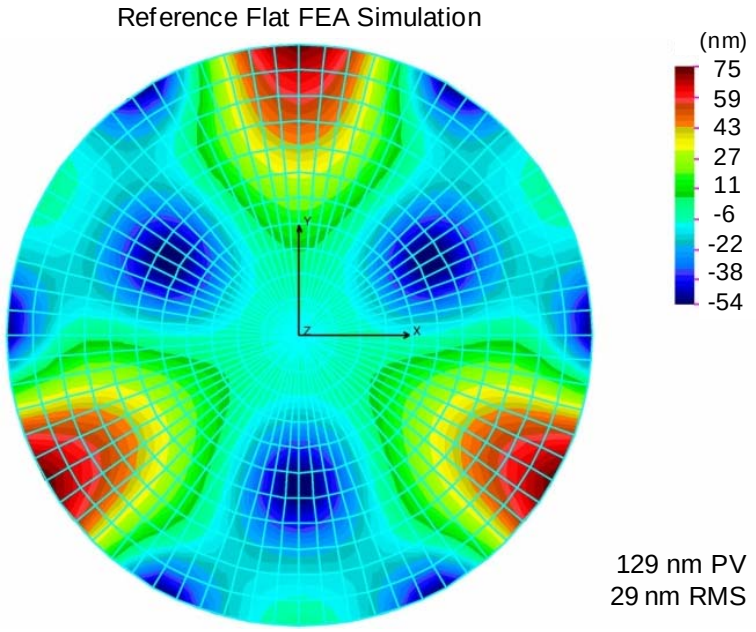

FIGURE 4.12. Results of the FEA simulation on the mounted reference flat that shows the effects of the three cables suspension and edge supports.

4.4.3. Calibration of reference surface power

Power in the reference surface can come from two things: 1) power left in the surface during polishing, and 2) power due to sag from gravity. Doing the multiple rotations of the reference and test surfaces to obtain overlapping subapertures did not calibrate power in the reference surface. An additional degree of freedom in translation of the reference flat was needed to calibrate the symmetrical errors in the reference surface. This additional degree of freedom was not available to us. Thus, power in the subaperture measurements was ambiguous.

One method of measuring the reference surface power is to look at the cosine effect at the reference surface [59]. With careful measurements of the slope errors and the gap between the reference and test surfaces, we could quantify this effect, although

with some difficulty. Instead, we used an existing auxiliary test system to calibrate power in the reference surface. We developed a highly accurate slope test that measured power and other low order surface errors in the large flat [50]. The power measured with the slope test was then used to calibrate the power in the reference surface. With this method the power ambiguity was removed.

4.5. Error Analysis

4.5.1. Test error budget from combined error sources

Table 4.4 shows the contribution from all error sources and the total combined error from the test. The combined errors set the error budget for the test. Since the power calibration was performed with an auxiliary test system, this calibration was not included in the error budget for the 1 m Fizeau test.

TABLE 4.4. Combined error sources and the error budget for the subaperture test.

Error source	Value (nm rms)
Interferometer noise	3
Illumination/alignment	3
Distortion (mapping)	1
Calibration	1
Combining the subapertures	1
Root sum square	4.6

4.6. Measurements on a 1.6 Meter Flat Mirror

Su [57-58] showed that the separation of the reference surface and test surface errors can be accomplished to 3 nm rms using the maximum likelihood estimation method through the repeatability of the subaperture measurements.

4.7. Conclusion

The developed 1 m vibration insensitive Fizeau interferometer has made accurate and efficient testing of 2 m class and larger flat mirrors possible. The increased size in aperture provided more surface coverage, thus less subaperture data to get full surface coverage lead to less errors from stitching. Through overlapping subaperture measurements and multiple rotations of the reference and test flats, errors from both surfaces can be isolated by maximum likelihood estimation. An auxiliary test was used to calibrate power in the reference flat. A reference data file containing errors from the reference flat was generated and stored. This file was then subtracted from each subaperture measurement before combining them. The results from the maximum likelihood estimation showed that a 2 m mirror can be measured and the reference flat calibrated to 3 nm rms. This Fizeau is an *in situ* test and can be used as a final test on the surface figure or to guide polishing and figuring during fabrication. The kinematic mount allows the reference flat to be moved and stowed during polishing.

SECTION II

ADVANCED FABRICATION TECHNOLOGIES

This second section contains a chapter on the methodology for manufacturing high performance large flat mirrors with greater emphasis on the fabrication techniques that we implemented. We found classical fabrication methods alone do not enable the manufacture of quality large flat mirrors, because the classical methods are not scalable. We introduced computer controlled polishing that used simulation software combined with accurate and efficient metrology to achieve rapid convergence of polishing and produce the best 1.6 meter flat mirror in the world (11 nm rms power and 6 nm rms surface irregularity). This methodology used to produce the 1.6 meter flat can be extended to 4 meters or larger flat mirrors, a key advantage over classical fabrication methods.

CHAPTER 5

METHODOLOGY FOR FABRICATING AND TESTING LARGE HIGH PERFORMANCE FLAT MIRRORS

In this chapter we present on the methodology and enabling technologies for fabricating and testing high performance flat mirrors larger than 1 meter in diameter. Classical fabrication methods are combined with predictive software to allow rapid convergence of polishing and accurate slope and interferometric testing to guide the polishing and figuring of a 1.6 m flat mirror. The developed technologies are scalable to larger flat mirrors (≥ 4 meter diameter). We look at the limitations and risks of extending the technologies to 4 m mirrors.

5.1. Introduction

Large flat mirror fabrication poses significant challenges. The requirement on the radius of the mirror is at the same level as the requirement on surface irregularity (i.e. a few tens of nanometers). Current fabrication and testing technologies, although well established for moderately sized optics (≤ 1 m), do not enable the manufacture of high performance flat mirrors much larger than 1 m. The standard method of characterizing flat surfaces uses Fizeau interferometers that require comparison to a reference surface of similar size, but the development of such interferometers with meter type apertures would be very

expensive to produce. In addition, because large mirrors take months or even years to make, manufacturing becomes very costly.

The current state of the art for flat mirror fabrication uses continuous polishing as discussed in Chapter one. The advantages of using continuous polishing machines are they can produce multiple flat mirrors simultaneously, making this type of a machine very cost-effective, and they can polish smoothly out to the mirror edges. The disadvantage, however, is that mirrors can be no larger than about a third of the diameter of the lap. The largest continuous polishing machines known to exist have laps that are 4 m in diameter. These machines can make up to 1.3 m diameter flat mirrors.

Large flat mirrors are typically tested interferometrically. The three tests that can measure flat surfaces are the Fizeau, Ritchey-Common, and skip flat tests. These tests were discussed in Chapter one. Each has advantages and disadvantages. Their disadvantages affect test efficiency and accuracy that is required in large flat mirror manufacturing.

We provide a brief introduction on the current fabrication technologies for manufacturing large high quality mirrors in Section 5.2. The testing technologies are discussed again, but briefly, in Section 5.3 to make this chapter complete. They are described in more detail in Chapters two through four. Section 5.4 describes the manufacture and testing of a 1.6 m flat mirror and provides results on the finished mirror. Section 5.5 covers the feasibility of extending the fabrication and testing technologies that we developed to 4 m flat mirrors. The concluding remarks are provided in section 5.6.

5.2. Fabrication Technologies

Mirror fabrication techniques include a vast array of polishing methods from the tried and true conventional or classical polishing methods to the modern computer controlled polishing used to make optical surfaces of varying sizes and shapes. The fabrication of large mirrors, in particular, is a time consuming process. The optician uses multiple machines, polishing tools, material and compounds, and specialized skill. This section is a brief introduction to conventional and computer controlled polishing currently used in industry.

5.2.1. Conventional polishing

Conventional polishing techniques make use of proven and established polishing methods, which have been used for many decades [10-11, 71]. Many polishing machines, tools, and techniques have been developed and refined over the years to increase efficiency and accuracy in shaping glass surfaces. Polishing pads, formed wax, or formed pitch, which make contact with the glass, are typically applied to the tool work surface. Various compounds are used during polishing as abrasives and wet slurry to help remove and smooth the glass surface. Conventional polishing techniques rely on controlling the shape of the polishing lap to adjust the entire surface of an optical element. These techniques can be used to make flat surfaces as well as a variety of other elements.

5.2.2. Computer controlled polishing

In the past few decades, computer controlled polishing has come to the forefront in optical manufacturing as the cost of computer control has come down and the flexibility of the method is realized [10-11, 71]. Glass mechanics and polishing parameters are also now better understood; thus, repeatability and modeling of removal functions can be established. Polishing strokes can be optimized by performing well controlled polishing runs. Modeling and optimizing the polishing strokes allow for accurate prediction of the outcome of a polishing run based on the polishing parameters selected. Important information related to the polishing tool dwell time and polishing hit can be then obtained.

5.3. Testing Technologies

There are many metrology techniques in use for optical surface characterization. We developed three very efficient tests that allowed us to accurately measure and monitor the flat surface during polishing and figuring with a fairly rapid (within a day) turnaround of the data. These test systems combined optical and mechanical methods and were used to guide the fabrication and provide measurements on the finished 1.6 m flat mirror. The three tests are briefly discussed below. A full description of the test systems were given in Chapters two through four.

The ability to measure slopes on an optical surface provides an alternative to interferometric testing. Integrating the slope data gives low order surface profiles. Below are brief descriptions of the two test systems used to measure surface slopes

5.3.1. Surface measurement using electronic levels

Using differential electronic levels is a new way of measuring flat optical surfaces [46]. The test is mechanical (contact), instead of optical (non-contact), and measures low order aberrations (e.g. power and astigmatism). We used electronic levels during grinding and coarse polishing to guide the early fabrication of the 1.6 m flat. This method of testing provided an efficient and cost effective way to measure the mirror surface to an accuracy of about 50 nm rms.

5.3.2. Scanning Pentaprism Testing

The scanning pentaprism system, which used two pentaprisms aligned to a high resolution electronic autocollimator, provided a more accurate optical slope test that operated on the same principles as the electronic levels [50]. The scanning pentaprism was used during the late polishing and figuring stages of the 1.6 m flat to monitor the surface and guide the remaining fabrication. It was also used as an absolute test for power on the finished mirror. This testing technique provided an accuracy of about 9 nm rms for power.

5.3.3. Vibration Insensitive Fizeau Testing

We developed a custom 1 m vibration insensitive Fizeau interferometer to monitor the higher order variations in the mirror surface and also guide the remaining fabrication [47]. This test system used a 1 m beam combined with multiple overlapped subsampling to provide a complete coverage of the 1.6 m flat. Stitching and maximum likelihood estimation were used to combine the subaperture measurements and obtain a full surface

map. This measurement method also provided an absolute test on the final surface irregularity to an accuracy of 3 nm rms.

Both the scanning pentaprism system and the 1 m Fizeau reference were designed for kinematic positioning over the flat mirror during fabrication. The kinematic design allowed the flat mirror to remain fixed on the polishing table while the test systems were interchanged for complete surface testing.

5.4. Manufacture and Testing of a 1.6 Meter Flat Mirror

5.4.1. Introduction

The manufacture of large (> 1 m) high performance flat mirrors presents challenges because of the lack of enabling fabrication and testing technologies that economically provide measurement efficiency and accuracy. In this section, we describe the development of novel fabrication techniques that enabled us to manufacture a high performance 1.6 m flat mirror. The testing technologies described in Section 5.3 were used to guide the fabrication.

An important consideration for large mirrors is the design of proper mechanical supports, which must hold the large mirror to some small allowable deflection (e.g. 10 nm rms) during polishing and testing. We discuss the design of the mechanical supports for the 1.6 m flat mirror and provide an overview of the manufacturing sequence. Finally, we provide the measurement results on the finished mirror.

5.4.2. Mirror geometry

The mirror blank glass material was solid Zerodur® (Schott, Inc.) with 1.6 m diameter and 20 cm thickness (8:1 aspect). Figure 5.1 shows the mirror geometry, and Table 5.1 lists the geometry and material parameters for the mirror blank. The mechanical support design was optimized based these parameters. The mirror was supported from the back surface (zenith pointing) during the entire manufacturing process.

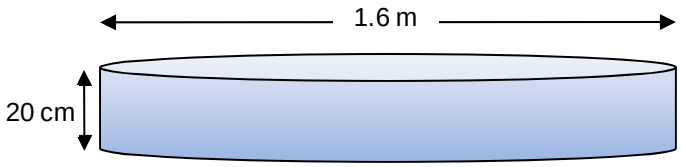

FIGURE 5.1. The 1.6 m Zerodur® flat mirror blank geometry.

TABLE 5.1. Parameters for the 1.6 m Zerodur® flat mirror blank.

Parameter	Value
Diameter, d	1.6 m
Thickness, t	0.20 m
Poisson's ratio, υ	0.243
Modulus, E @ 20°C	9.1×10^{10} N/m^2
Density, ρ	2530 kg/m^3
Total mass, m	1034 kg

5.4.3. Mirror support design

Mechanical polishing supports for large mirrors are an important design consideration. The supports must control the mirror self weight deflection to some small allowable

amount. Nelson et al. point out that for large (thin) mirrors, the number of support points and their arrangement control the mirror deflection with varying accuracy [72-73]. For the 1.6 m flat, Nelson's design for a 36 support point system arranged in a circular pattern was used as a baseline. This design was modeled and optimized in the finite element analysis (FEA) software. The analysis showed that this support system maintained the mirror surface deflection to less than 3 nm rms [74]

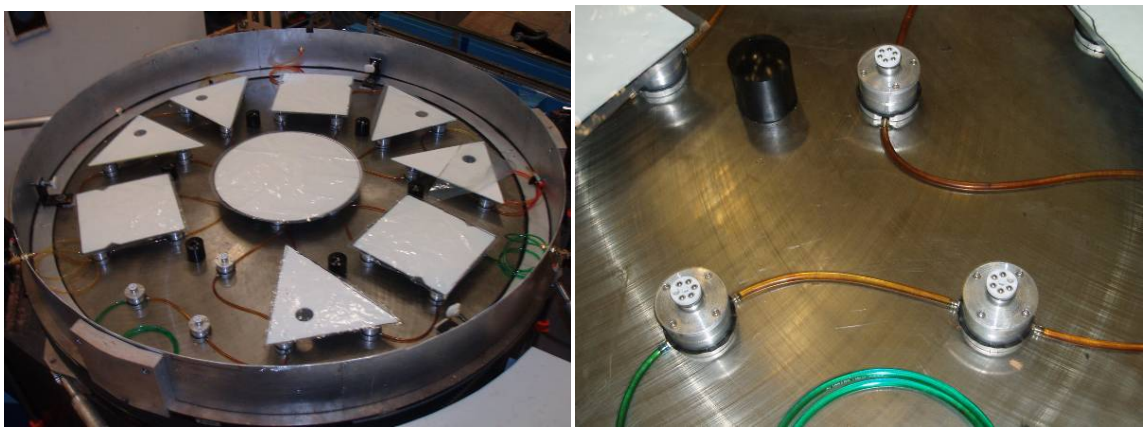

FIGURE 5.2. The mechanical support system used 36 hydraulic actuators to support the 1.6 m flat mirror (left), and a blow up of the plumbing of the hydraulic support points (right). The black cylinder (right figure) is one of six hard contact points; they do not contact the mirror in operation.

Our final polishing support design consisted of 36 hydraulic piston type actuators laid out on the high performance air bearing polishing table as shown in Figure 5.2. Aluminum plates (square and triangular) were placed between the mirror and the actuators to protect the mirror back surface. Once the mirror was positioned on the hydraulic supports, it remained there the entire fabrication; polishing and testing were performed without removing the mirror. This approach lent itself to efficient

manufacturing. In addition, this approach minimized transfers of the mirrors and, thus, risk of damaging the mirror.

5.4.4. Overview of the manufacturing sequence

The manufacture of large mirrors requires four phases: surface generation, grinding, polishing, and figuring [10-11, 71]. We performed the grinding, polishing, and figuring. After surface generation, the remaining three phases of the manufacture were carried out in the following sequence:

1. First, we used a 100 cm diameter tool faced with ceramic tiles on the Draper machine to grind out the generating marks and subsurface damage caused by the diamond cutting tool. The same 100 cm tool was used with molded soft pitch to polish the surface to a smooth finish and minimize power and asymmetrical surface variations. The mirror rested on foam pads during this step.
2. During grinding and initial polishing, we periodically checked the global surface changes with electronic levels. Polishing with the 100 cm tool continued until the surface was smooth (with no visible marks and subsurface damage) and the measured power in the mirror was 100 nm rms or better.
3. Next, the mirror was moved to the air bearing table and onto the hydraulic polishing supports. We switched to smaller tools (size ranging from 15 to 40 cm diameters) for polishing and figuring. A Draper machine was retrofitted with a radial stroker (described in Section 4.5.8), which drove the smaller tools. (Note: We initially used a 60 cm tool for surface figuring. After we failed to converge (Figure 5.12), we switched to smaller tools and the radial stroker)

4. We used the scanning pentaprism system and the 1 m Fizeau interferometer to monitor the mirror surface and guide the polishing/figuring.
5. We used polishing simulation software (described in Section 4.5.9) to help with the polishing decisions. The software provided optimized tool stroke and dwell to reduce the surface zones.

5.4.5. Large tool polishing

The grinding and coarse polishing were performed with a stiff 100 cm diameter tool on a Draper machine. The tool applied about 0.3 pounds per square inch (psi) of pressure on the mirror. Grinding was performed with tiles set in pitch on the work surface side of the tool. For polishing, molded soft pitch in 10 cm squares was applied to the bottom of the tool with about 1 cm channels between the squares. Before each polishing run, the tool (with pitch) was first pressed out overnight on a flat surface. This step ensured a 'flat' tool at the beginning of a polishing run. Barnesite [11], a popular polishing compound that has been used successfully at our facility, was used as the polishing compound or slurry. To start polishing, the slurry was liberally applied to the mirror surface, and the large tool was placed on top. The motions of the tool were adjusted based on the measured surface data from the electronic levels and historical behavior of the large tool with pitch and Barnesite. The tool was allowed to charge for a short time, after which it was timed for the actual polishing run. Charging the surface refers to the process of the polishing compound particles embedding themselves in pitch where they can remain active for a period of time and is essential for efficient polishing. The mirror surface was

always kept wet with slurry throughout the polishing run. Figure 5.3 shows the 100 cm polishing tool and the polishing process.

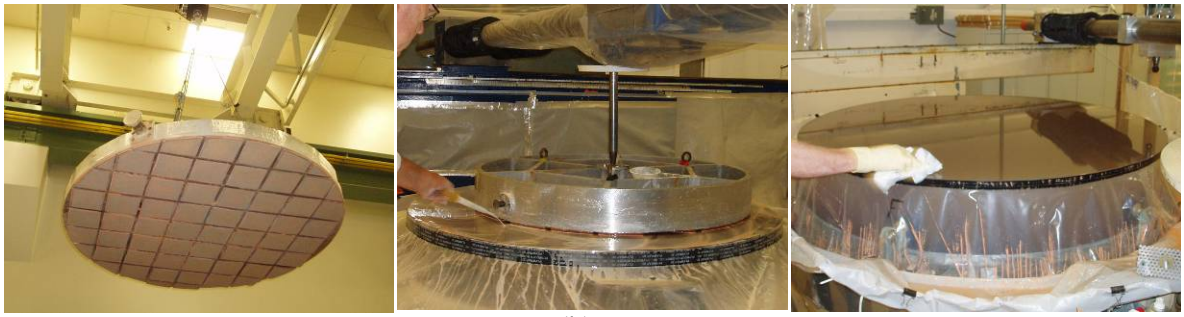

(a) (b) (c)

FIGURE 5.3. (a) Large (100 cm) tool with square tiles in pitch used for grinding. (b) Grinding/polishing with the large tool. (c) 1.6 m flat mirror polished to a smooth finish with a large tool.

The mirror edge is always a concern during fabrication. Driving the tool over the edge of the mirror can cause unpredictable removal at and near the mirror edge [77-78] as the glass at the edge experiences a linear pressure gradient from the overhanging tool. The pressure gradient and unpredictability increases as the tool is driven further over the edge. A high removal at the edge causes edge 'roll-off.' Because it is necessary to drive the tool over the edge, extra care was taken in monitoring the edge through thorough sampling with the electronic levels and visual inspections with a 10 cm test plate.

5.4.5.1. Efficient metrology

Periodic surface measurements were performed with the electronic levels to monitor the global surface and edge changes. Sampling for global surface changes requires at least two measurements across the diameter of the mirror. But to monitor the mirror edges, we

sampled more thoroughly near the edges (1 cm measurement spacing). The electronic levels measured surface slopes to which we fitted slope functions derived from low order Zernike polynomials. Multiple measurements at different orientations on the mirror generated a fitted two-dimensional surface map that showed only low order surface modes (e.g. power and astigmatism).

5.4.6. Surface finishing with small tools

Large stiff polishing tools (> 75 cm diameter) can remove more glass than small tools. Therefore, a large tool can easily make global surface changes without introducing much surface ripple. However, large tools are not very useful in controlling the mirror surface shape, especially if the surface is flat. Therefore, smaller tools with easily controlled and measured influence are used for surface figuring and finishing.

Small tools with sizes ranging from 15 to 40 cm diameters at pressures 0.2 to 0.3 psi were used for surface figuring after failing with a 60 cm tool on the Draper machine (as mentioned in Section 5.4.4). Channeled square molded pitch was applied to bottom side of each tool. Before a tool was used, it was pressed out on a flat surface.

We developed a radial stroker, shown schematically in Figure 5.4, to drive the smaller tools. The radial stroker was attached to the rail of the Draper polishing machine, which used a high quality rotary air bearing table to hold the mirror blank. The radial stroker used two motors; one motor provided a variable tool stroke motion, and the other provided variable tool rotation. The radial stroker provided rotation rates of the tool up to 8 revolutions per minute (rpm). Unlike large tools, the radial stroker with small tools allowed for zonal changes to the mirror surface. Depending on the zone width and height

determined from the surface measurements, a proper tool size was chosen to reduce the zone height by 40 to 50% in a single run. This conservative approach avoided removing too much glass and creating a low zone. A low zone correction requires the entire surface to be brought down to that level. The small tool was positioned over the high zones by moving the Draper machine rail, which normally would provide stroke for large polishing tools. Polishing simulation software, used to optimize the polishing tool stroke and dwell, enabled computer control to correct the surface figure. We describe our computer control polishing method next.

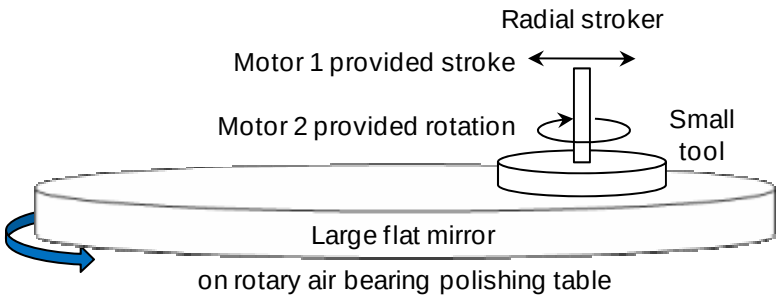

FIGURE 5.4. Schematic of the radial stroker and polishing/figuring with small tools. This radial stroker was attached to the Draper machine rail. Two motors provide variable tool stroke and rotation.

5.4.6.1. Computer controlled polishing

We developed computer controlled polishing for surface figuring through the use of polishing simulation software. The computer control came from the choice of polishing strokes based on computer simulation and optimization. The polishing simulation software is based on the finite element modeling of the lap and glass mechanics and

assumed Preston's relation, that glass removal rate is proportional to pressure and velocity between the tool and the mirror. The software differed from most by allowing the use of a rotating tool with a removal function that varies significantly with position of the tool on the mirror [79]. The computation of the removal function at any point on the mirror is made by numerically integrating Preston's relation over the tool stroke position and mirror rotation angle.

The software simulated polishing given the proper polishing parameters (i.e. tool size, pressure and geometry, tool and mirror rotation speeds, etc.). Parameters such as the tool dwell, stroke and position were then optimized for a particular surface zone. Each surface zone required its own data file. Multiple zonal data files can be combined to simulate their combined effect on the mirror. The design of the full polishing run was then given to the optician to execute on the mirror.

In order to predict the surface removal, we first calibrated the Preston's constant. Preston's equation is related to the rate of the material removal caused by the tool velocity and pressure for each point on the mirror relative to the glass:

$$R(p,v) = K \times p \times v\,. \tag{5.1}$$

where R is the local removal rate

K is Preston's proportionality constant (units μm/hr/psi/m/s)

p is the local tool pressure

v is the instantaneous linear velocity of the tool relative to the mirror surface.

Preston's constant accounted for other parameters such as the behavior of the polishing compound. To use the software successfully, the Preston's constant first

required calibration by measuring the effects of the polishing strokes and tool dwell. The result of our calibration of Preston's constant is shown in Figure 5.5. A simple polishing run was designed and simulated with the software. The simulation was then executed on the mirror. The mirror surface was measured before and after this polishing run. Preston's constant was adjusted in software until simulated surface removal matched the actual removal amplitude. The resulting constant was then recorded and stored for future simulations. A typical value for our process was 15 μm/hr/psi/m/s.

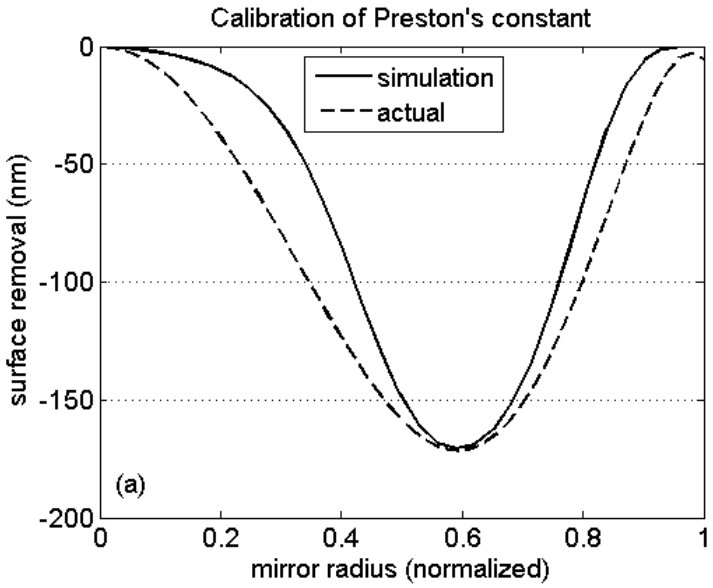

FIGURE 5.5. The result of Preston's constant calibration. In software Preston's proportionality constant was adjusted until the simulated surface removal matched the actual removal amplitude.

For a mirror with only zonal errors, the radial surface profile can be written as

$$z = f(\rho), \quad (0 \le \rho \le r). \tag{5.2}$$

In software, a removal profile can be generated for a measured surface zone. After applying the removal profile to the zone in the mirror, the new mirror surface profile will take the form

$$z_1 = f_1(\rho) = f(\rho) - h_1 \times g_1(\rho), \tag{5.3}$$

where h_1 is the removal depth at ρ_1 (typically 40 to 50% of the maximum zone height)

$g_1(\rho)$ is the removal profile normalized to 1 with its center peak at ρ_1.

The resulting surface profile after applying N different removal profiles (or equivalently polishing runs) to the mirror is then given by

$$z_N = f_N(\rho) = f(\rho) - \sum_{i=1}^{N} h_i \times g_i(\rho). \tag{5.4}$$

Figure 5.6a shows an example of designing removal functions for a measured surface radial profile exhibiting two zonal errors. The ideal removal profile is an inverted surface radial profile reduced in height. Figure 5.6b shows the surface after applying the removal functions, which results in a new surface with smaller zone heights.

Once the profiles of the ideal removal functions are established, the goal is to duplicate the profiles by choosing the right tool size, pressure, and rotation rates and then optimizing tool stroke and dwell.

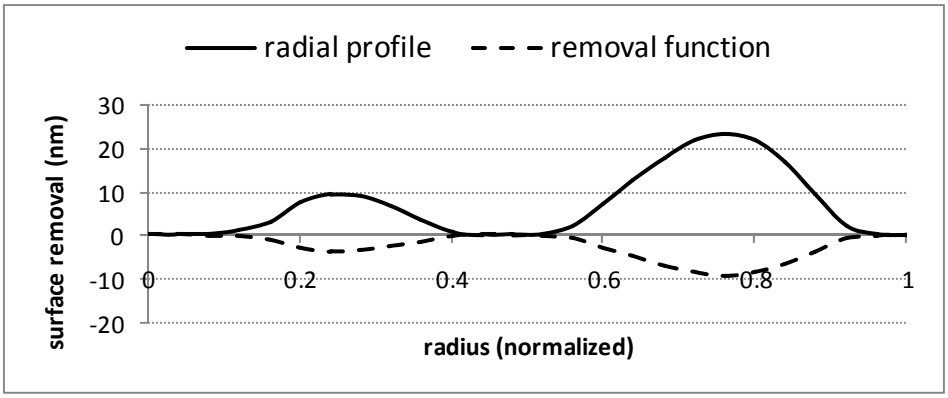

(a)

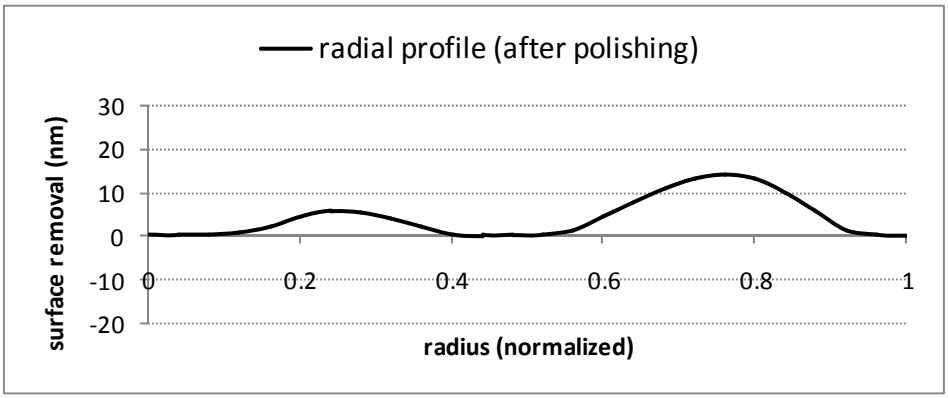

(b)

FIGURE 5.6. Example of reducing zone heights with proper design of removal functions assuming only zonal errors are present in the surface. (a) Initial measured surface radial profile showing two zones and the removal functions designed for each zone. (b) Surface after applying the removal functions.

Figure 5.7 shows a real example of the result of a polishing simulation, which consisted of multiple removal functions with varying tool sizes and dwells, and the actual surface removal after the computer controlled polishing was applied to the mirror. The actual removal departs from the predicted for two reasons: smoothing and non-linear behavior [79]. The polishing tool provides natural smoothing of the mirror surface. In addition, Preston's constant may vary with velocity and pressure, $K(p, v)$, resulting in non-linear removal effects. Although the software has evolved to include nonlinear

effects, this option was not used, because the magnitude of the nonlinear effects was not known.

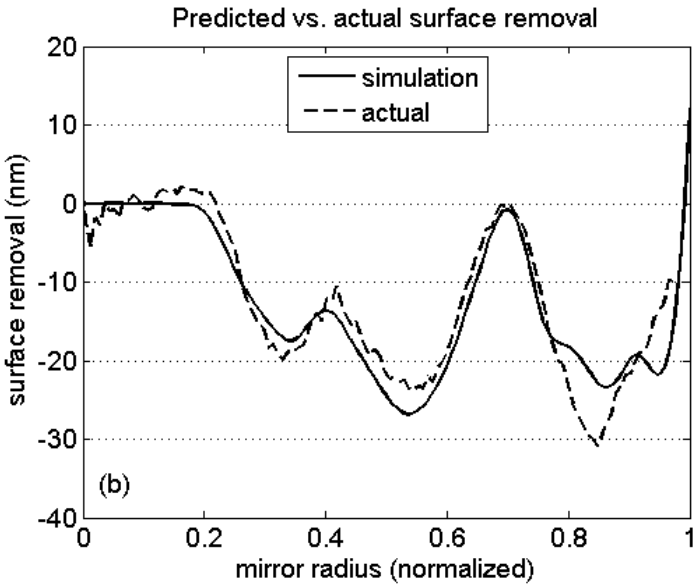

FIGURE 5.7. Comparison of a simulated and actual surface removal on the 1.6 m flat while it was in production.

Computer controlled polishing procedure

The method of computer controlled polishing was operated in a closed loop. A summary of the steps for completing a computer controlled run is given next.

1. First, the mirror surface was measured with the scanning pentaprism system and the 1 m Fizeau interferometer, and the average radial profile of the mirror was then calculated.
2. The average radial profile was imported into the polishing simulation software along with the expected polishing parameters.

3. Inside the software the surface removal function for each zone was generated and optimized. The target reduction for each zone was typically 40 to 50% of the maximum zone height.
4. The surface removal on the measured average radial profile was then simulated, and the result was evaluated.
5. Finally, the optimized polishing design was applied to the mirror. After the polishing run was complete, the process was repeated from step 1.

Figure 5.8 shows the same closed loop sequence in a flowchart. Typically, polishing runs required three to five hours to complete. This included time to change out polishing tools and move the tool to other zones on the mirror. Multiple iterations of the above sequence were carried out. In the next section, we present measurements obtained after the final run. The method of closed loop computer controlled polishing convergence of the surface figure was relatively rapid (an average of about 50 nm rms per week for power as shown in Figure 5.12).

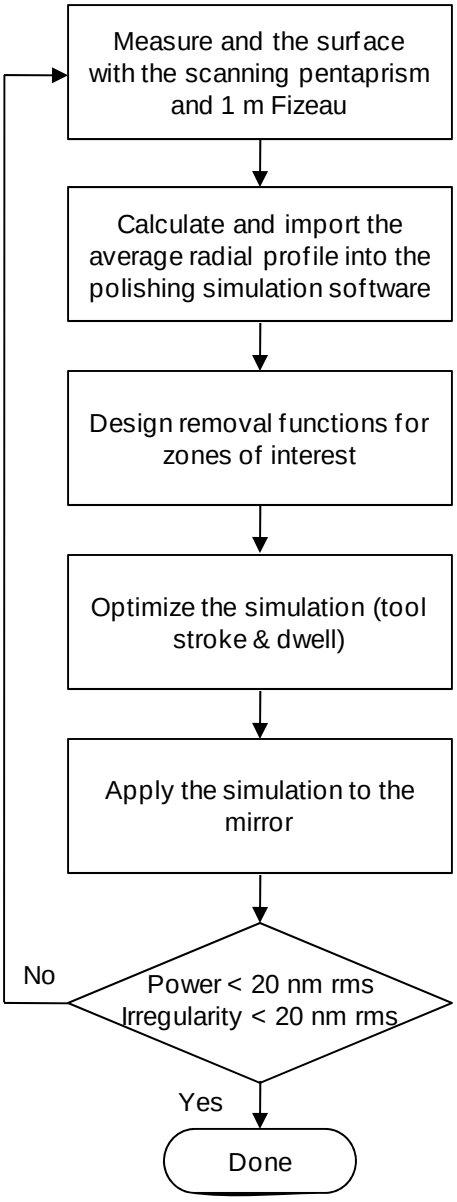

FIGURE 5.8. Flowchart diagram of the closed loop computer controlled polishing method.

5.4.6.2. Scanning pentaprism measurements for power

The result of the scanning pentaprism test on the finished mirror is shown in Figure 5.9. The measurement was made along a single diagonal line on the mirror. Forward and

backward scans were performed and the data were averaged. Only low order symmetrical Zernike polynomials were fitted to the data. The linear component of the fit gives power. This measurement resulted in 11 nm rms power with measurement uncertainty of 9 nm rms.

The large slopes due to surface irregularity were not represented well with low order polynomials. Irregularity was more accurately measured interferometrically with the 1 m Fizeau interferometer.

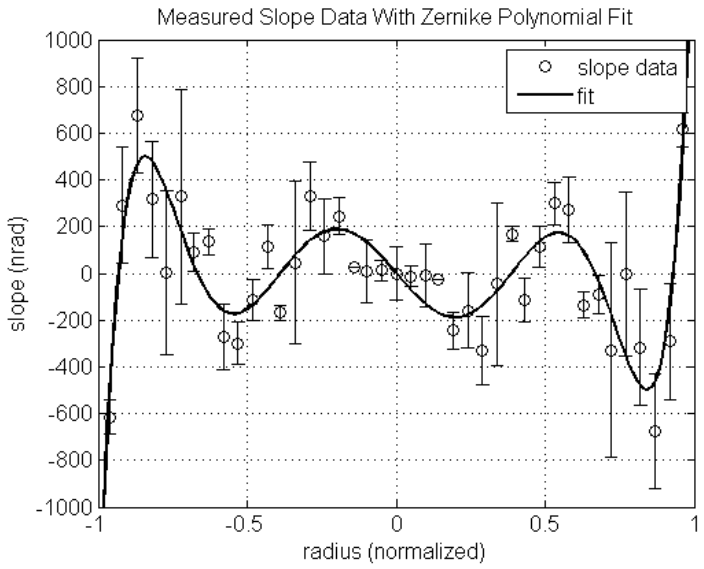

FIGURE 5.9. Measured slope data on the finished mirror with the scanning pentaprism along a single line and low order polynomial fit to the slope data. The linear component of the polynomial fit gives power in the surface (11 nm rms).

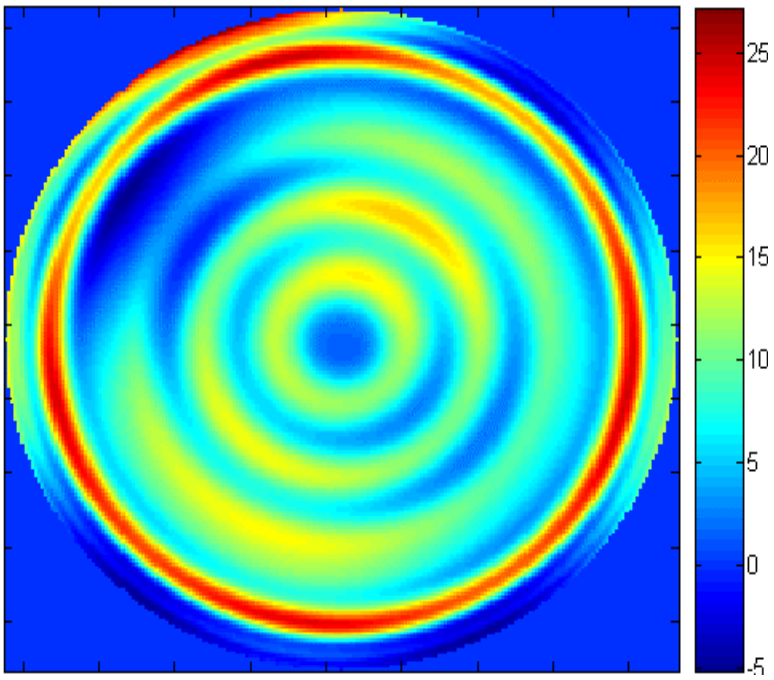

FIGURE 5.10. Result of the 1 m Fizeau measurement on the finished mirror. 24 subaperture measurements were acquired and combined with the maximum likelihood estimation (6 nm rms surface irregularity after removing power and astigmatism).

5.4.6.3. Fizeau measurements for surface irregularity

The surface map, shown in Figure 5.10, is the result of the 1 m Fizeau interferometer test on the finished mirror. A total of 24 overlapping subaperture measurements were acquired through multiple rotations of the reference and test surfaces. The subaperture measurements were combined using the maximum likelihood estimation to get a full surface map. Up to 188 Zernike terms were used to reconstruct the surface. Removing power and astigmatism leaves surface irregularity of 6 nm rms with measurement uncertainty of 3 nm rms. The results from stitching are not provided here but can be found elsewhere [17, 90].

5.4.7. Demonstration of the flat mirror with 11 nm rms power and 6 nm rms surface irregularity

Figure 5.11 demonstrates the final surface map, which is the combination of the results from the scanning pentaprism and Fizeau tests on the finished mirror: 11 nm rms power and 6 nm rms surface irregularity. The final surface was characterized to 12.5 nm rms and 57 nm peak to valley.

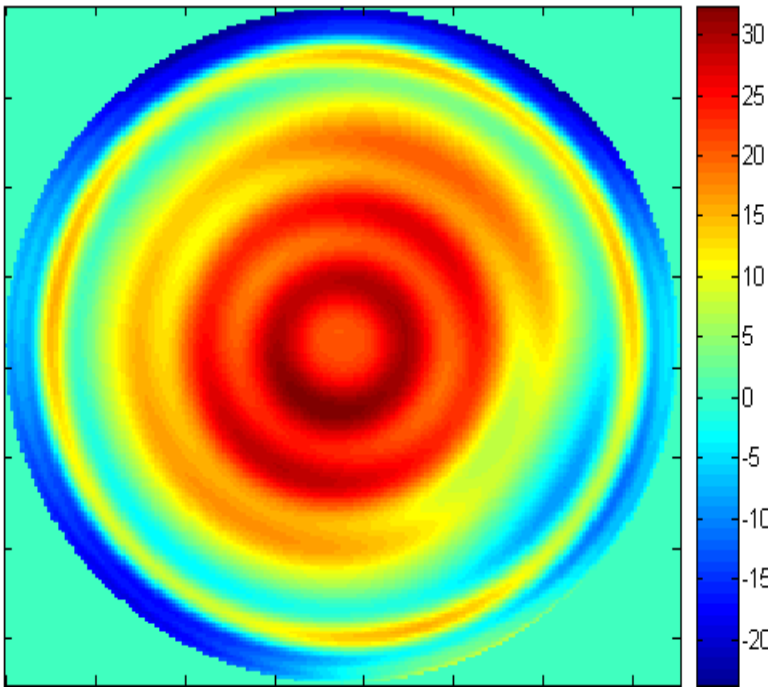

FIGURE 5.11. The final surface map showing combined power with surface irregularity from the scanning pentaprism and 1 m Fizeau tests on the finished mirror.

By continuing with the computer controlled polishing procedure described in section 5.4.6.1 and based on the sensitivities of the test systems [47, 50], we estimated 6 nm ($\lambda/100$) rms power and 3 nm ($\lambda/200$) rms surface irregularity to be achievable for 2 m

class mirrors. Due to time constraints this state of the art surface figure of 6 nm rms power and 3 nm rms irregularity was not achieved for the 1.6 m flat.

Figure 5.12 shows the rapid convergence of surface power on the 1.6 m flat mirror after implementing our computer controlled polishing. Measurements on the left side of the vertical dashed line were taken during classical large tool polishing before our computer controlled polishing. The classical polishing method used a 60 cm polishing tool to make corrections to the mirror surface. This method managed to bring the surface to about 60 nm rms power before reversing direction on the error. After several more polishing runs with the 60 cm tool and a dramatic increase in the surface power, we switched to the closed loop computer controlled method.

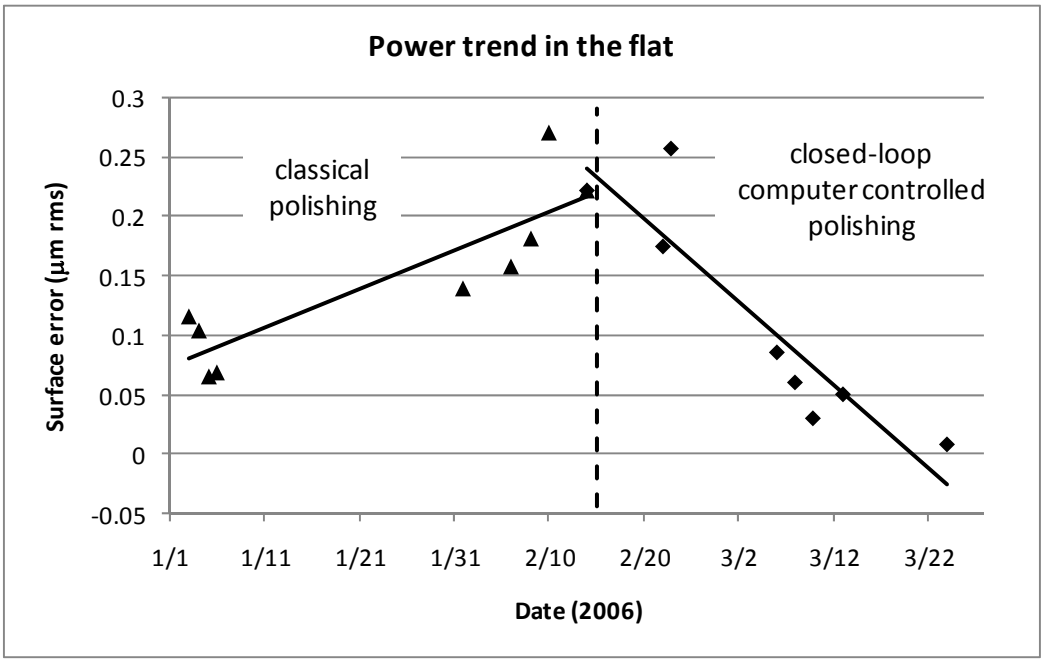

FIGURE 5.12. Power trend in the 1.6 meter flat (over about three months) as measured with the scanning pentaprism system. The power trend shows rapid convergence after implementing the polishing software aided computer controlled polishing.

5.5. Manufacture and Test Plan for a 4 m Flat Mirror

A key advantage of our manufacturing methodology described is that it is scalable to larger mirrors. In this section we discuss the feasibility of extending our methodology to 4 m class mirrors.

5.5.1. Mirror geometry

Zerodur® (Schott Glass, Inc.), ULE® (Corning, Inc.), and fused quartz are common low expansion glass materials for large mirror blanks. Each glass type has properties that make it ideal for specific applications. Zerodur®, for example, has excellent opto-thermal properties and chemical resistance, so it is typically chosen for space programs and other extreme applications. For the purpose of the analysis below, we assumed a solid Zerodur® mirror blank with a thickness of 10 cm shown in Figure 5.13 (40:1 aspect ratio).

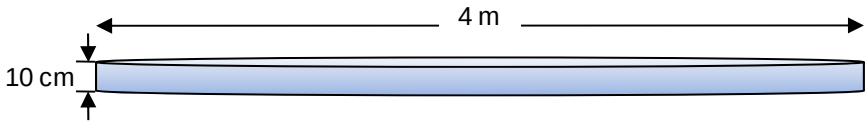

FIGURE 5.13. Solid Zerodur® 4 m flat mirror geometry.

5.5.2. Mirror support

Using the same approach described by Nelson et al. as a baseline (see Section 4.1.2), a support system with 120 points, arranged on five rings, was modeled and optimized for a mirror geometry described above. The support system arrangement is shown in Figure

5.14. From the FEA modeling this support arrangement will maintain the mirror surface deflection to about 12 nm rms after optimization [75-76].

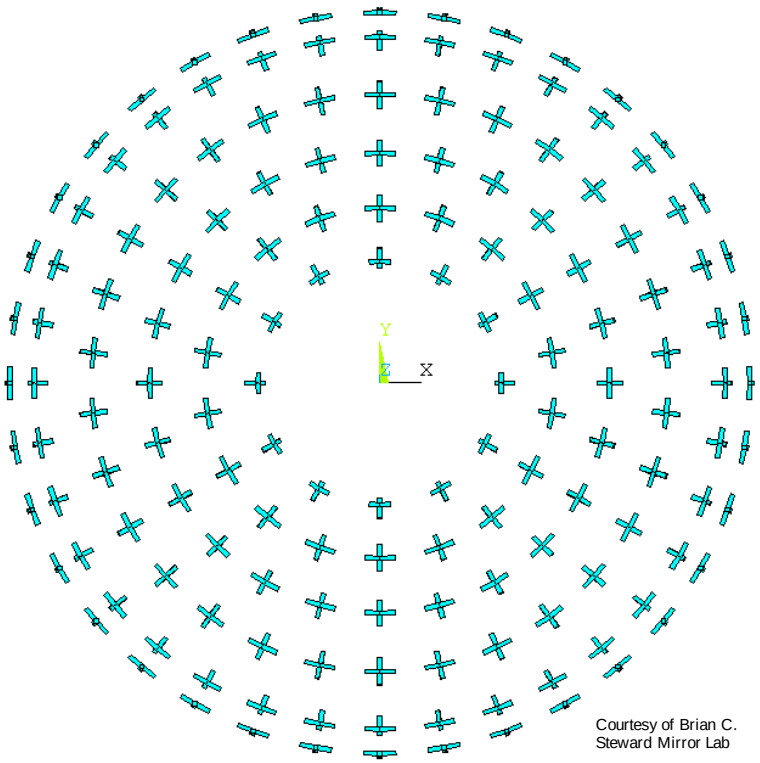

FIGURE 5.14. A five ring support design for a 4 m mirror. This design will maintain the mirror deflection to about 12 nm rms.

5.5.3. Overview of the manufacturing sequence

Many of the same processes that were established during the manufacture of the 1.6 m flat mirror can be used in larger mirror fabrication. After the mirror surface generation, the manufacturing process might proceed as follows:

1. Use a large stiff tool (≥ 100 cm) with tiles to grind and then with pitch to polish the surface to a smooth finish, minimize power and asymmetrical surface variations and carefully monitor the edges.
2. Use the electronic levels to make surface slope measurements, monitor global surface changes, and guide the initial polishing.
3. Switch to smaller tools (40 to 80 cm diameter) for figuring after the surface obtains a smooth finish and power is less than 100 nm rms.
4. Use the scanning pentaprism and 1 m Fizeau tests to monitor the surface and guide the remaining fabrication.
5. Use polishing simulation software to aid with the decisions on polishing and figuring.

Figure 5.15 shows the manufacturing sequence flowchart.

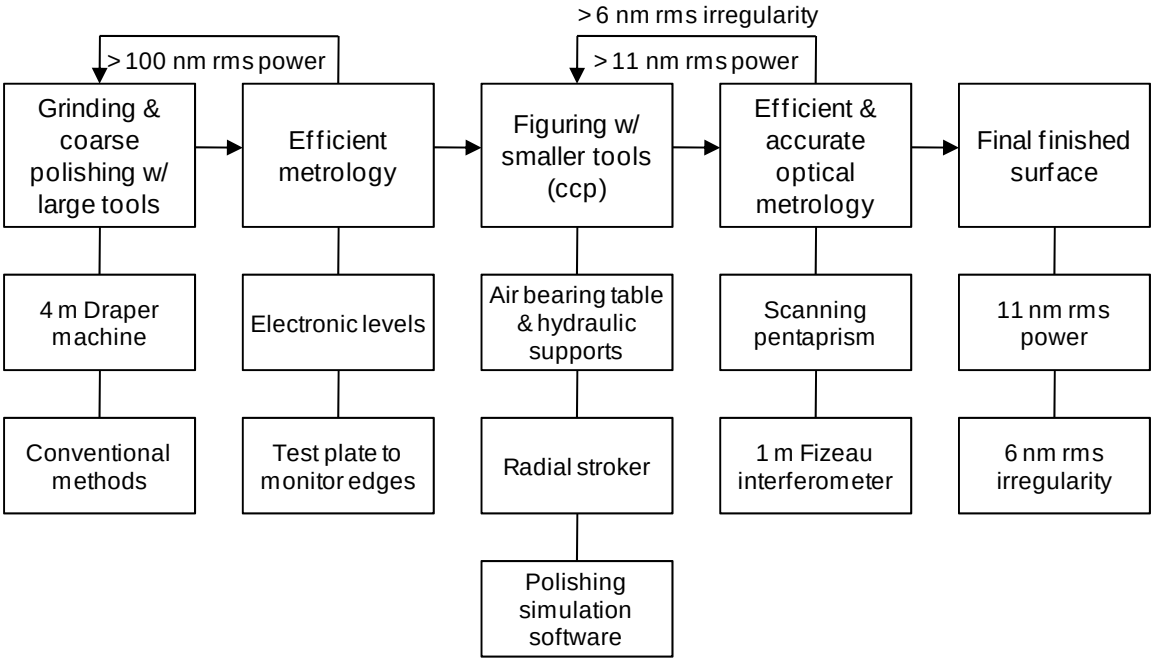

FIGURE 5.15. Potential manufacturing sequence for large high performance flat mirrors.

5.5.4. Limitations and risks

Because large mirrors may take a few years to complete, safety is a major concern when handling mirror blanks that weigh three to five tons (4 m diameter). Damage to the mirror blank is a significant risk especially during handling and transfer operations. We minimize handling, however, by keeping the mirror on one table where it is well supported (Section 5.2). Polishing and testing are performed without moving the mirror. Additionally, shop risks can be mitigated through proper training and practice.

In this section, we look at other possible limitations and risks of our developed fabrication and testing methods.

Fabrication: polishing and figuring

Our facility is currently limited to handling 4 m mirrors. Additional modifications to our polishing table are necessary to accommodate mirrors larger than 4 m.

In addition, our large tool is limited to 100 cm in diameter. A 230 cm diameter or larger tool, after characterization, can be used on a 4 m mirror for initial polishing. In some cases, polishing techniques proven for smaller mirrors do not work for large mirrors. As the tool size increases, so does the pressure it exerts on the mirror surface. This alone may change the expected polishing outcome.

To succeed within the boundary of our capability, careful planning and design is essential with special attention to gaining experience with tools and their effect on mirrors in fabrication.

Surface slope testing

For a given magnitude surface error (e.g. 20 nm rms astigmatism) the surface slope errors are inversely proportional to the mirror size. Thus, slope errors for a large mirror must become smaller to maintain the same performance as a smaller one. For power, the edge slope error is inversely proportional to the diameter of the mirror by (derived in the Appendix)

$$\Delta\theta = \frac{8s}{D}, \tag{5.5}$$

where s is the peak to valley power or sag in the mirror surface

D is the diameter of the mirror.

If the electronic levels, for example, are expected to measure 60 rms power in a 2 m mirror, then the edge slopes are 1 μrad. For the same specification on power for a 4 m mirror, the edge slopes become 0.5 μrad. The sensitivities of the test systems must be improved as the mirrors get larger.

We determined the measurement uncertainty in the electronic levels and the scanning pentaprism system [46, 50]. The results shown in Table 5.2 are of Monte Carlo simulations using the uncertainties in the slope test systems to estimate the accuracy in measuring the low order Zernike aberrations in a 4 m flat mirror assuming 0.6 μrad rms noise for the electronic levels test and 0.4 μrad rms noise for the scanning pentaprism test. This analysis assumes three diagonal line scans and 12 measurement points per scan for the electronic levels and 42 measurement points per scan for the scanning pentaprism.

TABLE 5.2. Accuracy in measuring the low order Zernike aberrations on a 4 m flat mirror.

Zernike aberration	Measurement accuracy (nm rms)	
	Electronic levels	Scanning pentaprism
Power	29	16
Cos Astigmatism	50	19
Sin Astigmatism	52	20
Cos Coma	18	7
Sin Coma	18	8
Spherical	14	5
Secondary Spherical	9	4
Root sum square	83	34

Table 5.2 shows that on a 4 m flat mirror, power can be measured to 29 nm rms with the electronic levels and to 16 nm rms with the scanning pentaprism system after including the limiting effect of the autocollimator beam divergence. The surface can be measured to about 83 nm rms and 34 nm rms of low order aberrations with the electronic levels and the scanning pentaprism system, respectively, with no or minimal modifications and upgrades to the current slope test systems. The measurement uncertainties can be reduced by averaging more data points and increasing the number of measurement points.

With the electronic levels, there is always a risk of damaging the mirror surface when placing the levels since there is a metal to glass contact. As the mirrors get larger, the difficulty of placing the levels closer to the center of the mirror increases, thus the risk level also increases. However, measurements at and near the edges are enough to

measure global errors in the surface by Equation 5.2; measuring the slopes only at the edges will reduce the risk of placing the electronic levels.

There is a potential limitation with the scanning pentaprism system: the current system uses rails that are 2.5 m in length, so the current system may become limited in size for flat mirrors 4 m in diameter or larger. Increasing the length of the rails overcomes this limitation, but the increase does two things: increases the working distance of the electronic autocollimator and picks up more noise over the longer beam paths. Both these problems may limit the test system in accuracy. But more data averaging can compensate for the additional noise and random errors.

Large Fizeau test

In the current Fizeau test the 1 m reference flat and test mirror are fixed in lateral translation. This configuration limits how large a mirror we can test by subsampling (≤ 2 m). To measure larger mirrors, another degree of freedom in lateral translation is needed for the reference flat.

Figure 5.16a shows the current subaperture sampling arrangement to measure 2 m or smaller flat mirrors. The reference flat remains fixed and the test mirror is rotated underneath to get full coverage. For a 1.6 m flat mirror eight subaperture measurements are enough to get full coverage of the test mirror [47]. This type of sampling arrangement is insufficient for flat mirrors larger than 2 m. Figure 5.16b shows an example of subsampling a 4 m mirror after introducing lateral translation of the 1 m reference flat. In this example, the reference flat is translated to three positions and the test mirror is rotated underneath to acquire 25 subaperture measurements and provide full

coverage of the mirror. All 25 measurements must be combined to get a full synthetic surface map.

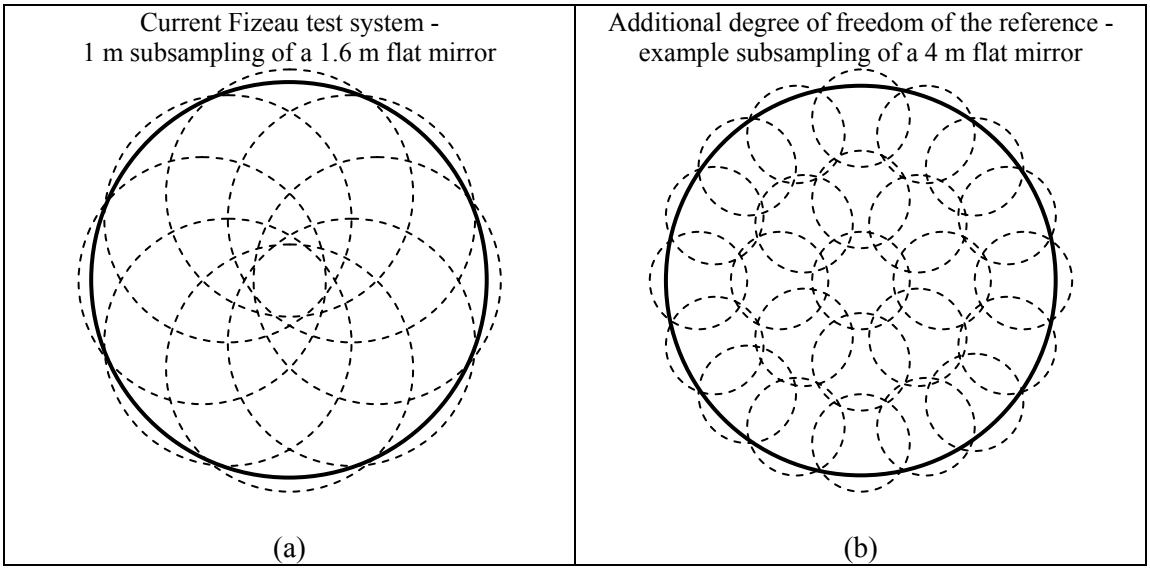

FIGURE 5.16. (a) 1 m subaperture (dashed circular outlines) sampling on the 1.6 m flat mirror, and (b) on a 4 m flat mirror. Multiple subaperture sampling provides full coverage of the large mirror. Combining the subaperture measurements produces a full synthetic map.

Errors in stitching the subaperture measurements increase as more subapertures are combined. The increase in subaperture measurements limits the accuracy of the test system. However, the quality of the test in terms of slope, power spectral density or structure function is not degraded.

5.6. Conclusion

The manufacture of large flat mirrors is challenging. We found classical polishing alone does not enable the manufacture of large high performance flat mirror much larger than 1

m diameter. We reported on the methodology and enabling technologies for fabricating and testing high performance large flat mirrors. We developed the enabling fabrication and testing technologies during the manufacture of a 1.6 m flat mirror that measured 11 nm ($\lambda/60$) rms in power and 6 nm ($\lambda/100$) rms in surface irregularity on the finished mirror. The enabling technologies are scalable for manufacture of flat mirrors as large as 8 m in diameter with proper tool design and selection. Our discussion of limitations and risks showed the accurate manufacture of a 4 m flat mirror is within our current capability.

CONCLUSION

A description of the methodology for manufacturing large high performance flat mirrors that are much larger then 1 m diameter and of solid (i.e. non light weighted) glass material has been given. We found during the manufacture of a 1.6 meter flat mirror that classical fabrication methods alone do not enable fabrication of quality large flats and current metrology for large flats are limited in efficiency and accuracy. To address these limitations, we developed computer controlled polishing that used polishing simulation software combined with accurate and efficient metrology. Two slope tests, the electronic levels and scanning pentaprism, were developed and analyzed in detail. A vibration insensitive interferometer, based on the classical Fizeau, with an external 1 meter reference flat was developed, characterized, and calibrated. The Fizeau interferometer used subaperture sampling and stitching and maximum likelihood estimation to obtain synthetic surface maps over the full aperture of the flat mirror.

The electronic levels were used during early fabrication (grinding and coarse polishing with large tools) to provide efficient determination of global changes in the mirror surface. The scanning pentaprism and the 1 m Fizeau are highly accurate tests and were used during the remaining fabrication and to qualify the surface figure of the finished mirror. The surface of the finished 1.6 m flat was measured to 11 nm rms (±9 nm rms) power and 6 nm rms (±3 nm rms) surface irregularity. At present this is the best large flat in the world.

The analysis of the risks and limitations of the fabrication methods and metrology showed that manufacturing 4 m flat mirrors is within our current capabilities. Mirrors larger than 4 meters will require modifying mechanics including the polishing machines, metrology and data analysis techniques. Changes to the fabrication include designing larger stiff tools and carefully characterizing them. Changes to the metrology include increasing the data averaging and introducing an additional degree of freedom in lateral translation for the Fizeau reference flat.

The manufacture of large flat mirror is challenging. We addressed the limitations and laid the foundation for flat fabrication by developing enabling fabrication and testing technologies. Our method of computer controlled polishing was operated in closed loop. The key advantage to our methodology is it is scalable to 8 meter flat mirrors. With proper design of the mechanics and hardware, including polishing tools, and upgrades to the data analysis software, high performance 8 meter flat mirrors are possible in the future.

The amount of work it took to finish this project was a lot more than one person can handle. It took a tremendous team effort to develop and implement the method of large flat manufacturing described in this dissertation and produce a very high performance 2 m class flat mirror. In addition to my role as the lead systems engineer on this project, I developed the electronic levels test, performed extensive analysis on the electronic levels and scanning pentaprism test systems, resulting in improved accuracies, designed polishing runs using predictive software and measured data, and, finally, integrated the metrology and fabrication methods into a closed loop manufacturing

operation that eventually produced the world's best 2 m class flat. Individuals that directly contributed technical solutions to this project were acknowledged in the beginning.

APPENDIX A

EDGE SLOPES FROM SURFACE CURVATURE

The sag in a mirror surface is defined as

$$s = \frac{r^2}{2R} \tag{A.1}$$

where r is the semi-diameter of the mirror and R is the radius of curvature. The slope in the radial direction is then

$$\theta(r) = \frac{ds}{dr} = \frac{r}{R} \tag{A.2}$$

or

$$\theta(r) = \frac{r}{R} \cdot \left(\frac{2r}{2r}\right) = \frac{2s}{r} \tag{A.3}$$

The difference between the edge slopes is now

$$\Delta\theta = \theta\left(\frac{D}{2}\right) - \theta\left(-\frac{D}{2}\right) = \frac{8s}{D}, \tag{A.4}$$

where D is the diameter of the mirror. Rearranging Equation A.4 shows slope measurements on opposing edges of the mirror are enough to measure the global curvature in the surface.

$$s = \frac{D \cdot \Delta\theta}{8}. \tag{A.5}$$

APPENDIX B

SCANNING PENTAPRISM TEST MONTE CARLO ANALYSIS OF NOISE COUPLING INTO MID ORDER ZERNIKE ABERRATIONS FOR NUMBER OF LINE SCANS, NUMBER OF MEASUREMENT POINTS AND LINE SCAN OFFSETS

This analysis is a continuation from Section 3.4.10. The Monte Carlo analysis studied measurement noise normalized to 1 μrad rms coupling into mid order Zernike aberrations (defined in Table 3.7). The parameters that were varied are the number of line scans (three to six), number of measurement points per scan, and the distance of the line scans from the center of the mirror (offset). The line scans were spaced in angle such that scans were symmetrical around the mirror.

The proceeding plots are for the case when the line scans had no offsets (i.e. the line scans go through the center of the mirror). The amounts of measurement error due to measurement noise are plotted against the number of measurement points (for each number of line scans). A function of the form $AN^{-1/2}$ was then fitted to the data points, where the *A* coefficient is the sensitivity to noise and *N* is the number of measurement points. The value of the *A* coefficient was chose that resulted in the best fit to the data points. The function shows that the measurement error decreases as $\frac{1}{\sqrt{N}}$. The sampling spacing was varied to obtain a distribution of data points for the measurement error.

Summary of the proceeding plots (Figures B.1 through B.10):

1. The analysis assumes measurement noise normalized to 1 μrad rms coupling into mid order Zernike aberrations for a 2 m flat mirror.
2. The line scans have no offset.
3. Sampling of trefoil (3θ) requires a minimum of four line scans
4. Ssampling of pentafoil (4θ) requires a minimum of five line scans.
5. The plots generally follow $AN^{-1/2}$.

TABLE B.1. Values of the *A* coefficient for the mid order Zernike aberrations for the case of the line scans with no offset.

Line scans	Trefoil		Secondary astigmatism		Secondary coma		Pentafoil		Higher order spherical	
	Z10	Z11	Z12	Z13	Z14	Z15	Z17	Z18	Z16	Z25
3	--	--	115	115	40	40	--	--	35	25
4	190	190	58	60	35	36	--	--	33	22
5	165	170	53	53	33	33	97	99	29	21
6	155	157	50	49	30	29	92	94	26	20

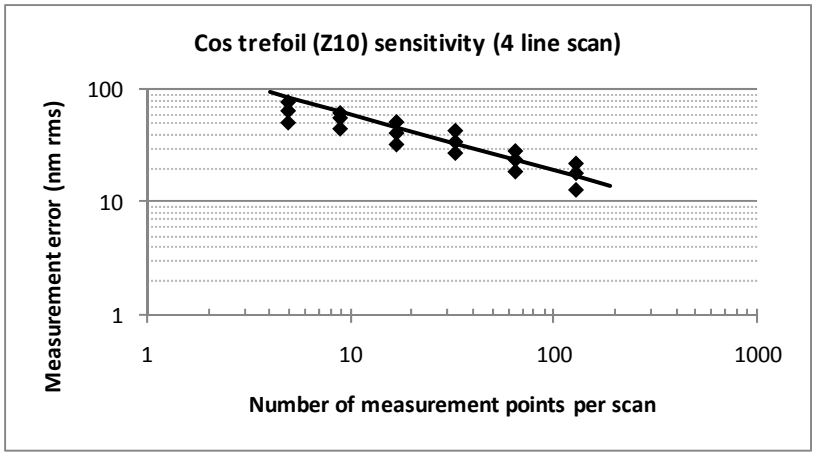

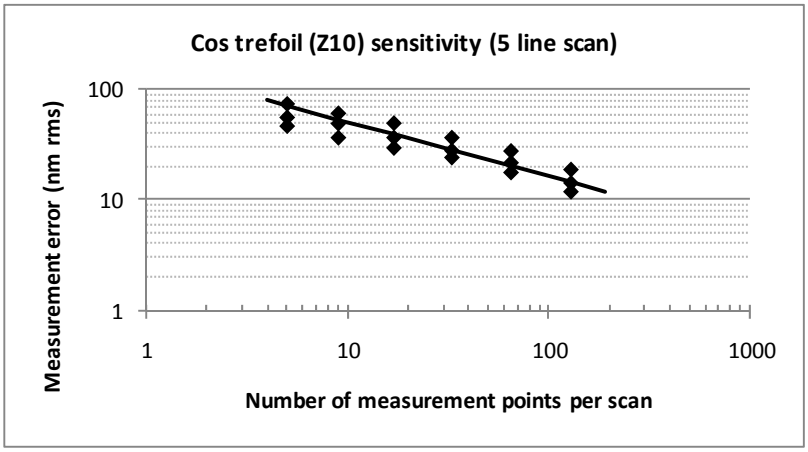

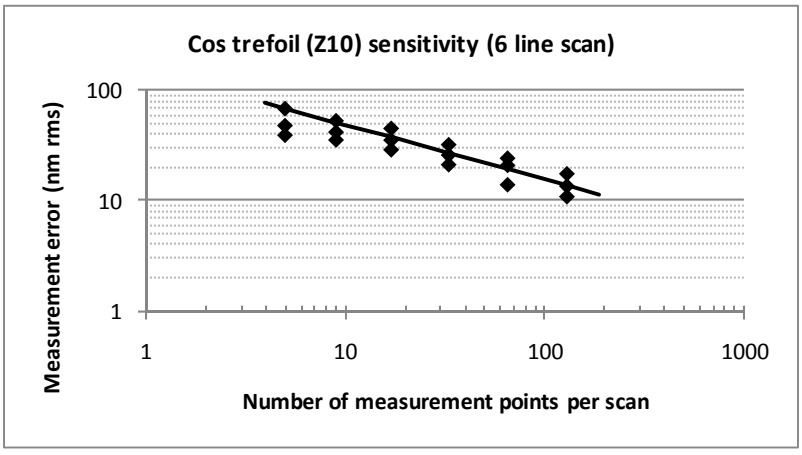

FIGURE B.1. Measurement noise normalized to 1 μrad coupling into cos trefoil (Z10) for the number of line scans and number of measurement points over a 2 m flat.

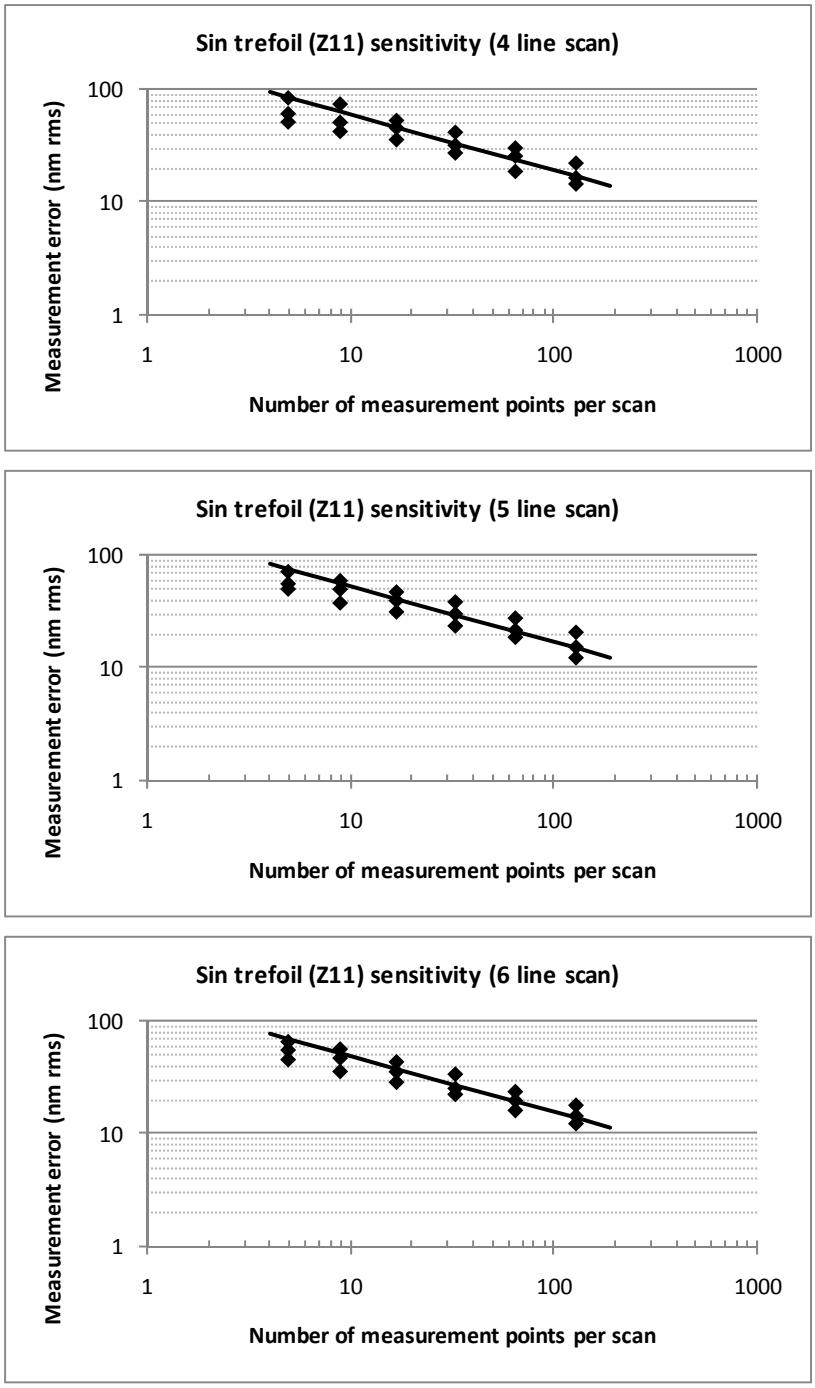

FIGURE B.2. Measurement noise normalized to 1 μrad coupling into sin trefoil (Z11) for the number of line scans and number of measurement points over a 2 m flat.

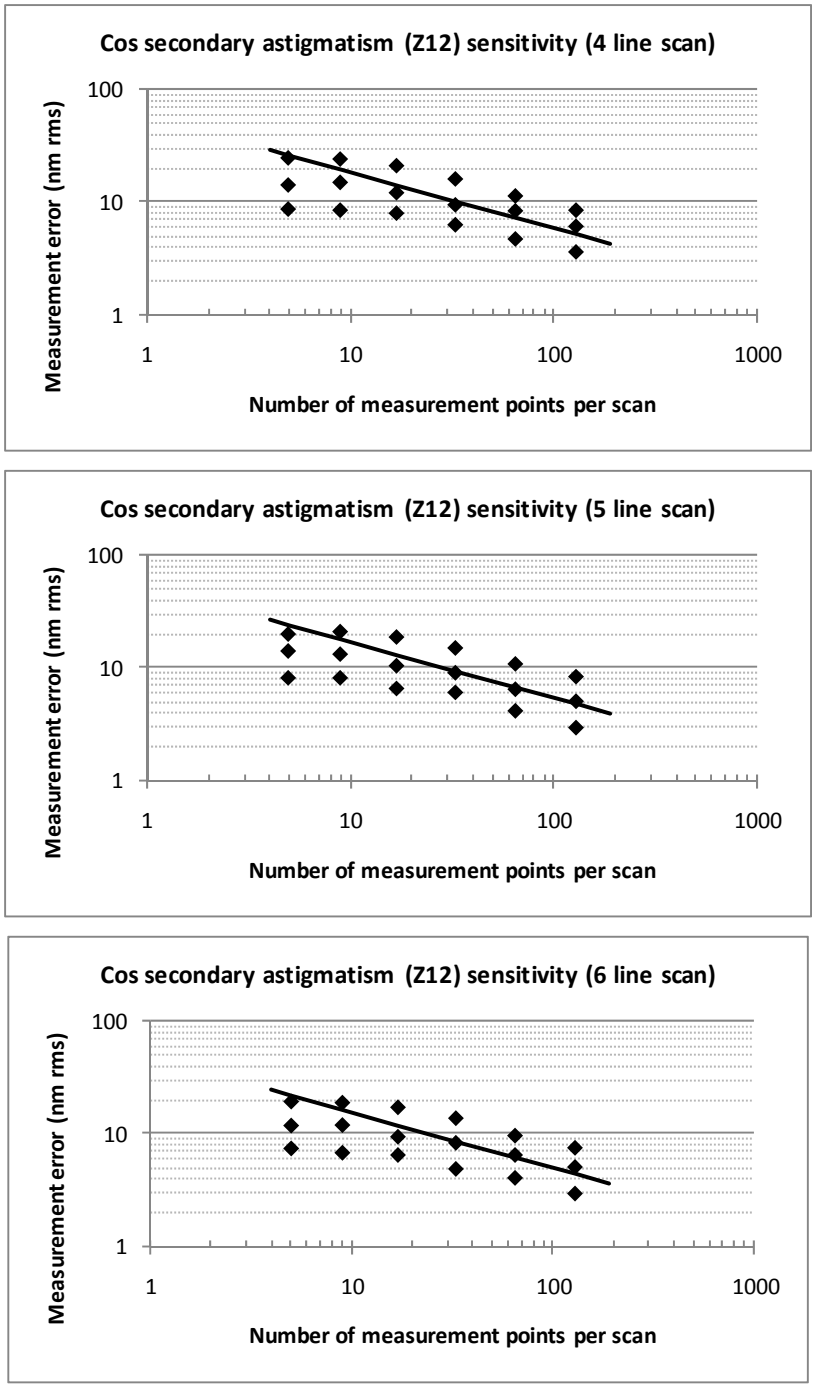

FIGURE B.3. Measurement noise normalized to 1 μrad coupling into cos secondary astigmatism (Z12) for the number of line scans and number of measurement points over a 2 m flat.

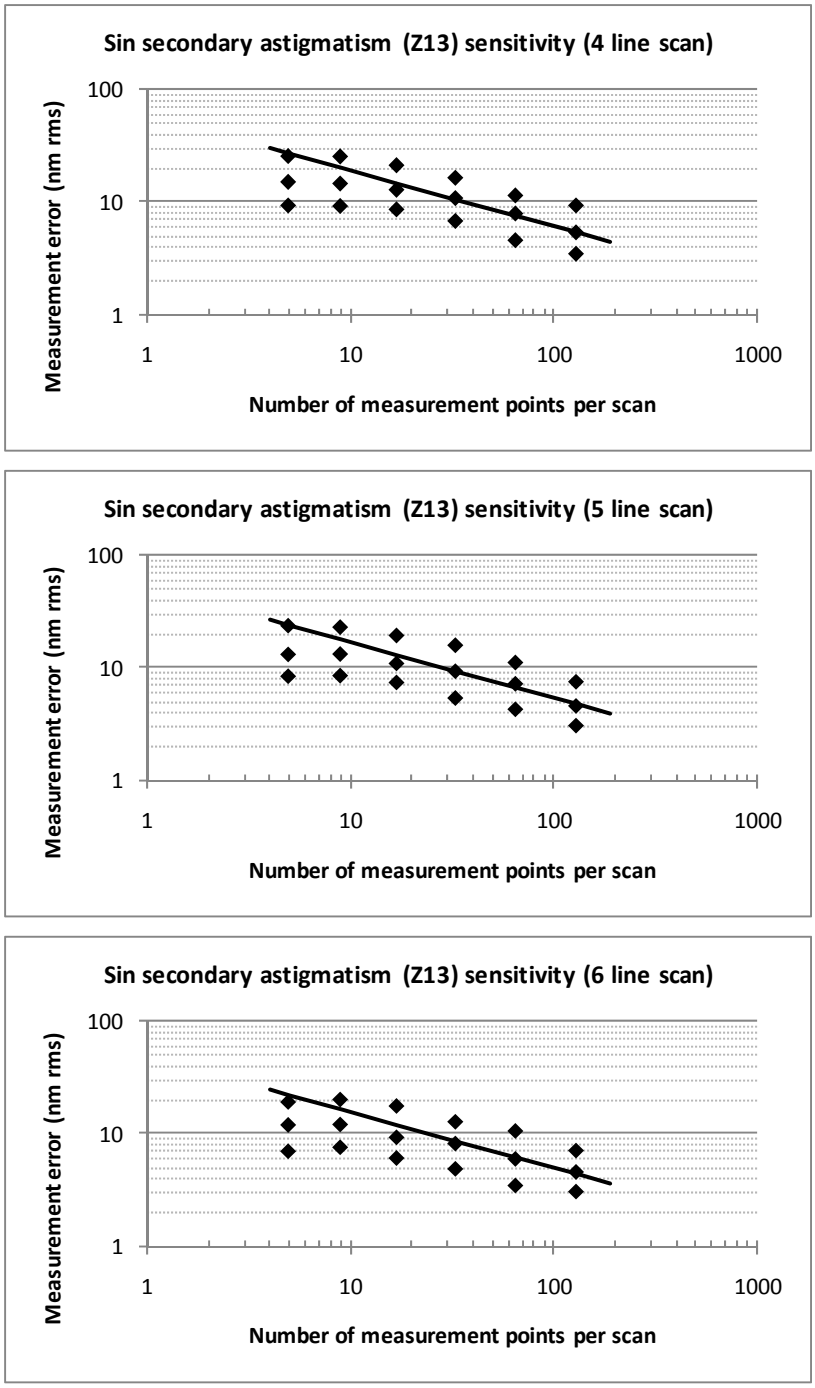

FIGURE B.4. Measurement noise normalized to 1 μrad coupling into sin secondary astigmatism (Z13) for the number of line scans and number of measurement points over a 2 m flat.

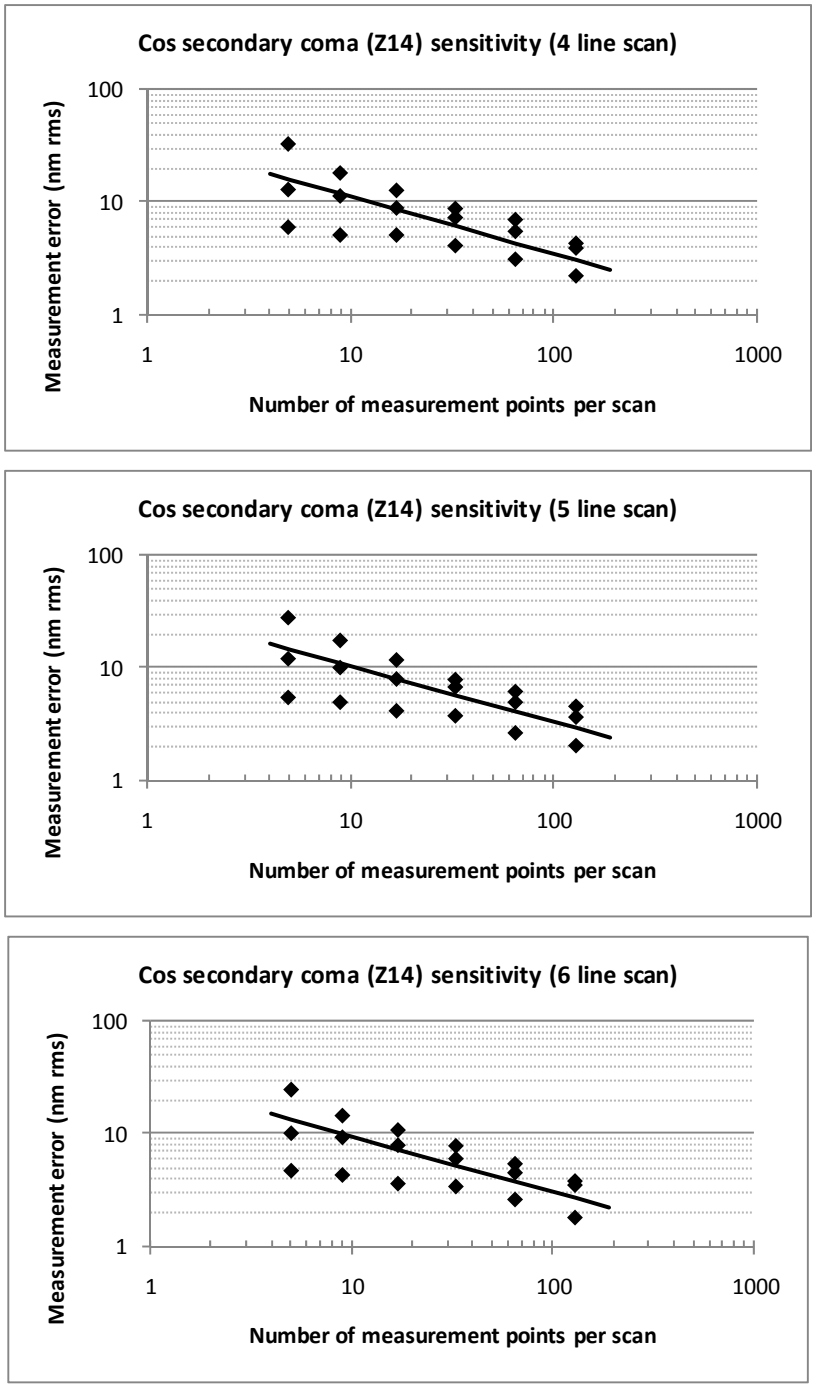

FIGURE B.5. Measurement noise normalized to 1 μrad coupling into cos secondary coma (Z14) for the number of line scans and number of measurement points over a 2 m flat.

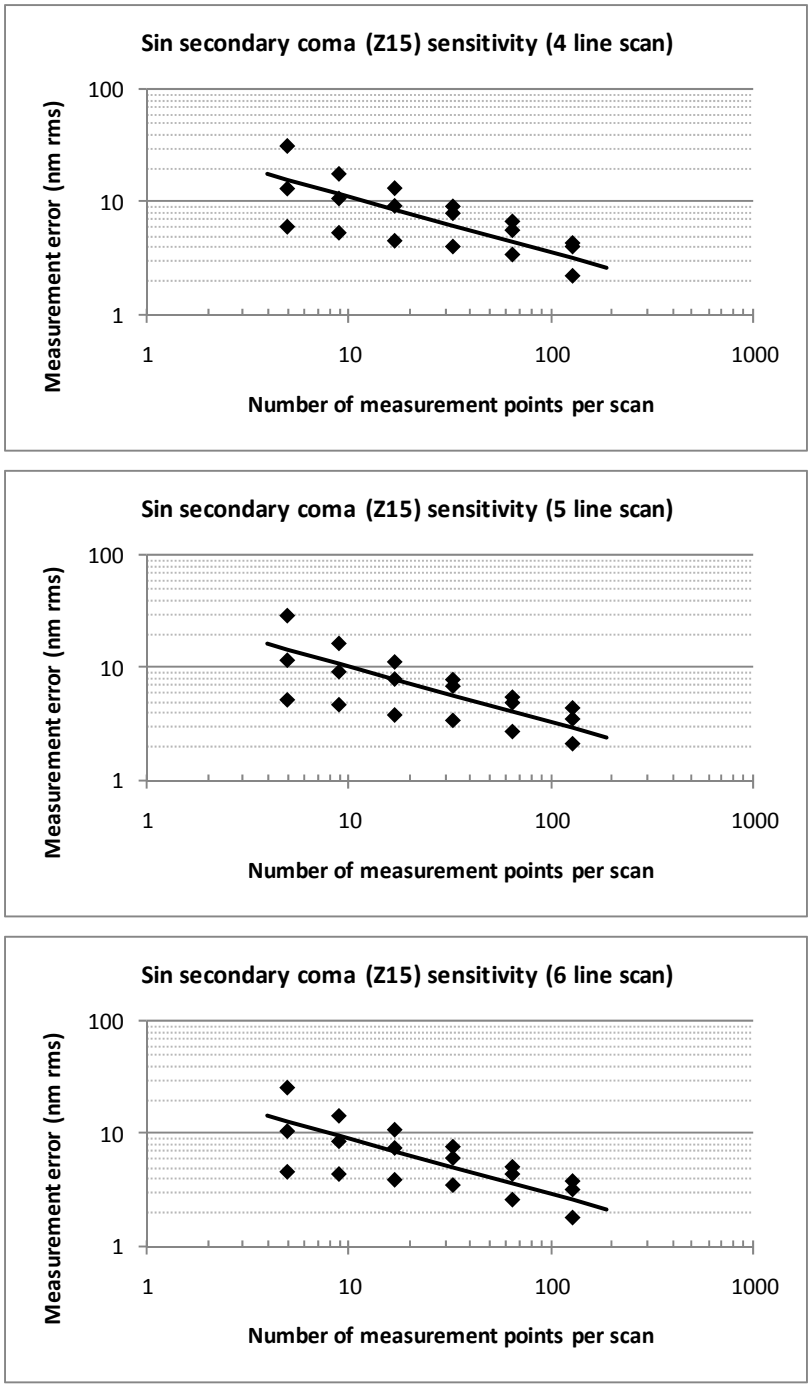

FIGURE B.6. Measurement noise normalized to 1 μrad coupling into sin secondary coma (Z15) for the number of line scans and number of measurement points over a 2 m flat.

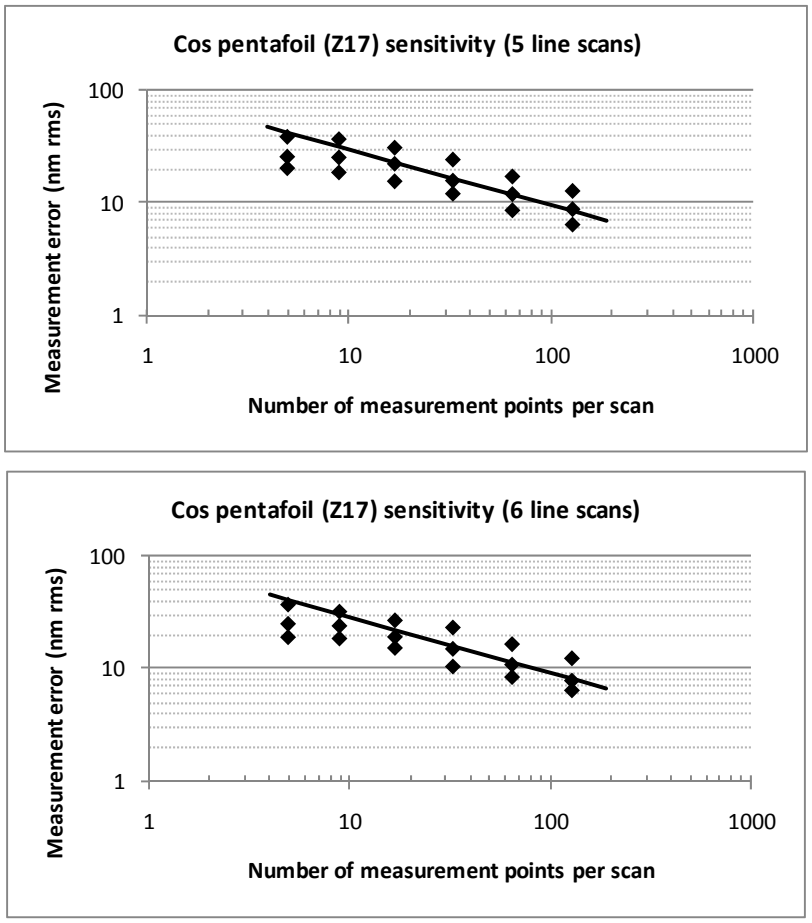

FIGURE B.7. Measurement noise normalized to 1 μrad coupling into cos pentafoil (Z17) for the number of line scans and number of measurement points over a 2 m flat.

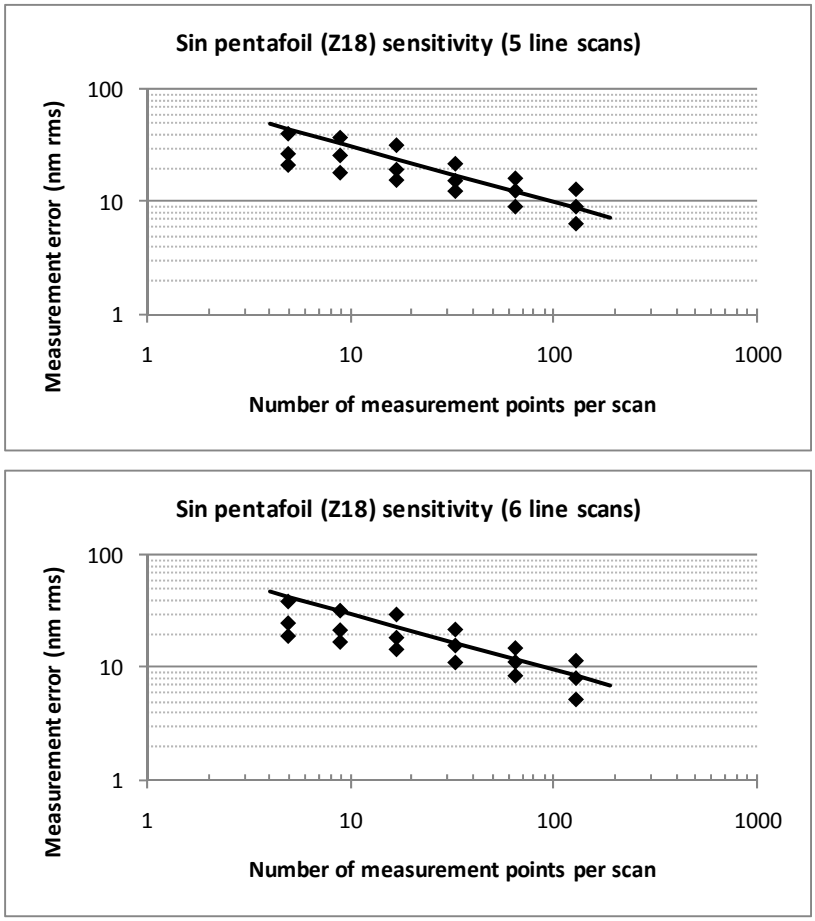

FIGURE B.8. Measurement noise normalized to 1 μrad coupling into sin pentafoil (Z18) for the number of line scans and number of measurement points over a 2 m flat

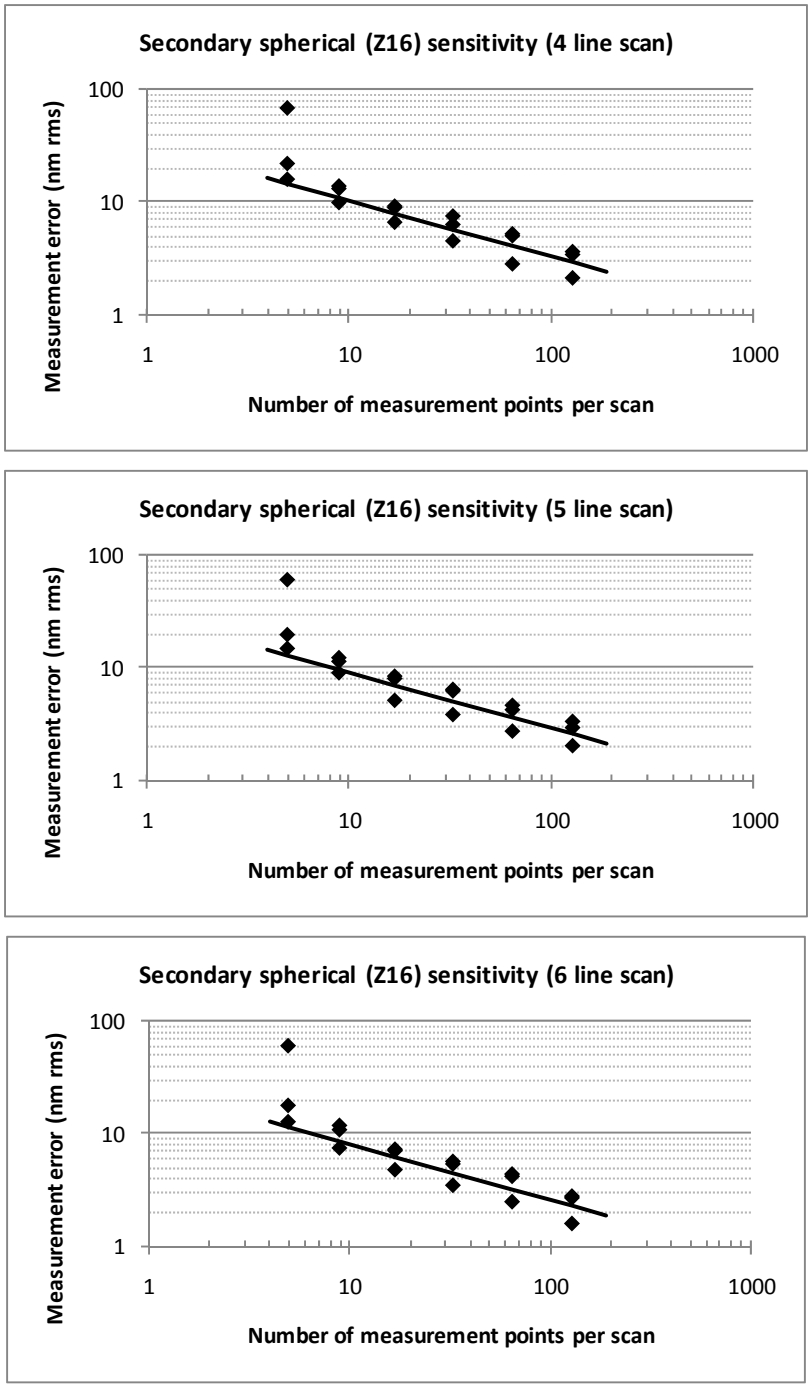

FIGURE B.9. Measurement noise normalized to 1 μrad coupling into secondary spherical (Z16) for the number of line scans and number of measurement points over a 2 m flat.

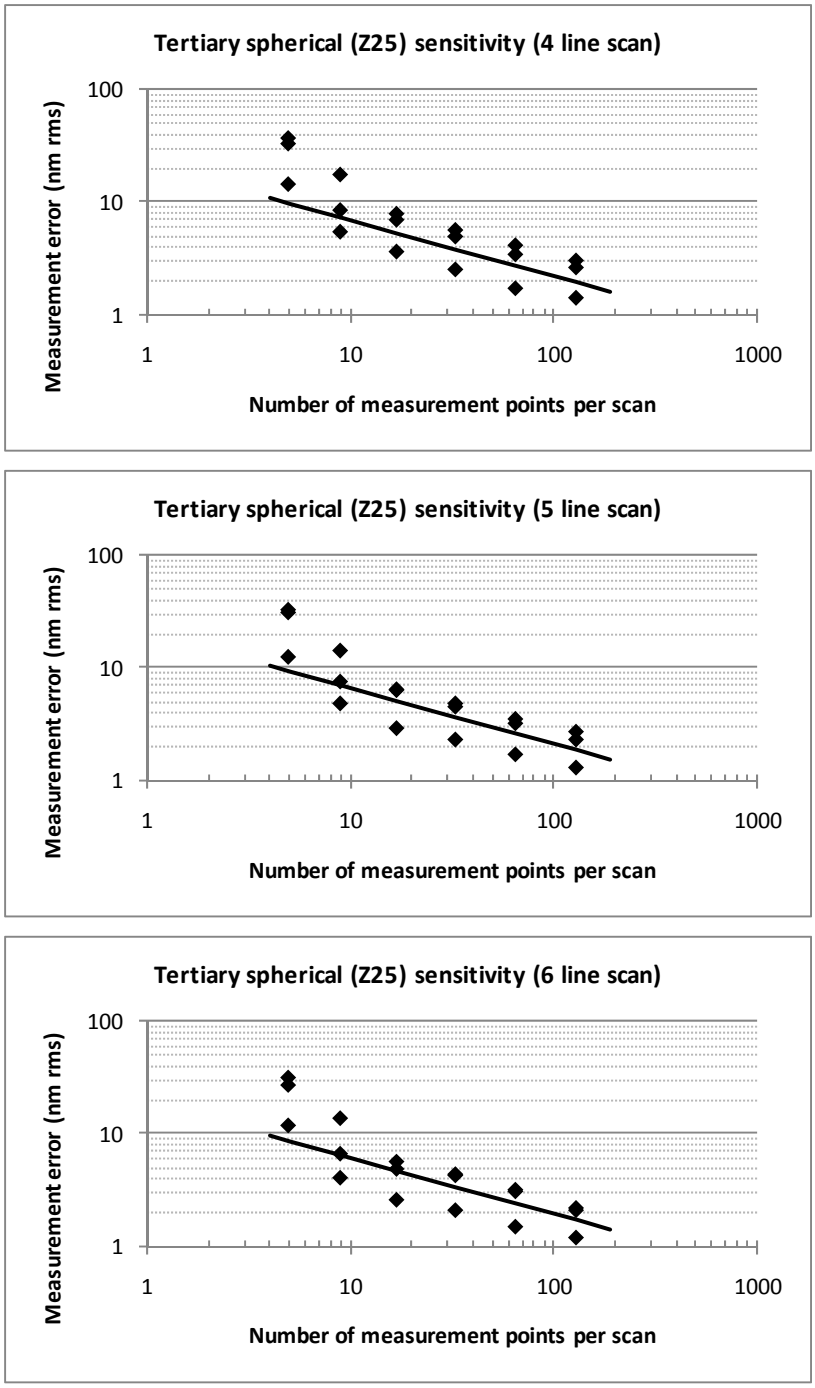

FIGURE B.10. Measurement noise normalized to 1 μrad coupling into tertiary spherical (Z25) for the number of line scans and number of measurement points over a 2 m flat.

The proceeding plots are for the case when the line scans offsets was 250 mm as shown in Figure B.11. The amounts of measurement error due to measurement noise are plotted against the number of measurement points (for each number of line scans). A function of the form $AN^{-1/2}$ was fitted to the data points, where *A* coefficient is the sensitivity to noise and *N* is the number of measurement points. Only the fitted functions are plotted to get all the number of line scans in a single plot.

Summary of the proceeding plots (Figures B.12 through B.16):

1. The analysis assumes measurement noise normalized to 1 μrad rms coupling into mid order Zernike aberrations for a 2 m flat mirror.
2. The line scans have 250 mm offset from the mirror center.
3. Sampling of trefoil (3θ) requires a minimum of four line scans.
4. Sampling of pentafoil (4θ) requires a minimum of five line scans.
5. The plots generally follow $AN^{-1/2}$ (Note: Except for small *N* due to under sampling).

TABLE B.2. Values of the *A* coefficient for the mid order Zernike aberrations for the case of the line scans with 250 mm offsets.

Line scans	Trefoil		Secondary astigmatism		Secondary coma		Pentafoil		High order spherical	
	Z10	Z11	Z12	Z13	Z14	Z15	Z17	Z18	Z16	Z25
3	--	--	50	49	36	36	--	--	39	30
4	122	125	34	52	30	29	--	--	37	25
5	108	110	38	39	27	27	92	90	29	22
6	100	102	35	35	26	25	82	82	27	21

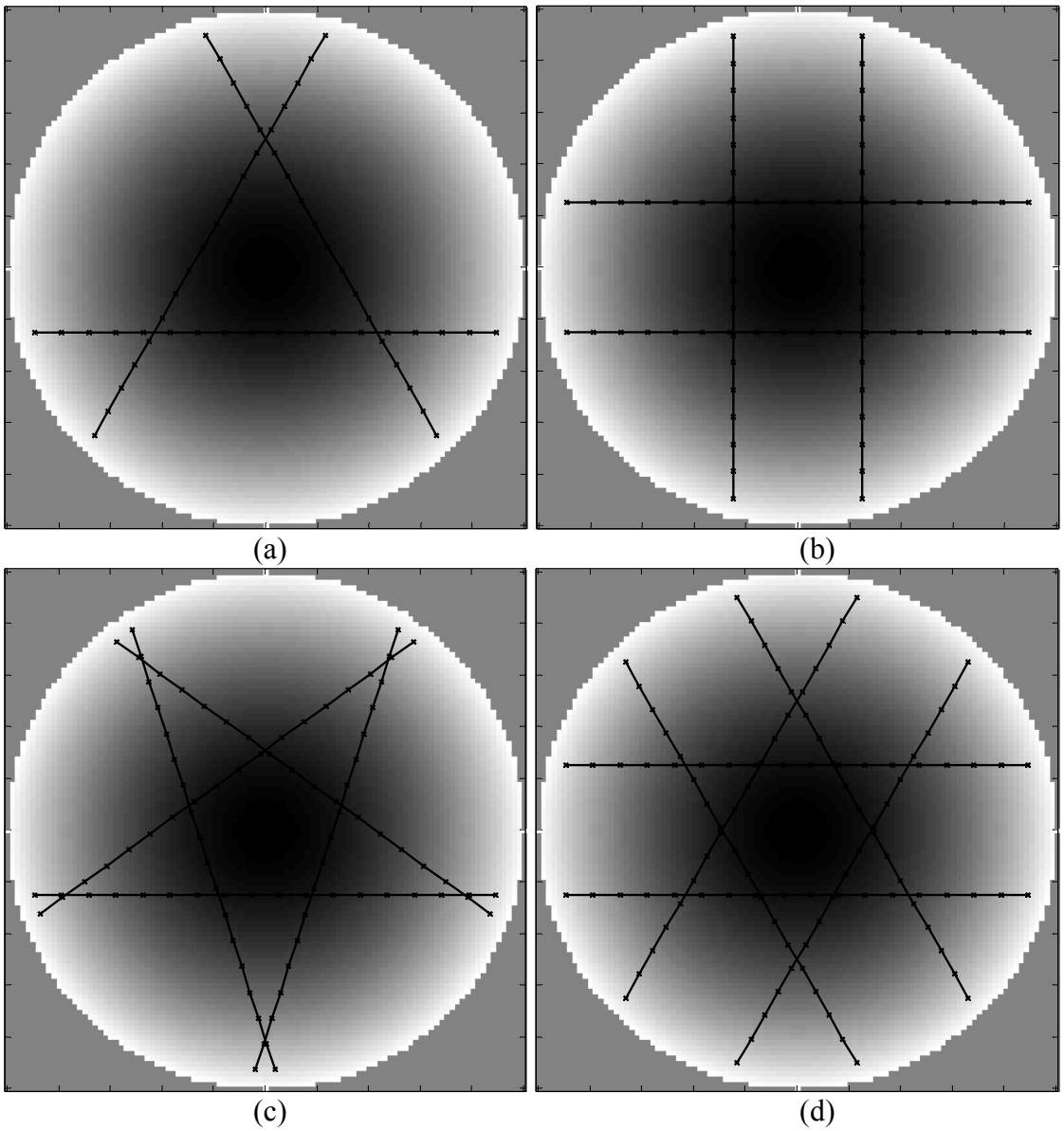

FIGURE B.11. Scanning pentaprism test examples – line scans (three, four, five, and six) are offset from the center of a 2 m mirror by 250 mm. The line scans are spaced in angle such that the scans are symmetrical around the mirror.

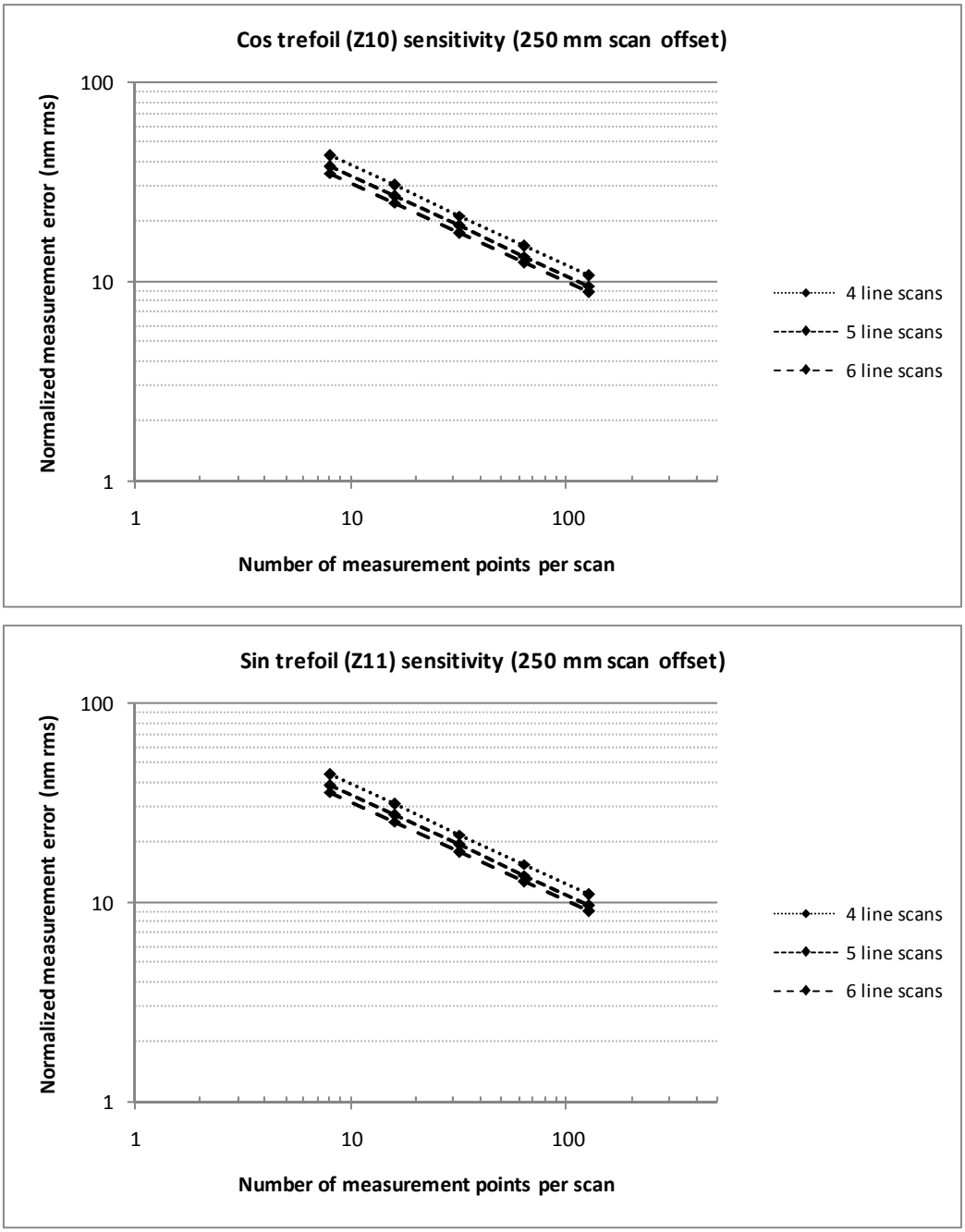

FIGURE B.12. Measurement noise normalized to 1 μrad rms coupling into trefoil (Z10, Z11) for number of line scans, number of measurement points, and d = 250 mm.

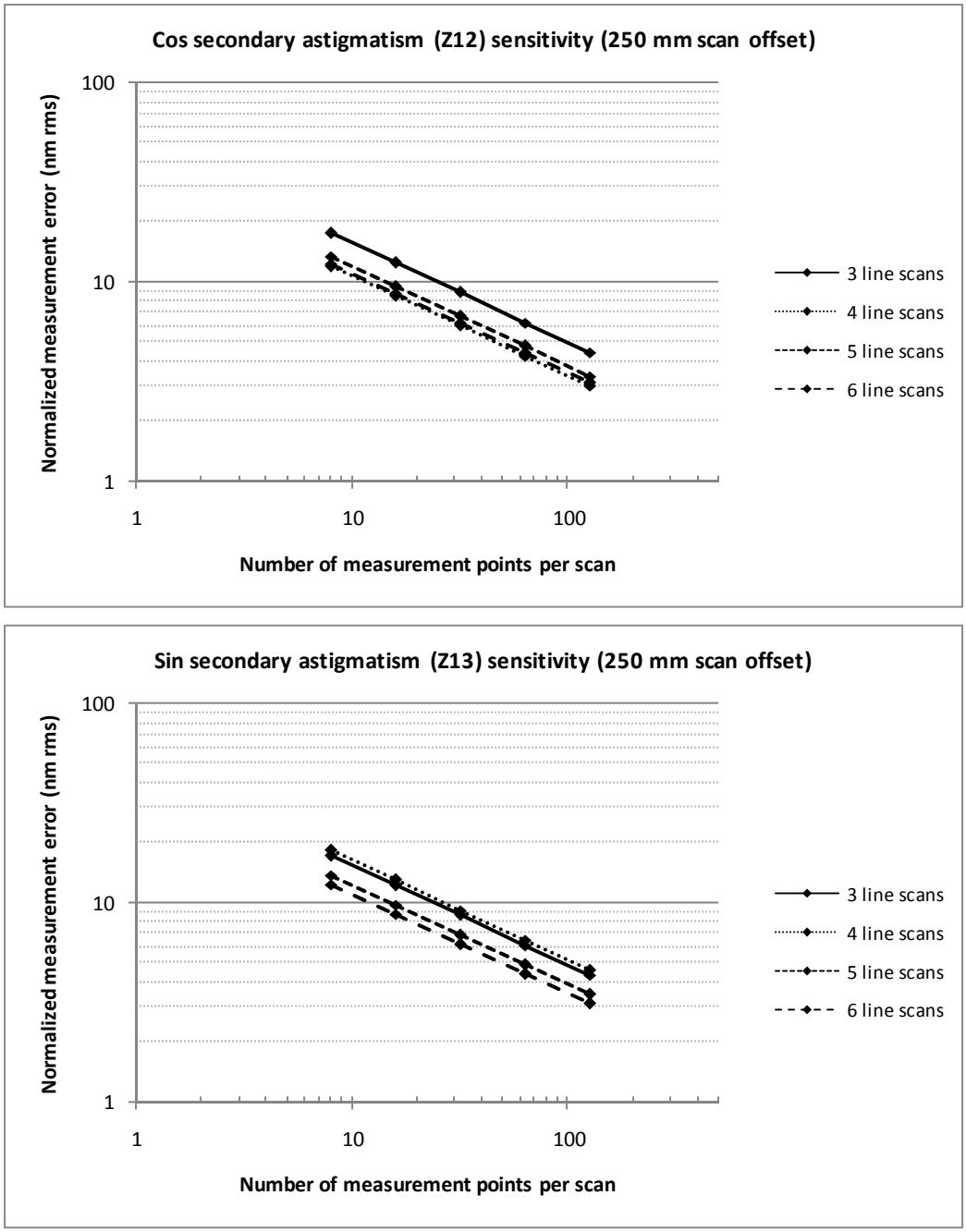

FIGURE B.13. Measurement noise normalized to 1 μrad rms coupling into secondary astigmatism (Z12, Z13) for number of line scans, number of measurement points, and d = 250 mm.

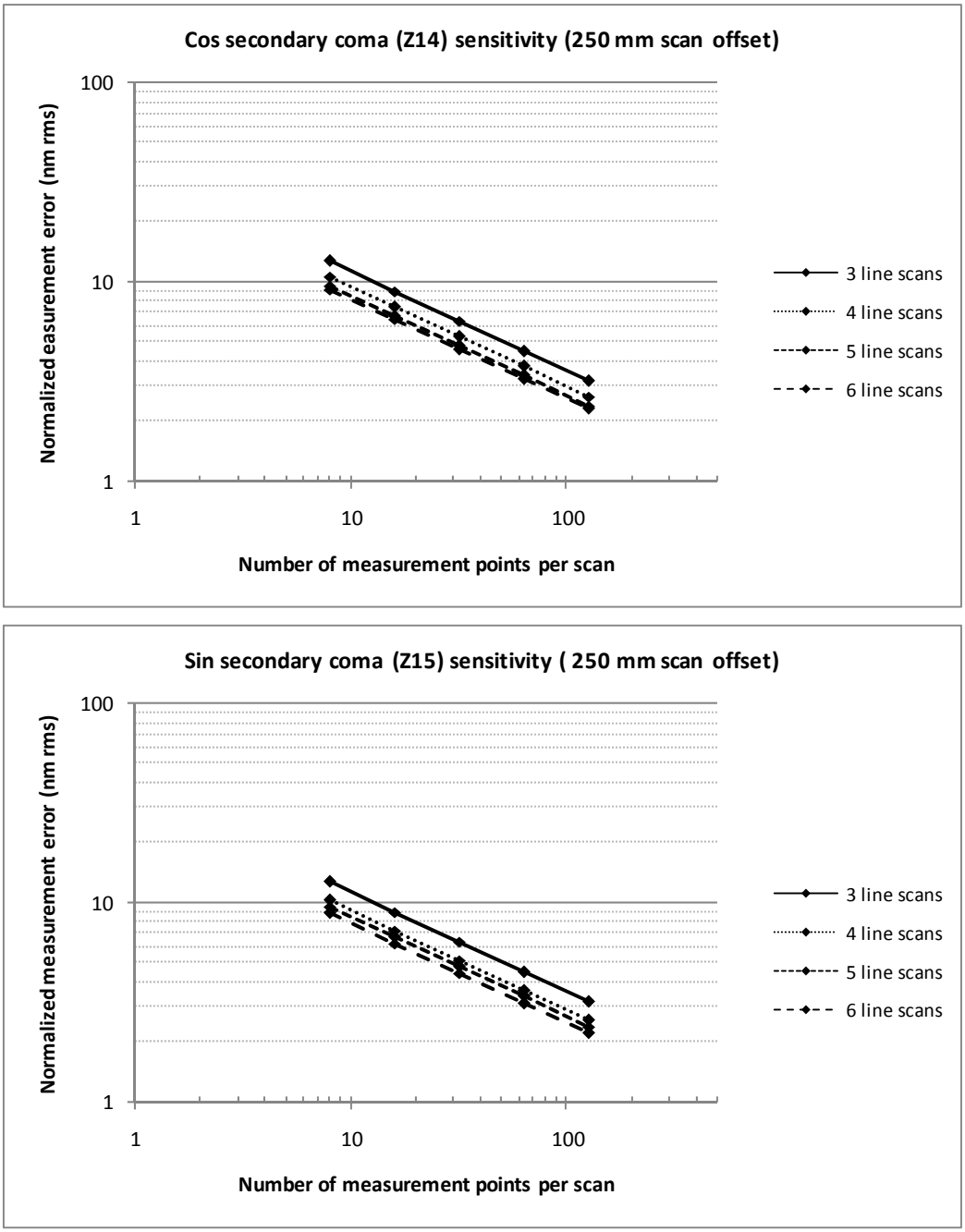

FIGURE B.14. Measurement noise normalized to 1 μrad rms coupling into secondary coma (Z14, Z15) for number of line scans, number of measurement points, and d = 250 mm.

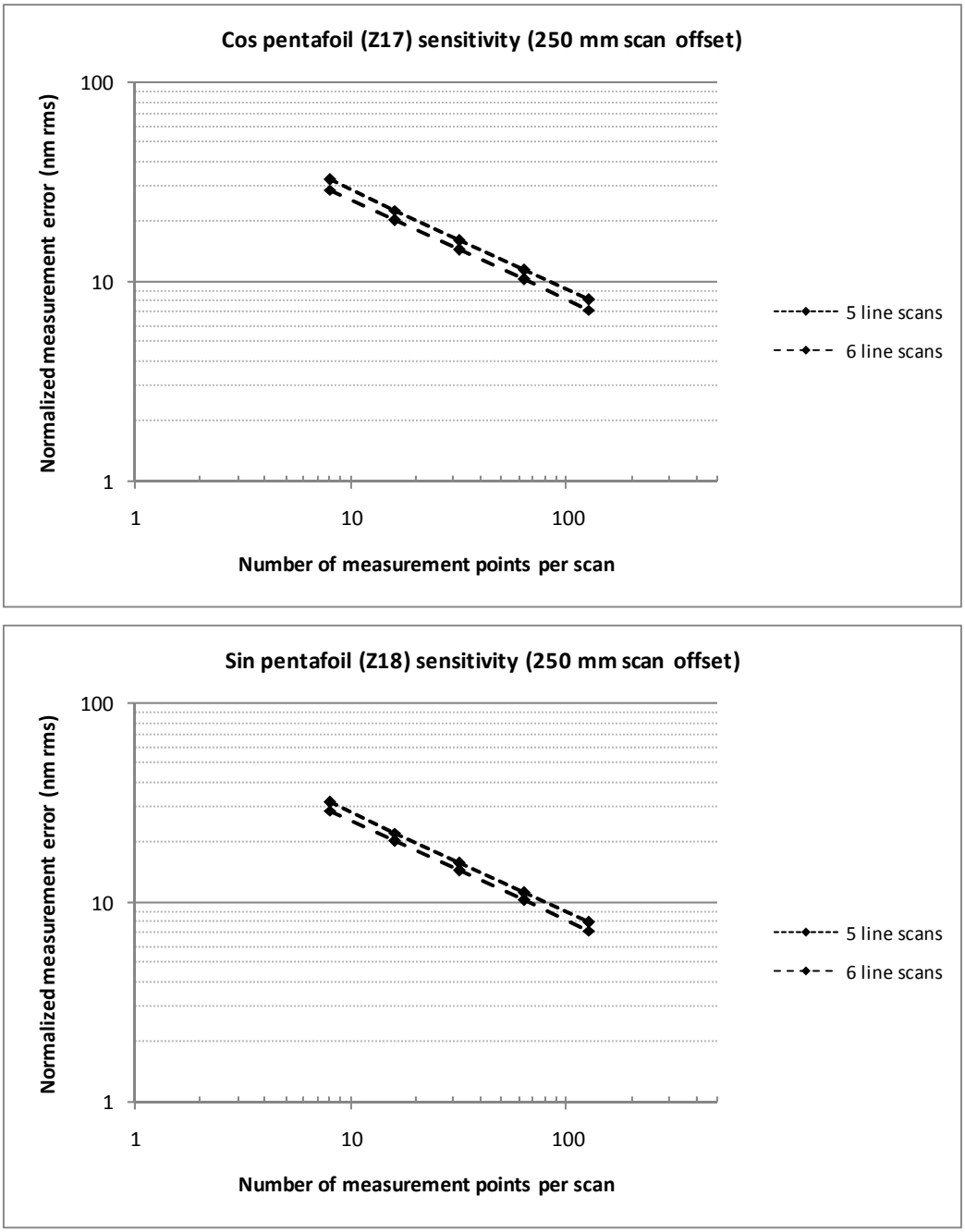

FIGURE B.15. Measurement noise normalized to 1 μrad rms coupling into pentafoil or 4θ (Z17, Z18) for number of line scans, number of measurement points, and d = 250 mm.

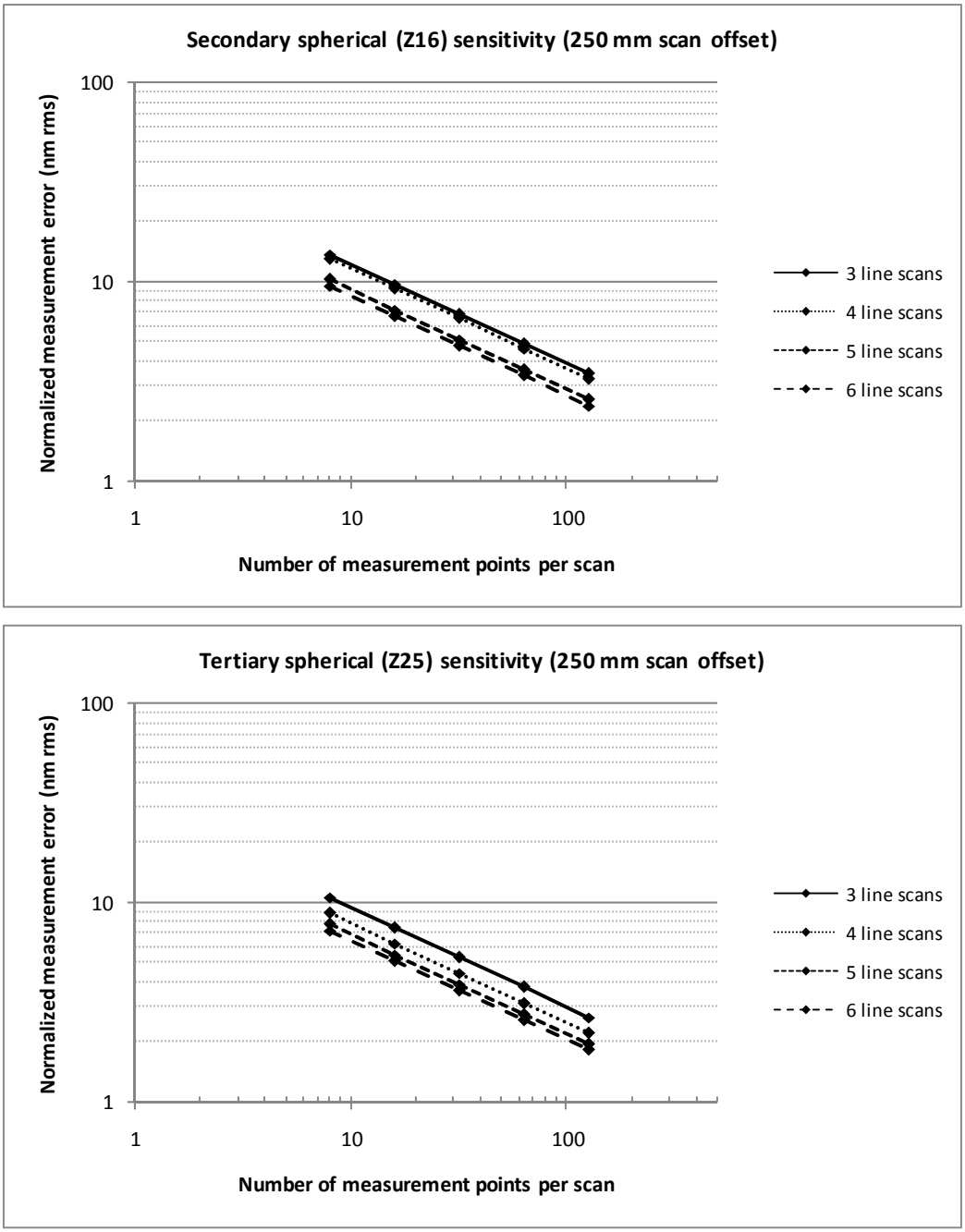

FIGURE B.16. Measurement noise normalized to 1 μrad rms coupling into secondary and tertiary spherical (Z16, Z25) for number of line scans, number of measurement points, and d = 250 mm.

The proceeding plots are for the case when the line scans offsets was 500 mm as shown in Figure B.17. The amounts of measurement error due to measurement noise are plotted against the number of measurement points (for each number of line scans). A function of the form $AN^{-1/2}$ was fitted to the data points, where *A* coefficient is the sensitivity to noise and *N* is the number of measurement points. Only the fitted functions are plotted to get all the number of line scans in a single plot.

Summary of the proceeding plots (Figures B.18 through B.22):

1. The analysis assumes measurement noise normalized to 1 μrad rms coupling into mid order Zernike aberrations for a 2 m flat mirror.
2. The line scans have 500 mm offset from the mirror center.
3. Sampling of trefoil (3θ) requires a minimum of four line scans.
4. Sampling of pentafoil (4θ) requires a minimum of five line scans.
5. The plots generally follow $AN^{-1/2}$ (Note: Except for small *N* due to under sampling).

TABLE B.3. Values of the *A* coefficient for the mid order Zernike aberrations for the case of the line scans with 500 mm offsets.

Line scans	Trefoil		Secondary astigmatism		Secondary coma		Pentafoil		Higher order spherical	
	Z10	Z11	Z12	Z13	Z14	Z15	Z17	Z18	Z16	Z25
3	--	--	103	97	65	65	--	--	49	38
4	90	88	59	35	35	32	--	--	46	32
5	91	91	44	45	37	36	95	93	37	28
6	128	55	50	48	28	27	100	97	32	25

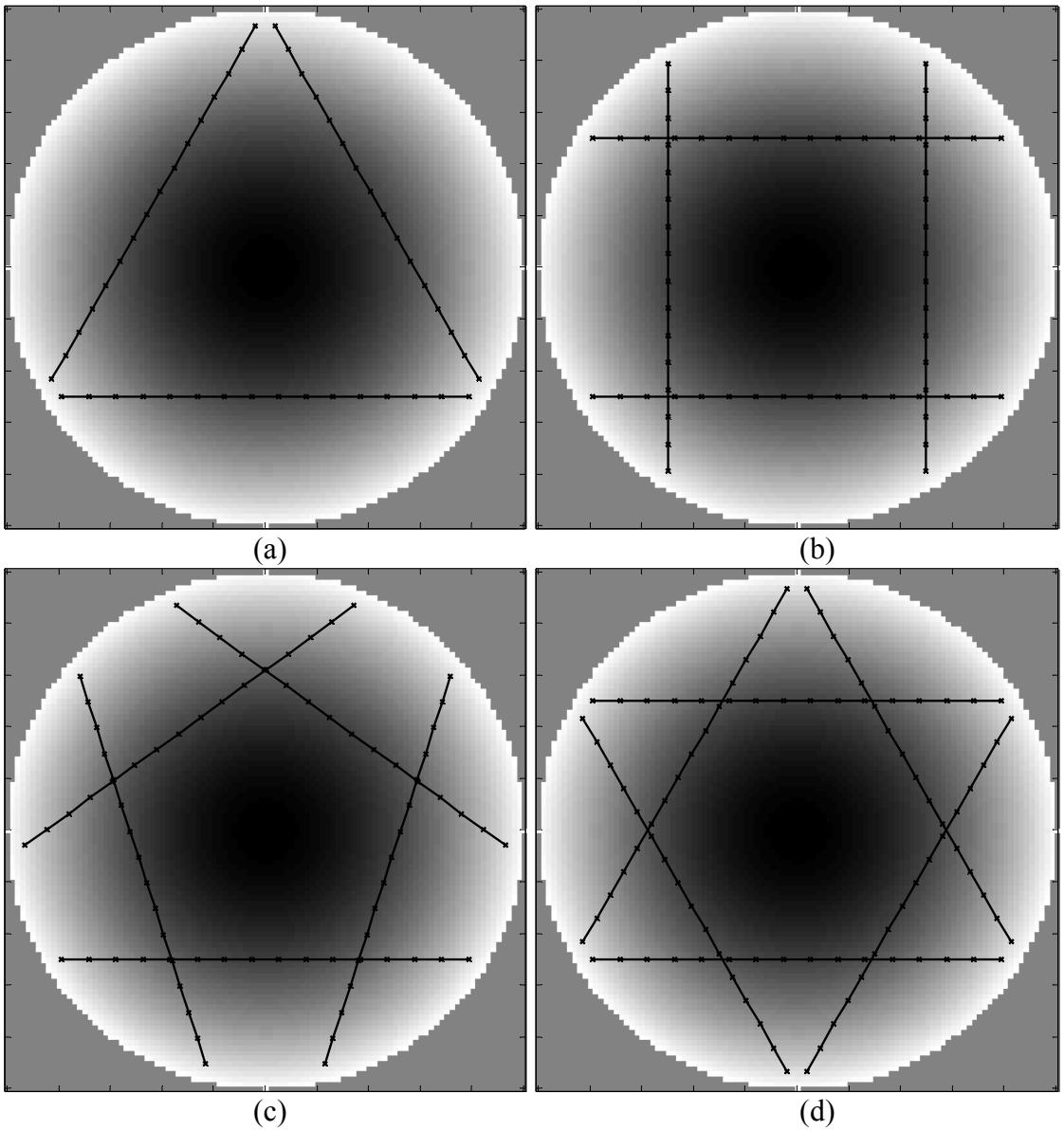

FIGURE B.17. Scanning pentaprism test examples – line scans (three, four, five, and six) are offset from the center of a 2 m mirror by 250 mm. The line scans are spaced in angle such that scans are symmetrical around the mirror.

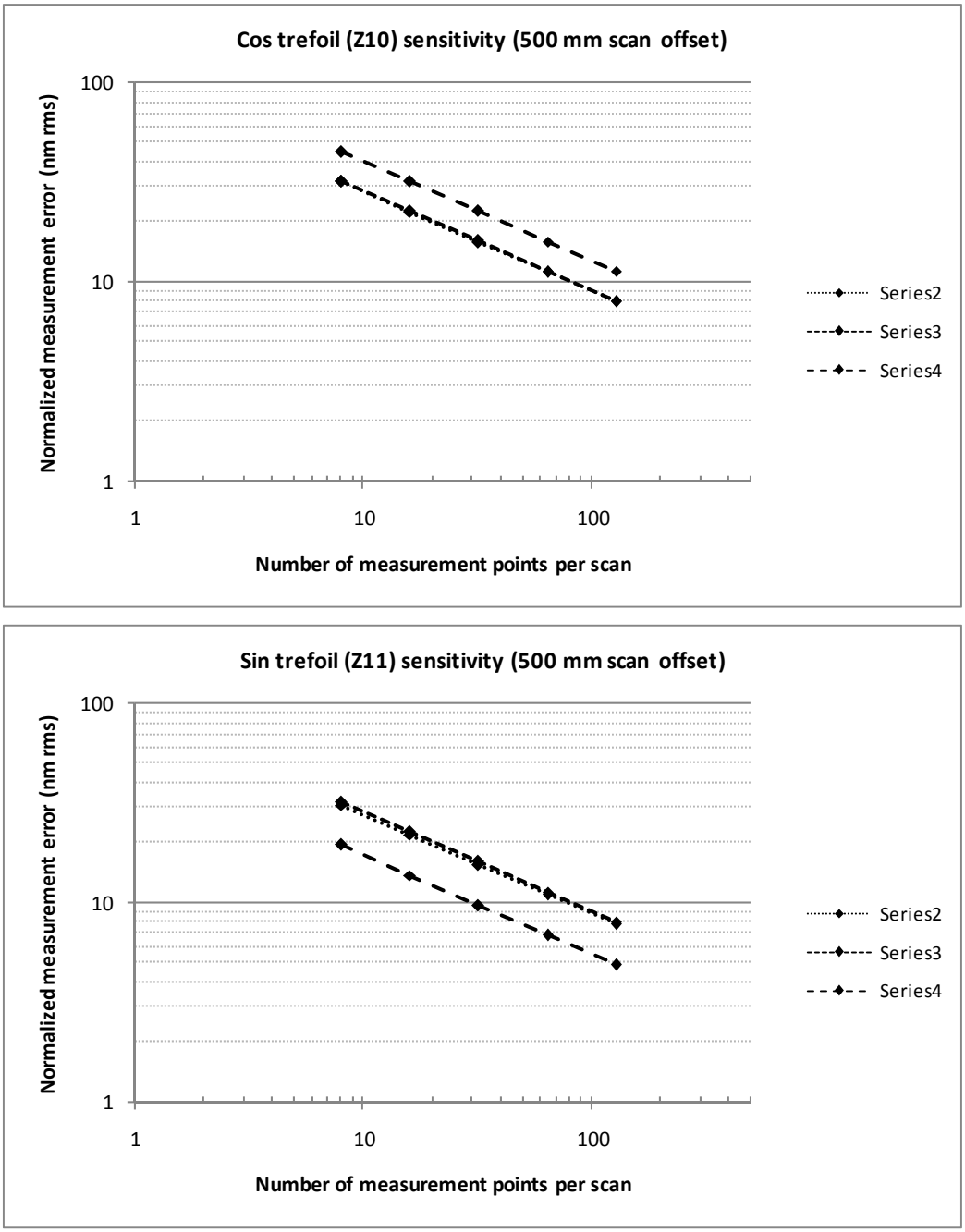

FIGURE B.18. Measurement noise normalized to 1 μrad rms coupling into trefoil (Z10, Z11) for number of line scans, number of measurement points, and d = 500 mm.

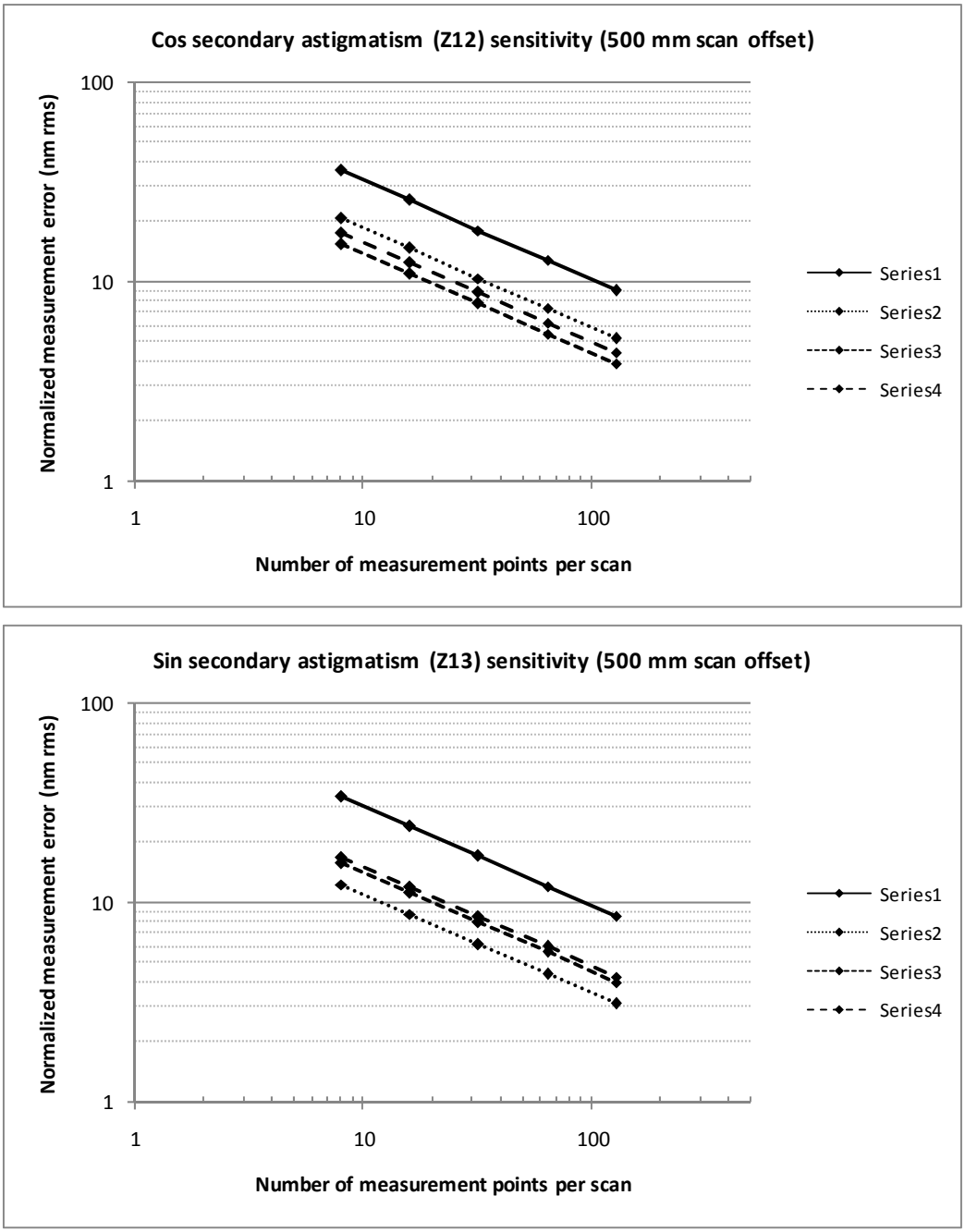

FIGURE B.19. Measurement noise normalized to 1 μrad rms coupling into secondary astigmatism (Z12, Z13) for number of line scans, number of measurement points, and d = 500 mm.

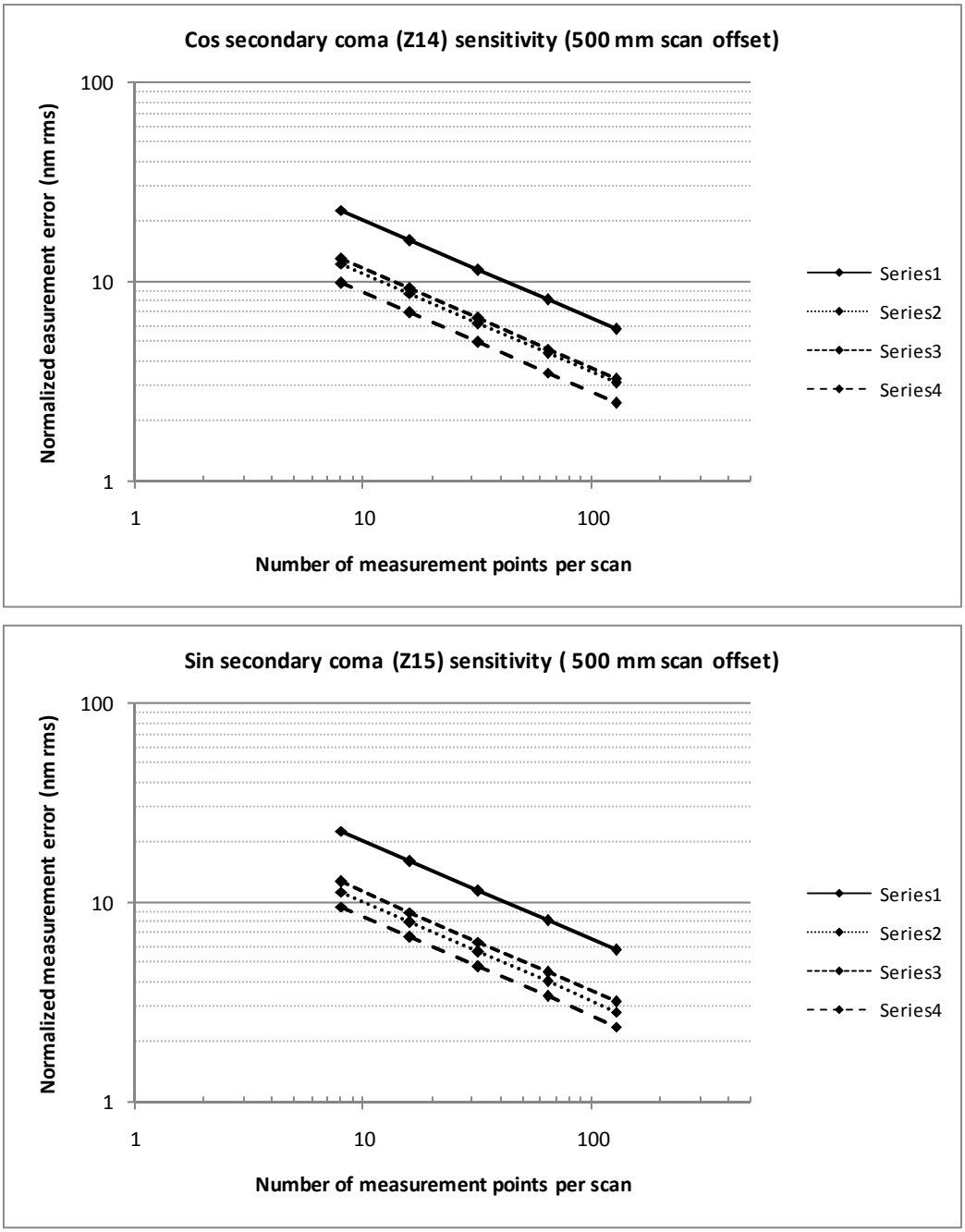

FIGURE B.20. Measurement noise normalized to 1 μrad rms coupling into secondary coma (Z14, Z15) for number of line scans, number of measurement points, and d = 500 mm.

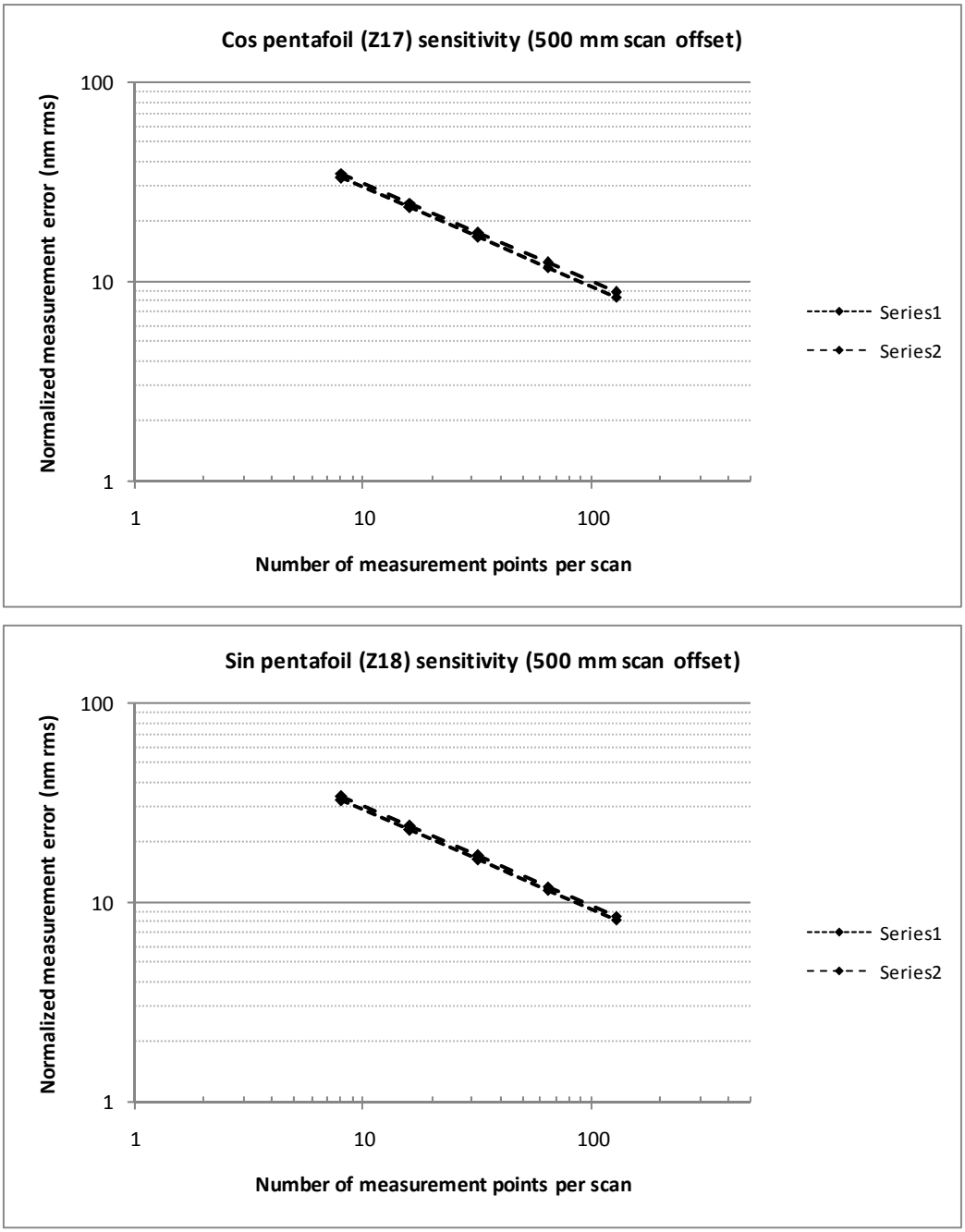

FIGURE B.21. Measurement noise normalized to 1 μrad rms coupling into pentafoil or 4θ (Z17, Z18) for number of line scans, number of measurement points, and d = 500 mm.

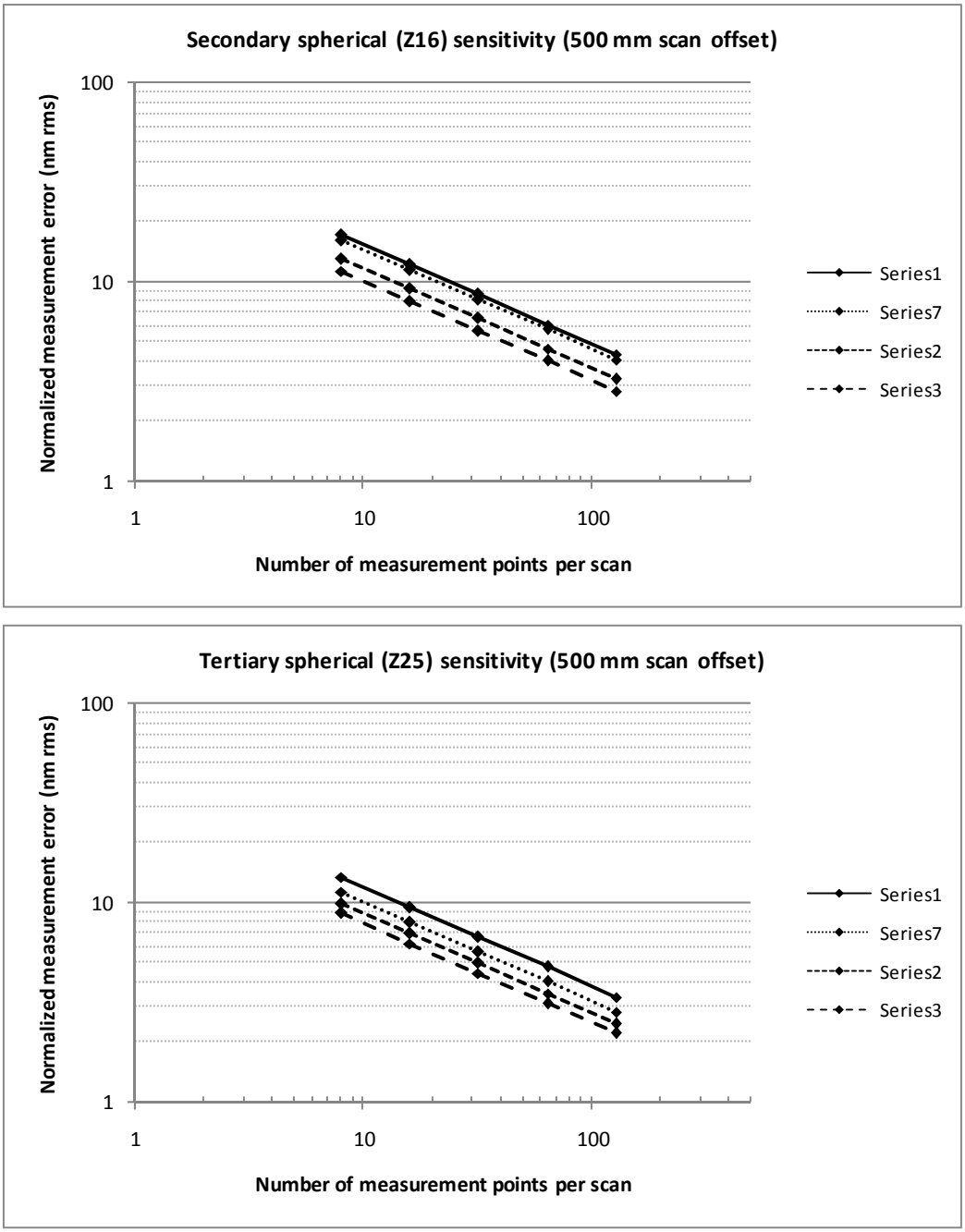

FIGURE B.22. Measurement noise normalized to 1 μrad rms coupling into secondary and tertiary spherical (Z16, Z25) for number of line scans, number of measurement points, and d = 500 mm.

The next set of plots shows the same data (measurement noise normalized to 1 μrad rms coupling into mid order Zernike aberrations), but plotted against the line scans distance from the center of the mirror or offset, *d*. The set of plots assumes 64 measurement points per line scan. The number of measurement points is maintained for each line scan with offset.

Summary of the proceeding plots (Figures B.23 through B.27):

1. The analysis assumes measurement noise normalized to 1 μrad rms coupling into mid order Zernike aberrations for a 2 m flat mirror.
2. The set of plots assumes 64 measurement points per line scan.
3. The behaviors of the measurement errors are mixed; some aberrations get sampled better with increasing line scan offsets, while others do not.
4. For some aberrations their trends are also mixed (e.g. secondary astigmatism).
5. Due to mixed behaviors, some aberrations get sampled better with a combination of the number of line scans and line scan offsets. For example, pentafoil is sampled well with six line scans and 250 mm line scan offset.

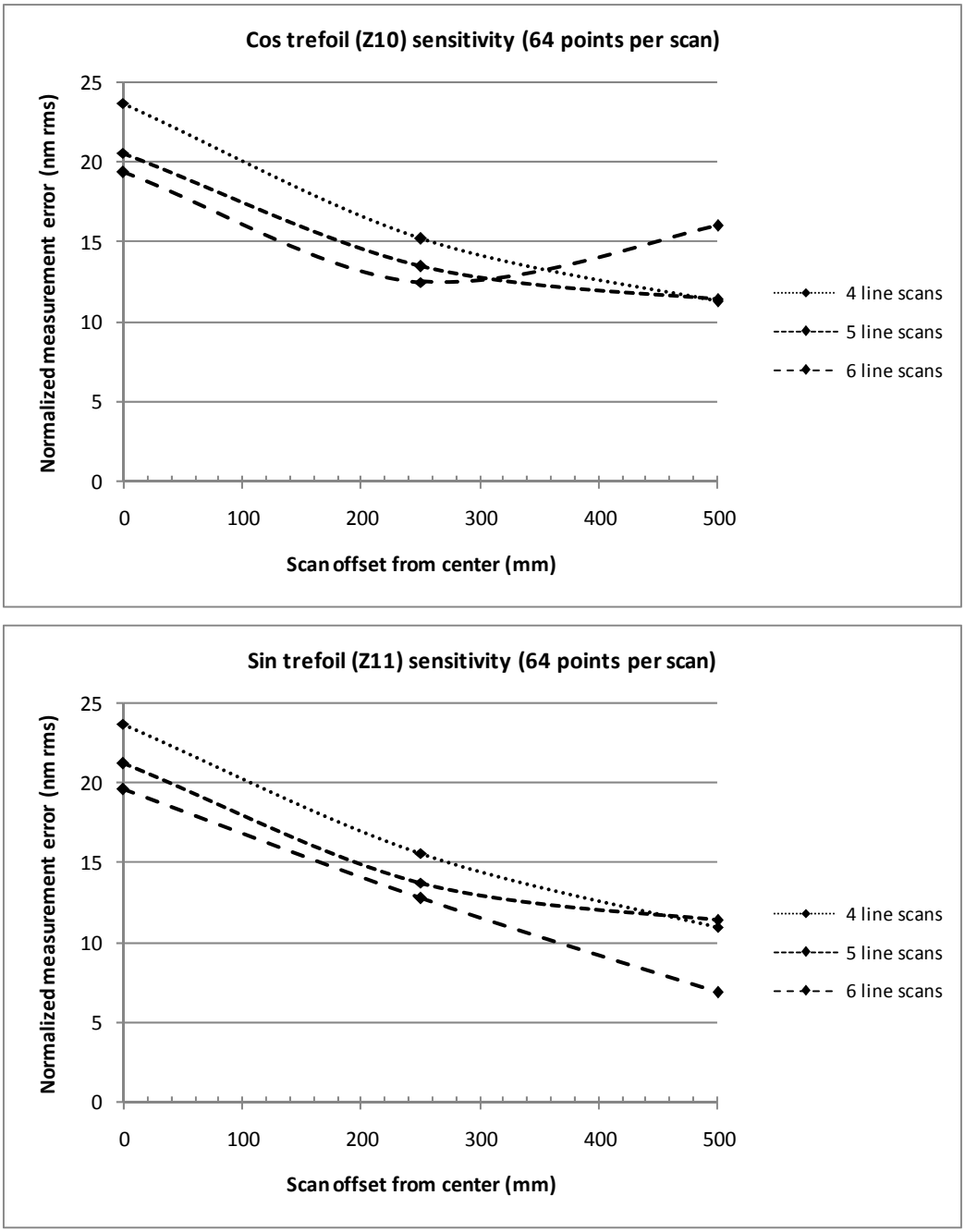

FIGURE B.23. Measurement noise normalized to 1 μrad rms coupling into trefoil (Z10, Z11) for number of line scans and 64 measurement points.

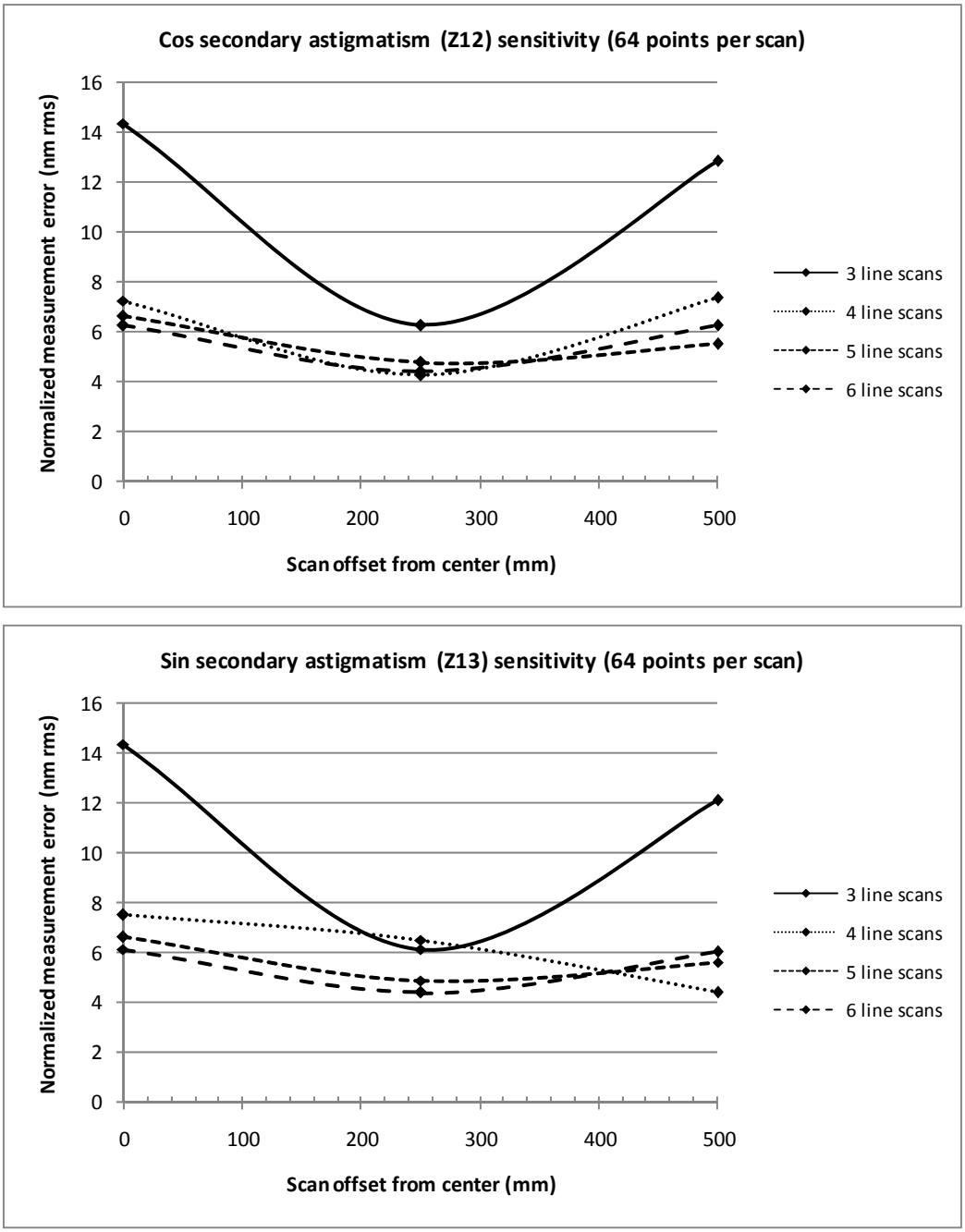

FIGURE B.24. Measurement noise normalized to 1 μrad rms coupling into secondary astigmatism (Z12, Z13) for number of line scans and 64 measurement points.

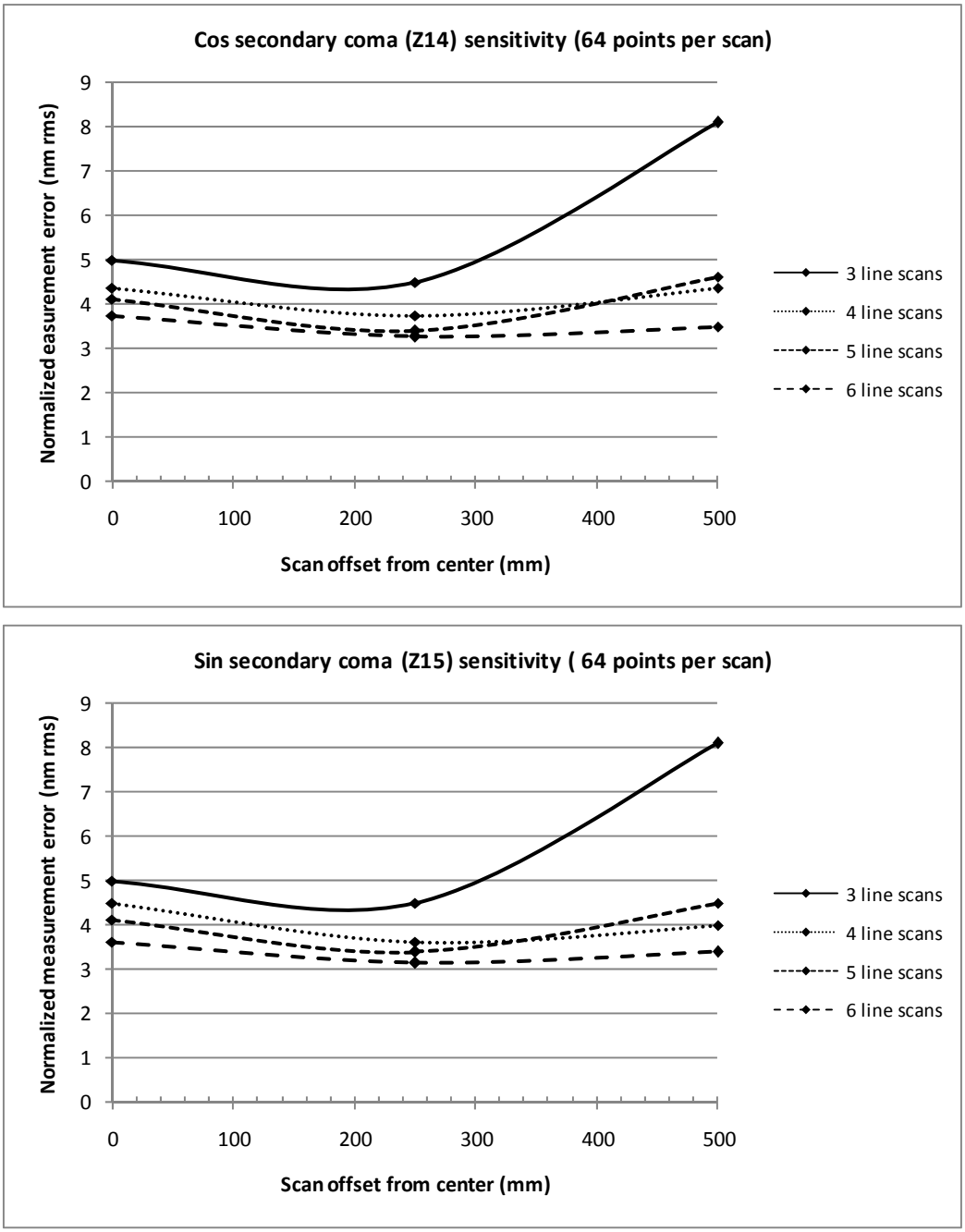

FIGURE B.25. Measurement noise normalized to 1 μrad rms coupling into secondary coma (Z14, Z15) for number of line scans and 64 measurement points.

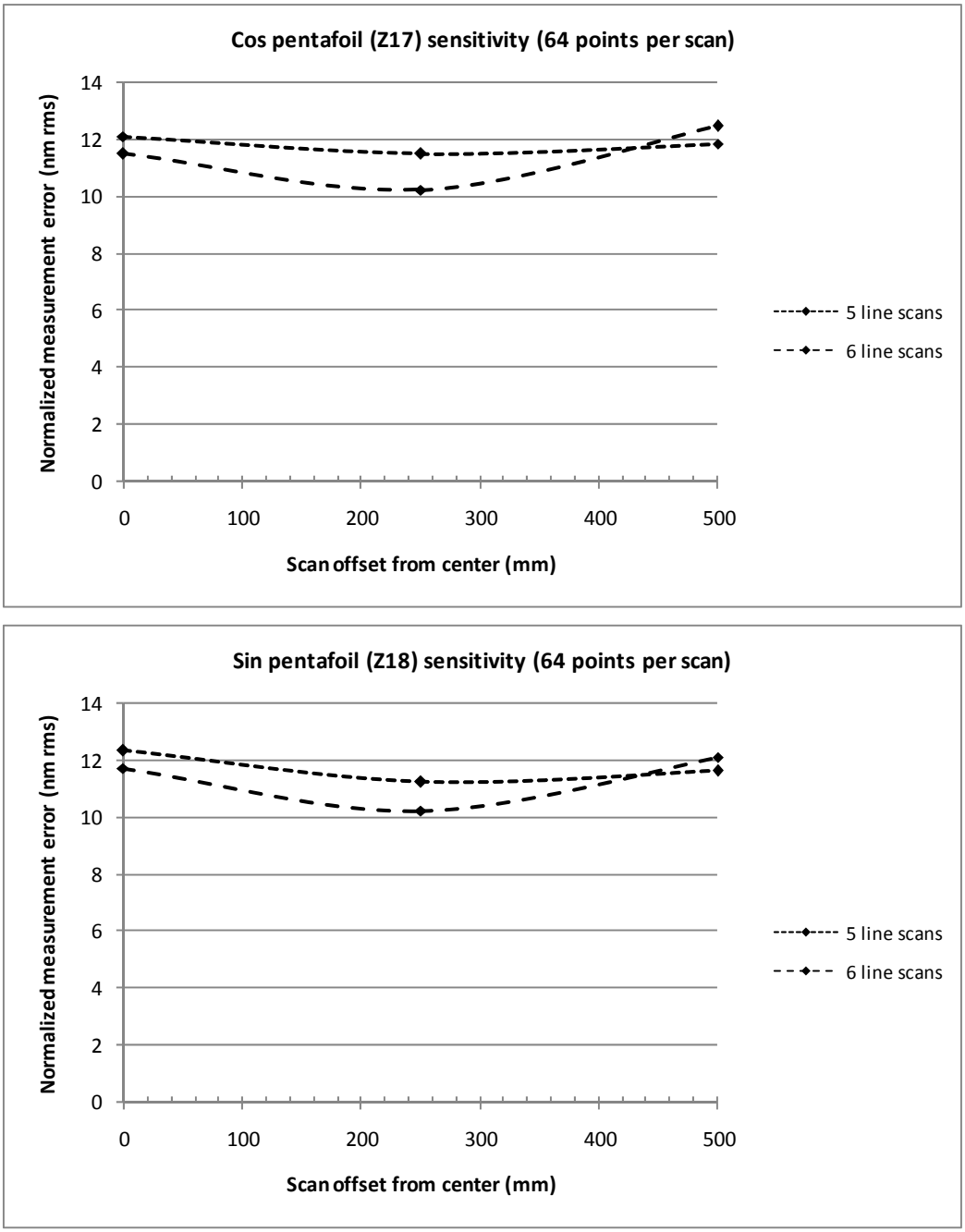

FIGURE B.26. Measurement noise normalized to 1 μrad rms coupling into pentafoil or 4θ (Z17, Z18) for number of line scans and 64 measurement points.

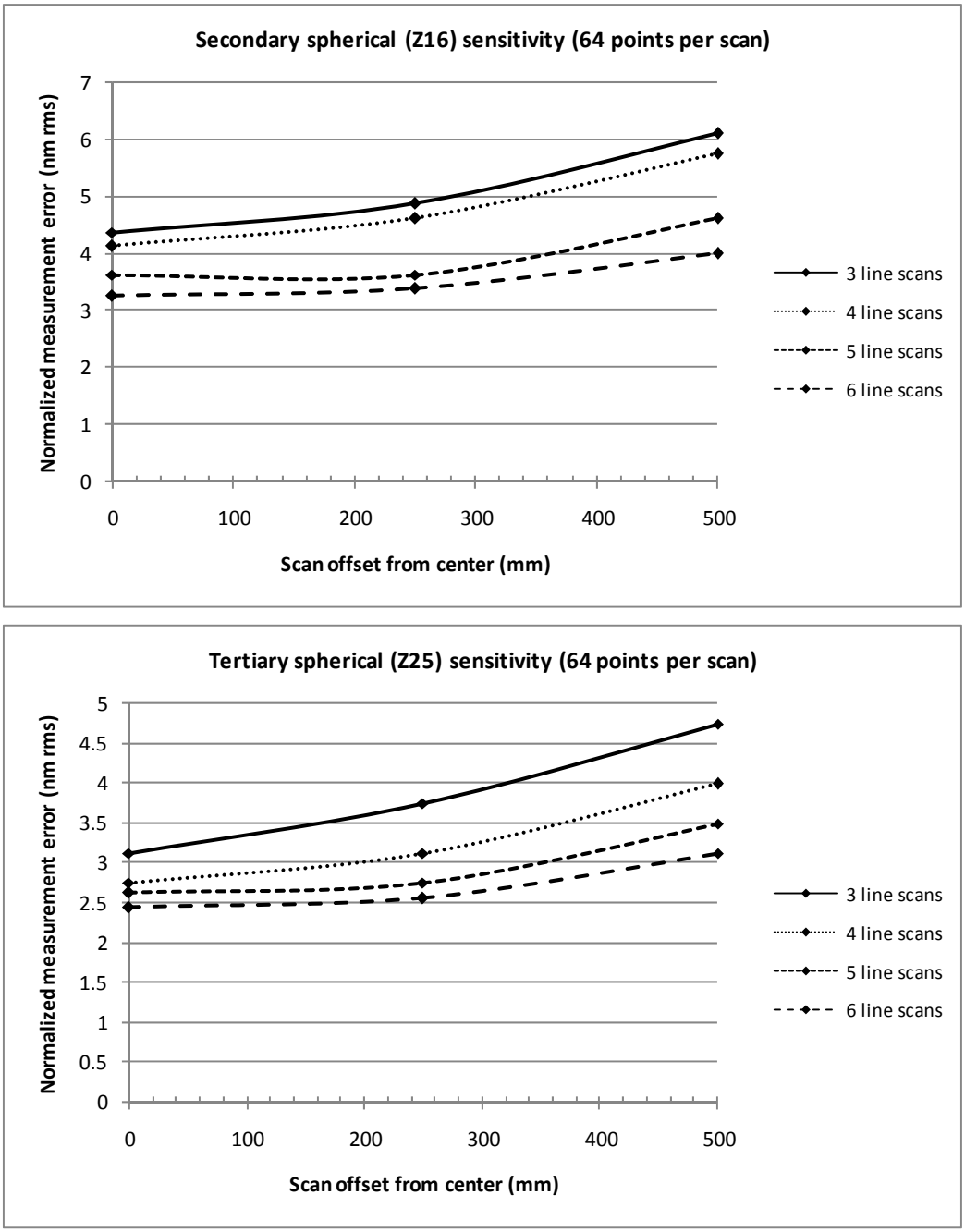

FIGURE B.27. Measurement noise normalized to 1 μrad rms coupling into secondary and tertiary spherical (Z16, Z25) for number of line scans and 64 measurement point per scan.

The next set of plots shows the same data (measurement noise normalized to 1 μrad rms coupling into mid order Zernike aberrations), but plotted against the number of line scans. The set of plots assumes 64 measurement points per scan. The number of measurement points is maintained for the line scans with offset.

Summary of the proceeding plots (Figures B.28 through B.32):

1. The analysis assumes measurement noise normalized to 1 μrad rms coupling into mid order Zernike aberrations for a 2 m flat mirror.
2. The set of plots assumes 64 measurement points per line scan.
3. The behavior of the measurement errors differ between the aberrations due to the ability of certain line scans with certain offsets to sample aberrations better. For example, secondary astigmatism and coma are sampled well with six line scans and 500 mm line scan offset, while secondary and tertiary spherical are sampled well with six line scans with no offset.

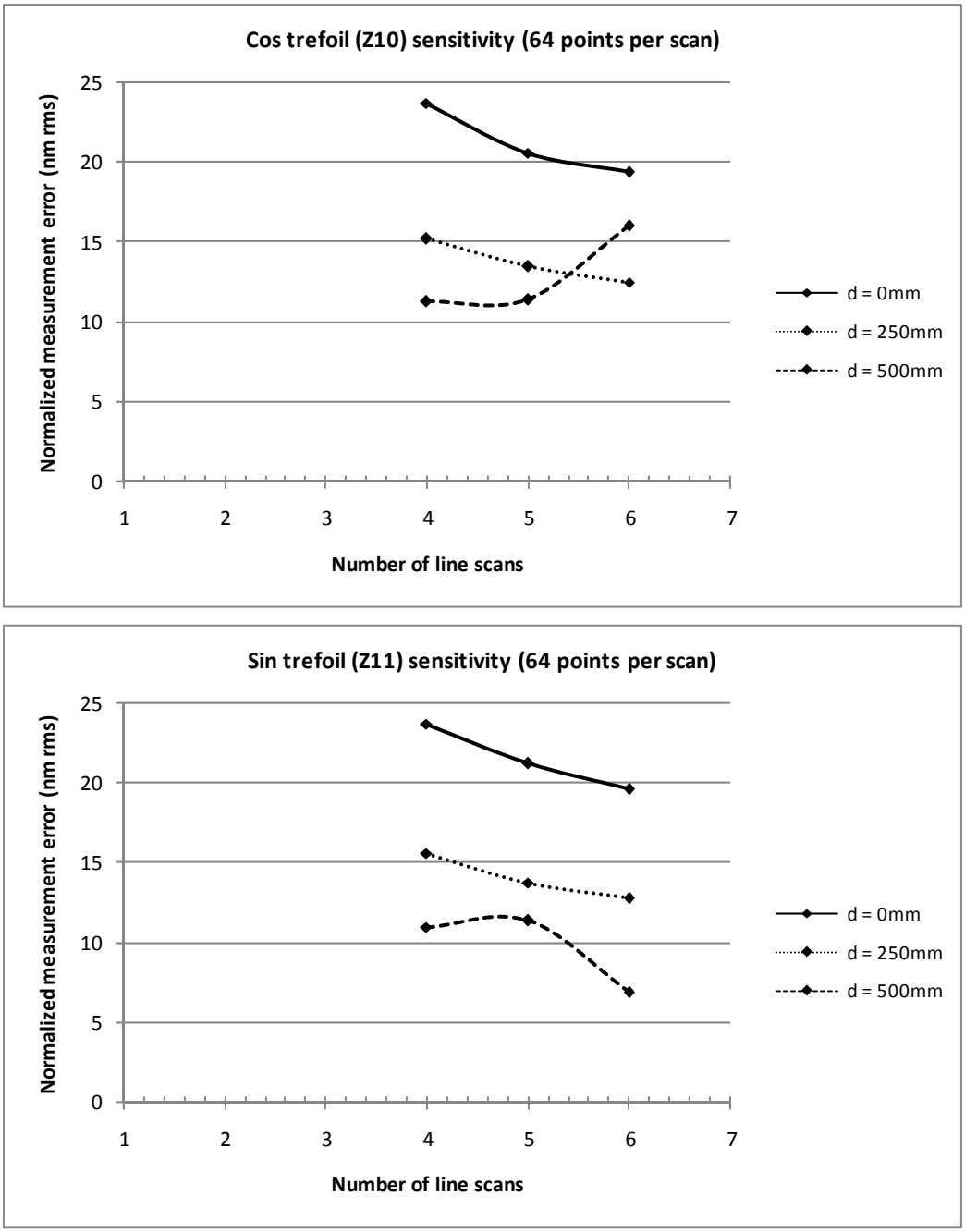

FIGURE B.28. Measurement noise normalized to 1 μrad rms coupling into trefoil (Z10, Z11) for number of line scans and 64 measurement points per scan.

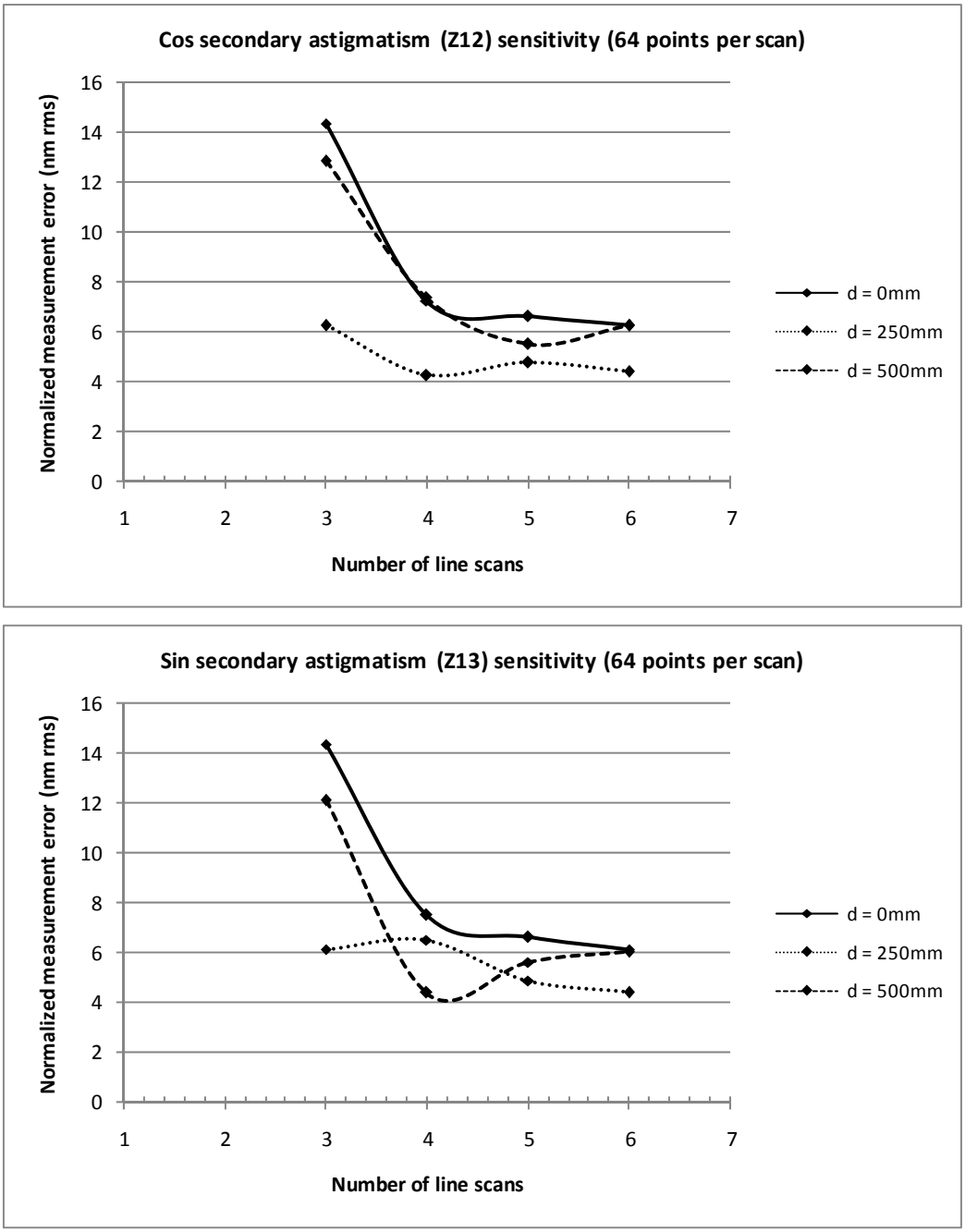

FIGURE B.29. Measurement noise normalized to 1 μrad rms coupling into secondary astigmatism (Z12, Z13) for number of line scans and 64 measurement points per scan.

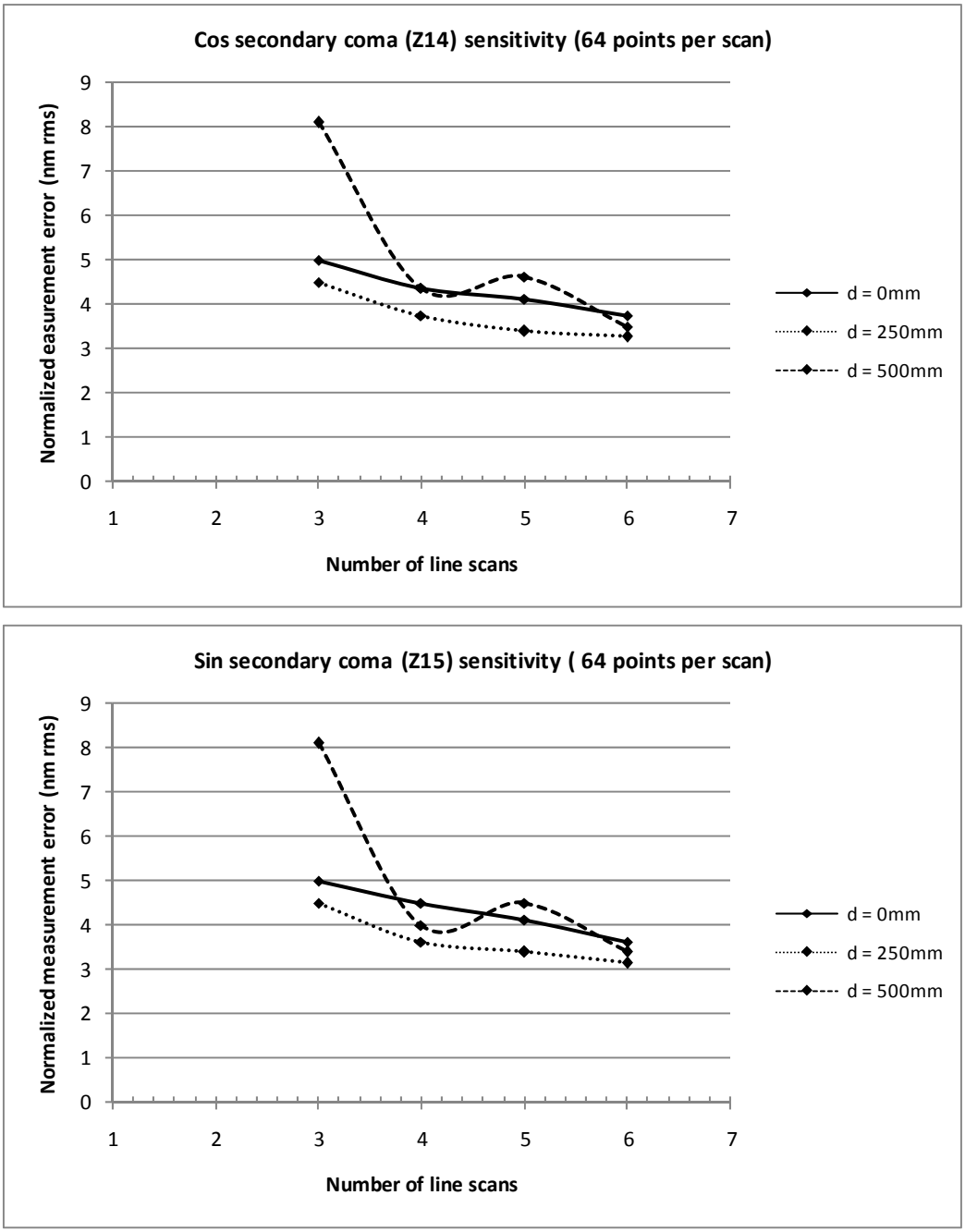

FIGURE B.30. Measurement noise normalized to 1 μrad rms coupling into secondary coma (Z14, Z15) for number of line scans and 64 measurement points per scan.

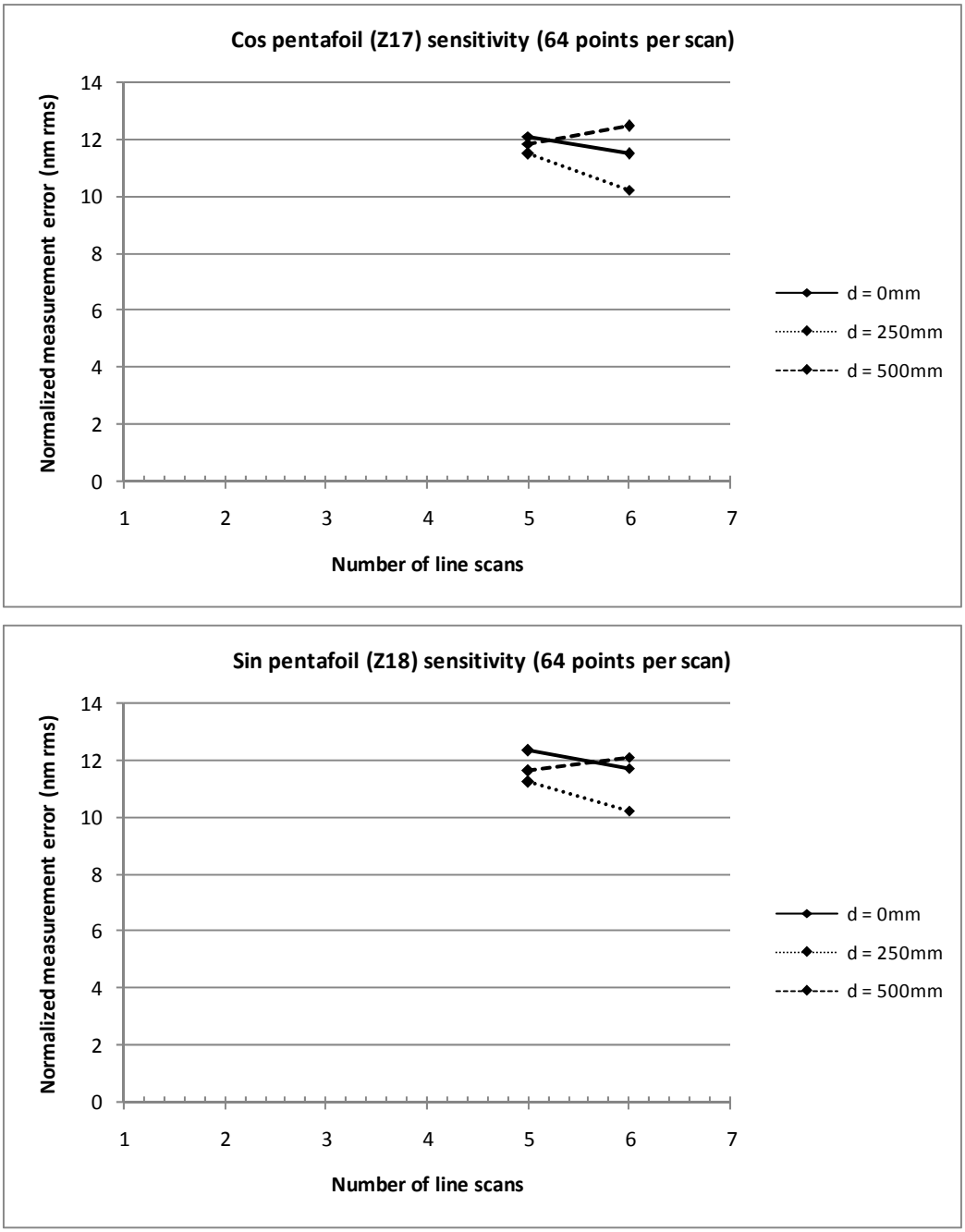

FIGURE B.31. Measurement noise normalized to 1 μrad rms coupling into pentafoil or 4θ(Z17, Z18) for number of line scans and 64 measurement points per scan.

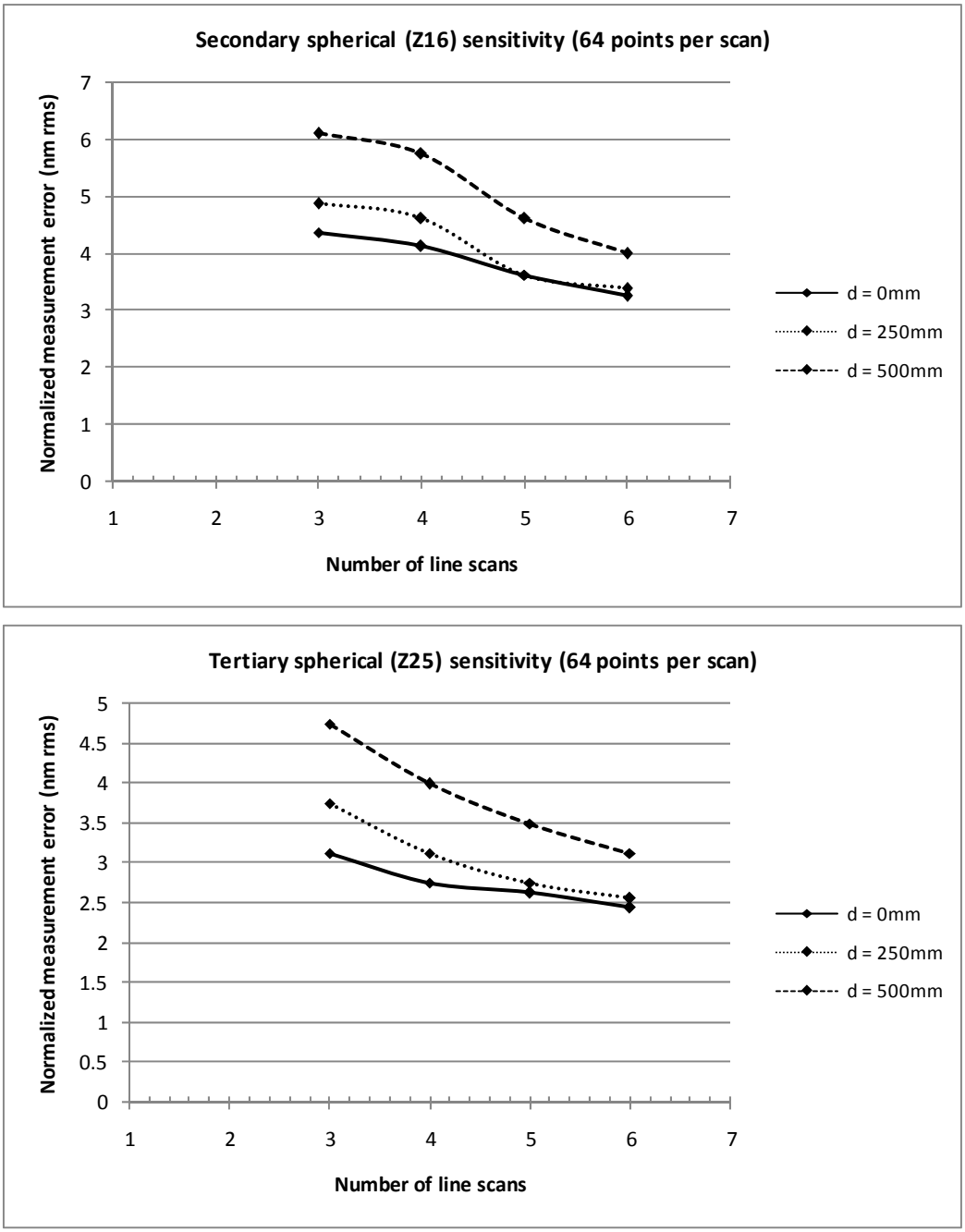

FIGURE B.32. Measurement noise normalized to 1 μrad rms coupling into secondary and tertiary spherical (Z16, Z25) for number of line scans and 64 measurement points per scan.

REFERENCES

[1] J. W. Mayo, III, "Problem areas in large optics fabrication – a project manager's perspective," Proc. SPIE **542**, 1 (1985).

[2] G. Bilie, M. Weijun, "The experiment of Φ1m annular continuous polisher (ACP) for LAMOST ultrathin hexagonal flat," Proc. SPIE **3785**, 94 (1999).

[3] L. V. Bourimborde, A. Tonso, L. M. Zerbino, M. Garavaglaia, "Optical interference studies of a confined liquid free surface: meniscus effect compensation and time evolution of the surface, Opt. Eng. **35** (1), 70 (1996).

[4] D. A. Ketelsen, D. S. Anderson, "Optical testing with large liquid flats," Proc. SPIE **966**, 365 (1988).

[5] I. Powell, E. Goulet, "Absolute figure measurements with a liquid-flat reference," App. Opt. **37** (13), 2579 (1998).

[6] P. C. V. Mallik, J. Burge, C. Zhao, R. Siebel, "Measurement of glass and liquid flats using a pentaprism scanning system," in Frontiers in Optics OSA Technical Digest Series (Optical Society of America, 2005).

[7] J. Hudman, Analysis of an off-axis null corrector and characterization of a 1 meter liquid flat, Unpublished master's thesis, University of Arizona, Tucson, Arizona (2005).

[8] W. P. McCray, Giant telescopes: astronomical ambition and the promise of technology, Cambridge, Massachusetts: Harvard University Press (2004).

[9] P. Y. Bely, The design and construction of large optical telescopes, New York: Springer (2003).

[10] D. Anderson, J. Burge, "Optical fabrication," in *Handbook of optical engineering*, D. Malacara , Ed., New York: Mercel Dekkar (2001), pp. 915-955.

[11] H. H. Karow, Fabrication Methods for Precision Optics, New York: Wiley-Interscience (1993).

[12] L. Stepp, et al., "Enabling a giant segmented mirror telescope for the astronomical community, Ch. 5 Technical studies, Section 5.4: cost effective mirror fabrication" http://www.aura-nio.noao.edu/book/ch5/5_4.html.

[13] F. Cooke, N. Brown, E. Prochnow, "Annular lapping of precision optical flatware," Opt. Eng. **15** (5), 407 (1976).

[14] Goodrich Corporation, http://www.oss.goodrich.com.

[15] M. V. Mantravadi, “Newton, Fizeau, and Haidinger interferometers,” in *Optical Shop Testing*, D. Malacara, Ed. (Wiley, 1992), pp. 1-49.

[16] J. Wyant, “Testing flat surface optical components,” optical testing class notes, Tucson, Arizona, University of Arizona, College of Optical Sciences (2004).

[17] C. Zhao, R. Sprowl, M. Bray, J. H. Burge, "Figure Measurements of a Large Optical Flat With a Fizeau Interferometer and Stitching Technique," Proc. SPIE **6293,** 62930K (2006).

[18] P. Murphy, J. Fleig, G. Forbes, D. Miladinovic, G. DeVries, S. O’Donohue, “Subaperture stitching interferometry for testing mild aspheres,” Proc. SPIE **6293**, 62930J (2006).

[19] S. Chen, S. Li, Y. Dai, “An efficient iterative algorigthm for subaperture stitching interferometry for aspheric surface,” Proc. SPIE **6024**, 60241E (2006).

[20] B. E. Catanzaro, J. A. Thomas, E. J. Cohen, “Comparison of full-aperture interferometry to subaperture stitched interferometry for a large-diameter fast mirror,” Proc. SPIE **4444**, 224 (2001).

[21] J. Ojeda-Castaneda, “Foucault, wire, and phase modulation tests” in *Optical shop testing*, D. Malacara, Ed. (Wiley, 1992), pp. 265-320.

[22] J. H. Burge, “Measurement of coma in a large flat mirror using the skip-flat test,” Tucson, Arizona, University of Arizona, College of Optical Sciences (2002).

[23] J. Drescher, “Analytical estimation of measurement uncertainty in surface plate calibration by the Moody method using differential levels,” Precision Engineering **27**, 323 (2003).

[24] B. Acko, “Calibration of electronic levels using a special sine bar,” Precision Engineering **29**, 48 (2004).

[25] Wyler AG, http://www.wylerag.com.

[26] Mathworks, “Matlab and simulink for technical computing,” http://www.mathworks.com.

[27] P. Mallik, C. Zhao, J. H. Burge, “Measurement of a 2-m flat using a pentaprism scanning system,” Opt. Eng. **46**, 023602 (2007).

[28] P. Mallik, C. Zhao, J. H. Burge, “Measurement of a 2-m flat using a pentaprism scanning system,” Proc. SPIE **5869**, 58691A (2005).

[29] J. Burge, Advanced techniques for measuring primary mirrors for astronomical telescopes, unpublished doctoral dissertation, University of Arizona, Tucson, Arizona (1993).

[30] H. Martin, J. Burge, J. Kingsley, L. Kot, T. Zobrist, "Verification tests for the GMT primary mirror segments," Tucson, Arizona, University of Arizona, Steward Observatory Mirror Lab (2006).

[31] R. D. Geckeler, "ESAD shearing deflectometry: potential for synchrotron beamline metrology," Proc. SPIE **6317**, 63171H (2006).

[32] R. D. Geckeler, "Error minimization in high-accuracy scanning deflectometry," Proc. SPIE **6293**, 62930O (2006).

[33] R. D. Geckeler, "Optimal use of pentaprisms in highly accurate deflectometric scanning," Measurement Science and Technology **18**, 115-125 (2006).

[34] M. Wurm, R. D. Geckeler, "A novel method and a novel facility for ultra-precise 2D topography measurement of large optical surfaces," Proc. SPIE **5457**, 401 (2004).

[35] J. Illemann, A. Just, "Absolute deflectometric measurement of topography – influence of systematic deviations," Proc. SPIE **5457**, 689 (2004).

[36] J. Illemann, "Absolute high-accuracy deflectometric measurement of topography," Proc. SPIE **5188**, 308 (2003).

[37] M. Schulz, R. D. Geckeler, J. Illemann, "High accuracy form measurement of large optical surfaces," Proc. SPIE **5190**, 211 (2003).

[38] I. Weingartner, et al., "Novel concept for ultraprecise and fast measurement of the nanotopography of large wafers," Proc. SPIE **4779**, 13 (2002).

[39] I. Weingartner, M. Schultz, C. Elster, "Novel scanning technique for ultra-precise measurement of topography," Proc. SPIE **3782**, 306 (1999).

[40] M. Schulz, I. Weingartner, "Avoidance and elimination of errors in optical scanning," Proc. SPIE **3823**, 133 (1999).

[41] S. Qian, P. Takacs, G. Sostero, D. Cocco, "Portable long trace profiler: concept and solution," Review of Scientific Instruments **72** (8), 3198-3204 (2001).

[42] S. Qian, W. Jark, P. Z. Takacs, "The penta-prism LTP: a long-trace-profiler with stationary optical head and moving penta prism," Review of Scientific Instruments **66** (3), 2562-2569 (1995).

[43] H. Li, P. Z. Takacs, T. Oversluizen, "Vertical scanning long trace profiler: a tool for metrology of X-ray mirrors," Proc. SPIE **3152**, 180 (1997).

[44] Moller-Wedel-Optical, http://www.moeller-wedel-optical.com.

[45] UDT Instruments, http://www.udtinstruments.com.

[46] J. Yellowhair, J. H. Burge, "Measurement of optical flatness using electronic levels," Manuscript submitted to Opt. Eng. for publication (2007).

[47] J. Yellowhair, College of Optical Sciences, University of Arizona, 1630 East University Boulevard, Tucson, AZ 85721, R. Sprowl, P. Su, R. Stone, and J. H. Burge are preparing a manuscript to be called "Development of a 1-m vibration-insensitive Fizeau interferometer."

[48] N. Siegel, Algorithms for Data Registration and Subtraction in Optical Testing, Unpublished master's thesis, University of Arizona, Tucson, Arizona (2005).

[49] J. Yellowhair, College of Optical Sciences, University of Arizona, 1630 East University Boulevard, AZ 85721, R. Sprowl, P. Su, M. Valente, and J. H. Burge are preparing a manuscript to be called "Methodology for fabricating and testing high performance large flat mirrors."

[50] J. Yellowhair, J. H. Burge (accepted for publication), "Analysis of a scanning pentaprism system for measurements of large flat mirrors." App. Opt. (2007).

[51] B. F. Oreb, D. I. Farrant, C. J. Walsh, G. Forbes, and P. S. Fairman, "Calibration of a 300-mm-Aperture Phase-Shifting Fizeau Interferometer," Appl. Opt. **39**, 5161-5171 (2000).

[52] P. S. Fairman, et al., "300-mm-Aperture Phase-Shifting Fizeau Interferometer," Opt. Eng. **38**, 1371-1380 (1999).

[53] S. Han, "Laser Alignment for 610-mm Large Aperture Fizeau Interferometer," Proc. SPIE **3782**, 469 (1999).

[54] Engineering Synthesis Design, http://www.engsynthesis.com.

[55] C. Zhao, D. Kang, and J. H. Burge, "Effects of birefringence on Fizeau interferometry that uses a polarization phase-shifting technique," Appl. Opt. **44**, 7548-7553 (2005).

[56] P. Hariharan, "Interferometric testing of optical surfaces: absolute measurements of flatness," Opt. Eng. **36** (9), 2478-2481 (1997).

[57] P. Su, J. Burge, R. Sprowl, J. Sasian, "Maximum Likelihood Estimation as a General Method of Combining Sub-Aperture Data for Interferometric Testing," Proc. SPIE **6342,** 63421X (2006).

[58] P. Su, "Estimate accuracy of the flat by the maximum likelihood estimation method," Tucson, Arizona, University of Arizona, College of Optical Sciences (2006).

[59] D. Baiocchi, J. H. Burge, "Radius of Curvature Metrology for Segmented Mirrors," Proc. SPIE **4093**, 58 (2000).

[60] S. Song, Y. W. Lee, J. B. Song, I. W. Lee, H. S. Yang, Y. W. Choi, J. H. Jo, "Dual Testing of Large Aperture Optical System," Proc. SPIE **4778**, 227 (2002).

[61] C-H. Meng, J-H. Zhang, J. Shi, "Design and development of an interferometer with improved angular tolerance and its application to x-y theta measurement," Review of Scientific Instruments **71** (12), 4633 (2000).

[62] P. R. Yoder, Jr., W. W. Hollis, "Design of a compact wide aperture Fizeau interferometer," JOSA **47** (9), 858 (1957).

[63] J. S. Song, et al., "Dual testing of large aperture optical system," Proc. SPIE **4778**, 227 (2002).

[64] R. Bunnagel, H. A. Oehring, K. Steiner, "Fizeau interferometer for measuring the flatness of optical surfaces," Appl. Opt. **7** (2), 331-335 (2005).

[65] B. Kimbrough, J. Millerd, J. Wyant, J. Hayes, "Low coherence vibration insensitive Fizeau interferometer," Proc. SPIE **6292**, 62920F (2006).

[66] P. de Groot, "Phase-shift calibration errors in interferometers with spherical Fizeau cavities, Appl. Opt. **34** (16), 2856-2863 (1995).

[67] N. R. Sivakumar, B. Tan, K. Venkatakrishnan, "Determination of measurement uncertainty in the developed instantaneous phase shifting interferometer," Proc. SPIE **6342**, 63421W (2006).

[68] J. Schwider, et al., "Digital wavefront measuring interferometry: some systematic error sources," Appl. Opt. **22** (21), 3421-3432 (1983).

[69] M. Vannoni, G. Molesini, A. Righini, "Interferometric test of optical systems: effects of probe beam collimation errors," Opt. Eng. **44** (3), 035604 (2005).

[70] W. S. Wan Abdullah, J. N. Petzing, "Development of speckle shearing interferometer error analysis as an aperture function of wavefront divergence," J. of Mod. Opt. **52** (11), 1495-1510 (2005).

[71] J. R. Graham, Mirror manufacture, http://astro.berkeley.edu/~jrg/Polish/node1.html (2003).

[72] J. E. Nelson, J. Lubliner, T. S. Mast, "Telescope mirror supports: plate deflections on point supports," SPIE **322**, 212 (1982).

[73] P. R. Yoder, "Opto-Mechanical Systems Design," Dekker (1986).

[74] B. Cuerden, "Analysis of surface errors caused by mounting," Tucson, Arizona, University of Arizona, Steward Observatory Mirror Lab (2003).

[75] B. Cuerden, "DCT Primary – five and six ring support patterns," Tucson, Arizona, University of Arizona, Steward Observatory Mirror Lab (2006).

[76] B. Ceurden, J. Burge, S. Hvisc, "DCT primary polishing support, draft 5," Tucson, Arizona, University of Arizona, Steward Observatory Mirror Lab (2007).

[77] C. Kiikka, et al., "The JWST infrared scanning Shack-Hartman system: a new in-process way to measure large mirrors during optical fabrication at Tinsley," Proc. SPIE **6265**, 62653D (2002).

[78] P. C. Chen, et al., "Advanced in very lightweight composite mirror technology," Opt. Eng. **39** (9), 2320 (2000).

[79] J. H. Burge, "Simulation and optimization for a computer-controlled large-tool polisher," in *Optical Fabrication and Testing*, OSA Technical Digest **12**, 43 (1998).

[80] R. A. Jones, W. J. Rupp, "Rapid optical fabrication with computer-controlled optical surfaces, Opt. Eng. **30** (12), (1991).

[81] Y. Shi-jie, "Computer-aided zonal figuring of aspherical surface," Proc. SPIE **1236**, 706 (1990).

[82] M. H. Krim, "Design of a manufacturing facility for 8 to 10-m class mirrors," Proc. SPIE **1236**, 748 (1990).

[83] T. Wilson, V. Genberg, "Enabling advanced mirror blank design through modern optical fabrication technology," Proc. SPIE **1994**, 183 (1994).

[84] P. Dierickx, "Optical fabrication in the large," Workshop on Extremely Large Telescopes, Backaskog, Sweden, (1999).

[85] J. Lambropoulos, S. Xu, T. Feng, "Loose abrasive lapping hardness of optical glasses and its interpretation," App. Opt. **36** (7), 1501 (1997).

[86] F. Preston, "The theory and design of plate glass polishing machines," J. of the Society of Glass Technology 11, pp. 214-256 (1927).

[87] D. Malacara, Optical shop testing, 2nd ed., New York: Wiley-Interscience (1992).

[88] E. Friedman, J. L. Miller, Photonics rules of thumb – optics, electro-optics, fiber optics, and lasers, 2nd ed., Bellingham, WA: SPIE Press – McGraw-Hill (2003).

[89] M. Born, E. Wolf, Principles of Optics: theory of propagation, interference and diffraction of light, 6th ed., New York: Cambridge University Press (1997).

[90] J. Yellowhair, Unpublished test reports, Tucson, Arizona: University of Arizona, College of Optical Sciences (2005-06).